MODELING, OPTIMIZING, AND BUILDING OF A CONTINUOUS-FLOW XENON-129 POLARIZER WITH LUNG AND BROWN ADIPOSE TISSUE MAGNETIC RESONANCE IMAGING APPLICATIONS

Andrew Meeker McCallister

A dissertation submitted to the faculty at the University of North Carolina at Chapel Hill in partial fulfillment of the requirements for the degree of Doctor of Philosophy in the Department of Physics and Astronomy in the College of Arts and Sciences.

Chapel Hill
2019

Approved by:

Rosa Tamara Branca

Jack Ng

Alfred Kleinhammes

Tom Clegg

Hong Yuan

ABSTRACT

Andrew Meeker McCallister: Modeling, optimizing, and building of a continuous-flow xenon-129 polarizer with lung and brown adipose tissue magnetic resonance imaging applications
(Under the direction of Rosa T Branca)

Applications of hyperpolarized ^{129}Xe gas are quickly expanding from gas-phase lung ventilation imaging to dissolved-phase imaging in the lungs and in distal organs. The largest barrier to dissolved-phase imaging continues to be the low xenon polarization value that can be obtained with continuous-flow, spin exchange optical pumping (SEOP). While theoretically polarization values should approach 90%, in practice they have been around 30%. Research in our lab on the SEOP process occurring inside the optical pumping cell, using finite element analysis simulations, pointed out major shortcomings in the entire continuous flow SEOP setup. The goal of my work is to improve the SEOP setup. To this end, I have designed and constructed a new continuous flow ^{129}Xe polarizer that is expected to increase xenon residency time inside the optical pumping cell and reduce turbulence. At the same time, the new polarizer will make use of a new narrow laser that is specifically designed to optimize the optical pumping process.

One of the applications of gas-phase hyperpolarized ^{129}Xe gas is lung ventilation imaging. Fluorine-19 gas imaging has been proposed as an easier alternative to lung ventilation imaging with hyperpolarized gases. Here we compare the ability of ^{19}F to that of hyperpolarized ^{129}Xe gas MRI to detect ventilation defects in cystic fibrosis patients.

One of the applications of dissolved-phase hyperpolarized ^{129}Xe is the detection and thermometry of brown adipose tissue. Brown adipose tissue is a metabolically active fat tissue

whose malfunction has been recently associated with the development of obesity and diabetes. Fat fraction MR techniques have also been proposed as a high-resolution alternative method to detect and quantify brown adipose tissue. Here we analyze some of the shortcomings of these techniques, specifically the specificity of fat fraction to brown adipose tissue and the effect of microscopic magnetic susceptibility gradients on fat fraction quantification.

ACKNOWLEDGEMENTS

I am grateful for all those with whom I have had the pleasure of working with over the course of my time here. None of the human experiments could have been possible without the time, and expertise given by every fellow lab mate as well as the hard work of the study coordinators, and imaging technicians over at BRIC. The polarizer build would not have been possible without the previous research and modeling of my lab mates and the expertise and help of Wolfgang Wanger on the laser optics as well as the work done and practical advice given by Cliff Tysor in the physics and astronomy instrument shop.

To my fellow graduate students and friends, thank you for keeping me going and making what was a lot of hard work into an experience I will look back on fondly. To my family thank you for all of the support and love, everything I accomplish is ultimately a result of what you have given me. To my wife Steph, thank you for moving down to North Carolina for me and supporting me during this adventure that at times looked to have no end.

Thank you to each of the members of my Dissertation Committee for having taken time from their busy lives to provide feedback and guidance. I would like to especially thank Dr. Tamara Branca. As my advisor and mentor, you have shown me through your passion and expertise what it takes to be good researcher, and it goes without saying that none of this happens without your guidance.

TABLE OF CONTENTS

LIST OF FIGURES

LIST OF TABLES

LIST OF ABREVIATIONS AND SYMBOLS

BAT	Brown Adipose Tissue
BIC	Bayesian Information Criterion
BMI	Body Mass Index
CF	Cystic Fibrosis
CSE	Chemical Shift Encoded
CSI	Chemical Shift Imaging
CT	Computed Tomography
FDG	Fluorodeoxyglucose
F	Fluorine
FEV1	Forced Expiratory Volume
FF	Fat Fraction
FOV	Field of View
GRE	Gradient Recalled Echo
H	Hydrogen (Proton)
HP	Hyperpolarized
ID	Inner Diameter
IDEAL	Iterative Decomposition with Echo Asymmetry and Least squared estimation
LDX	Lipid Dissolved Xenon
MR	Magnetic Resonance
MRI	Magnetic Resonance Imaging
N_2	Nitrogen
NMR	Nuclear Magnetic Resonance

NST	Non-Shivering Thermogenesis
OD	Outer Diameter
PET	Positron Emission Tomography
PFA	Perfluoroalkoxy Alkane
PFP	Perfluoropropane
ppm	Parts per million
PTFE	Polytetrafluoroethylene (Teflon)
PRESS	Point Resolved Spectroscopy
R2*	Recoverable transverse relaxation rate
Rb	Rubidium
RBC	Red Blood Cell
RF	Radio Frequency
ROI	Region of Interest
SEOP	Spin Exchange Optical Pumping
SNR	Signal to Noise Ratio
STEAM	Stimulated Echo Acquisition Mode
SUV	Standard Uptake Value
T_1	Longitudinal relaxation time constant
T_2	Irrecoverable transverse relaxation time constant
T_2^*	Recoverable transverse relaxation time constant
TE	Echo Time
TMS	Tetramethylsilane
TR	Repetition Time

UHP	Ultra-High Purity
ULTEM	polyetherimide
UTE	Ultrashort Echo Time
VDP	Ventilation defect percentage
WAT	White Adipose Tissue
Xe	Xenon
ZTE	Zero Echo Time
δ	Water-fat frequency separation
1D	One Dimensional
2D	Two Dimensional
3D	Three Dimensional

CHAPTER 1: INTRODUCTION

Since its inception, magnetic resonance imaging (MRI) has become an indispensable, powerful, non-invasive, diagnostic and research tool. MR images are essentially tomographic maps of spin density, modulated by the magnetic properties of the detected spins, such as relaxation rates and chemical shifts, which directly reflect the specific chemical environment in which the spin resides. In MR, signal strength is directly proportional to the number of detected spins and to the their polarization. The latter, at thermal equilibrium, is determined by the Boltzmann distribution which, at room temperature and at magnetic field strengths of few Tesla, does not exceed few parts per million. Therefore conventional MRI typically relies on high concentrations of atoms for the detection of the nuclear spins of atoms. Such is the case for the ^{1}H atom which is present at high concentrations in biological tissues (~100M), while conventional MRI is not suitable for probing tissues/samples with low spin densities such as the lungs or gases.

Nuclear spin hyperpolarization enables one to overcome the sensitivity limit of MR and detect low-density spin systems such as gases. Since its first demonstration in 1994, nuclear spin hyperpolarization of noble gases such as Helium-3 (^{3}He) and Xenon-129 (^{129}Xe) has enabled the probing of lung ventilation function and structure in animal and human studies. While the initial work with hyperpolarized gas was done largely with ^{3}He, which has favorable magnetic properties such as a relatively high gyromagnetic ratio and high polarizability, increasing demand and reduced supply for ^{3}He have pushed researchers to look for alternative gases to polarize, such as ^{129}Xe. In the past 10 years, ^{129}Xe has become the gas of choice for MR research because of its

lower cost and the considerable improvement made in ^{129}Xe polarization efficiency. In addition to its lower cost, the relatively high solubility of xenon in biological tissues and its wide range of chemical shifts, have opened new avenues for MR research with hyperpolarized gases. Dissolved-phase xenon MRI has the potential to probe gas-exchange processes in the lungs, as well as the function and structure of distal tissues and organs such as the brain or brown adipose tissue. The translation of hyperpolarized gas MRI to the clinics, however, has been slow. The difficulties and intricacies associated with the hyperpolarization process, and the current inability of producing a large volume of highly polarized ^{129}Xe gas in a relatively short amount of time, have been the largest barrier to its widespread clinical adoption.

The technique most commonly used to produce clinically relevant amounts (~L) of noble gases is spin exchange optical pumping (SEOP). During SEOP, circularly polarized light is used to polarize the valence electron spins of an alkali metal. The electron spin polarization is then transferred to the nuclear spin polarization of the gas atom via atomic collisions. Continuous-flow SEOP is the set-up most commonly used to polarize large volumes of ^{129}Xe gas in a relatively short amount of time (~30 minutes).[1] However ^{129}Xe polarization values achievable by continuous-flow SEOP have been disappointing, averaging around 30%, far below the maximum theoretical polarization value of 90%, based on current modeling of the SEOP process. Clearly, current models of continuous-flow SEOP have either been ignoring some source of depolarization, or are too simplistic, lacking the complexity to model accurately what is happening inside of the optical cell. A lot of work has been done by our group to identify potential sources of polarization loss as well as more accurately model the optical pumping process.[2,3] This work has led to the redesign of our gas polarizer, described in Chapter 3, which we will expect to be capable of producing significantly larger batches of hyperpolarized ^{129}Xe gas with much higher polarization.

Because of the difficulties associated with gas hyperpolarization, which typically requires additional expertise, alternatives to hyperpolarized noble gases have recently been proposed for lung imaging. Fluorinated gases such as perfluoropropane (PFP) and sulfur hexafluoride are a viable thermally polarized alternative to hyperpolarized gases, thanks to some favorable MR properties of Fluorine-19 (^{19}F), such as a high gyromagnetic ratio (~3.4 times ^{129}Xe), higher natural abundance (100%), higher spin-density than ^{129}Xe, and more importantly, extremely short T_1 (1-20 ms, 2-3 orders of magnitude shorter than that of other nuclei), which allows for fast, repeated excitations of the spin system.[4] While preliminary images acquired in healthy subjects are promising, whether ^{19}F MRI can provide similar measures of structure and function in diseased lungs, because of the intrinsically lower resolution and lower sensitivity achievable with this technique and differences in gas delivery, is still an open question. To this end, in Chapter 4, I will report on the first comparison study between ^{129}Xe and ^{19}F MR lung imaging in patients with cystic fibrosis.

Thanks to its high solubility in tissues, once inhaled, xenon rapidly diffuses from the lung airspaces into tissue and to blood, which then carries the atoms to distant organs, where the atoms accumulate in a manner proportional to tissue perfusion and to the relative tissue/blood xenon solubility. Several medical imaging techniques have been using xenon to quantify perfusion in the brain, heart and kidney, or to detect liver fat content. These techniques typically use radioactive ^{133}Xe for SPECT imaging or stable xenon with computed tomography, CT. Hyperpolarized xenon MRI could potentially provide a radiation-free alternative to these techniques. In addition to providing perfusion information, xenon MRI could provide additional information, such as the chemical composition of the tissue into which xenon diffuses. This is possible thanks to the wide range of chemical shifts that ^{129}Xe exhibits in biological tissues. Our group has leveraged this

property of hyperpolarized xenon MRI to image metabolically active fat tissues, like brown adipose tissue. Brown adipose tissue (BAT) is a fatty tissue that specializes in cold-induced thermogenesis. Having been shown to regulate energy expenditure and body weight, as well as blood glucose levels in rodents,[5,6] this tissue has been the subject of intense research and a target for anti-diabetes and anti-obesity therapies.[7,8] However at the moment, the greatest impediment to BAT research in humans, is the lack of a non-invasive, reliable imaging technique that can differentiate this tissue from other tissues.[9] The most commonly used imaging technique to detect BAT in humans is positron emission tomography (PET) with ^{18}F-fluorodeoxyglucose (FDG). FDG-PET uses a radioactive glucose analogue to map tissues that are glucose avid, like cancerous tissues or BAT.[10] Glucose, however, is not the primary substrate of BAT thermogenesis and therefore not an ideal biomarker for thermogenesis. In addition, FDG-PET cannot be used for longitudinal studies in humans due to concerns over radiation exposure on healthy research subjects.[11] Our group has shown that MRI with hyperpolarized xenon gas can provide a radiation-free alternative to FDG-PET for the detection of BAT and its activity, which is detected via lipid-dissolved xenon (LDX) MR thermometry, a technique also developed in our laboratory.[12] Other higher resolution MRI techniques have also been proposed as radiation-free alternatives to FDG-PET and could offer complementary structural information. Specifically, most of the MR research in BAT has focused on fat-water MR separation techniques, with which people try differentiate the more hydrated brown fat from the less hydrated white fat tissue.[13–17] While studies have shown that this may be a useful technique in rodents and infants, whether or not this is a valid method to differentiate these two tissues in adult humans is up for debate.[13,18] Several studies have been done comparing the mean MR derived fat fraction of the entire supraclavicular depot, where most of the BAT is located in adult humans, with glucose maps obtained with FDG-PET/CT[14,15,19]. However,

as the two maps were acquired using different scanners during separate imaging sessions, a direct comparison between the two could not be made.[20] With the aid of one of the first hybrid MRI/PET scanners available at our institution, we have performed the first direct comparison of FDG-PET and MR fat fraction techniques in cold-challenged adults for brown adipose tissue detection.[21] As will be discussed in Chapter 5, the overall results showed that glucose uptake, as measured by FDG-PET, does not necessarily occur in regions of low fat fraction (as measured by MRI), such that fat fraction based MR techniques cannot differentiate metabolically active tissues like BAT from other fat tissues. A fat fraction threshold could not be used to differentiate glucose-avid tissues from other tissues, at least within the supraclavicular fat depot. We did however detect small decreases in fat fraction over time in the glucose-avid fat regions in few subjects during stimulation of BAT activity. These decreases are consistent with the notion that during BAT thermogenesis, this tissue converts intracellular fat into heat.[22]

We have also investigated the robustness of modern fat fraction MR techniques. Modern fat fraction techniques generally work by measuring the signal from a mix of fat and water spins at multiple time points. The signal is then fit to a signal model, which depends on the number of detectable fat-spins, water-spins, their relaxation time, and the relative frequency of these spins. While developing a new MR thermometry method based on hyperpolarized xenon, and comparing this method with more traditional water-fat MR thermometry methods,[12,23] we came across the issue that water and fat spins do not mix at the microscopic level, but sit in compartments that have very different magnetic properties. Specifically, the difference in magnetic susceptibility between water and fat compartments imparts an additional frequency shift that differs for fat and water spins. How much the applied shift differs between spin species, depends on the spatial distribution of the two spin species and their orientation with respect to the static external magnetic field. This

effect is often not accounted for in current fat fraction signal models.[24–26] As will be discussed in Chapter 6, we have performed simulations and phantom studies to quantify this effect and determine its effect on the accuracy of fat fraction quantification techniques in the context of BAT detection.

CHAPTER 2: RELEVANT BACKGROUND

Section 2.1: Polarization

Section 2.1.1: Defining Polarization

All elementary particles possess an intrinsic angular momentum called spin. Protons and neutrons have intrinsic angular momentum of ½ ħ and, as a result, every element in the periodic table has at least one isotope with a non-zero nuclear spin. Nuclear spins give rise to a magnetic moment $\vec{\mu}$ given by 2.1 where γ is the gyromagnetic ratio and $\vec{S}$ is the spin angular momentum.

$$\vec{\mu} = \gamma * \vec{S} \text{ (2.1).}$$

When an atom with a non-zero nuclear spin is placed in a magnetic field *B,* the interaction energy between the spin magnetic moment and the external magnetic field can be described by the Hamiltonian:

$$H = \vec{\mu} \cdot \vec{B} = \gamma * \vec{B} \cdot \vec{S} \text{ (2.2).}$$

For atoms with nuclear spin $\frac{1}{2}$ ħ, if the magnetic field $\vec{B}$ is oriented along the z-direction, the interaction energy between the nuclear spin magnetic moment and the external magnetic field becomes $H = -\gamma B_o S_z$ where $S_z = \pm\frac{\hbar}{2}$ and the allowed energy levels become:

$$E = \pm\frac{\hbar}{2}\gamma\, B_o = \pm\frac{\hbar}{2}\omega_o \text{ (2.3),}$$

where $\omega_o = \gamma B_o$ is the Larmor frequency.

For a sample of atoms with nuclear spin ½ ħ, these two energy levels will be populated according to the Boltzmann distribution

$$\frac{N_+}{N_-} = e^{-\Delta E \mathrm{kT}} \text{ (2.4).}$$

In nuclear magnetic resonance, one detects not a single spin but an ensemble of nuclear spins. An ensemble of nuclear spins placed in a magnetic field typically produces a detectable magnetization M_o, defined as

$$M_o = \frac{\hbar}{2} \gamma N_s P \text{ (2.5),}$$

where N_s represents the total number of nuclear spins in the sample, and P represents the nuclear spin polarization, i.e. the difference in population between the two energy levels, defined as

$$P = \frac{N_+ - N_-}{N_+ + N_-} \text{ (2.6).}$$

In the high temperature approximation, $\Delta E / kT << 1$, P can be approximated as:

$$P = \frac{\gamma \hbar B_o}{2kT} \text{ (2.7).}$$

This quantity, which represents the excess of spins in the lower energy state, is on the order of 10^{-6} at room temperature in a 3T magnetic field, thus limiting the sensitivity of most NMR experiments to samples that contain a large number of nuclear spins.

Hyperpolarization techniques allow us to increase P, thus enhance the NMR sensitivity by several orders of magnitude. Via hyperpolarization the spin system is pushed into a non-

equilibrium state, where most of the spins "sit" in one of the two energy levels. This non-equilibrium state produces a much stronger MR signal that will return to its much smaller thermal equilibrium value with a time constant T_1, called the longitudinal relaxation time.

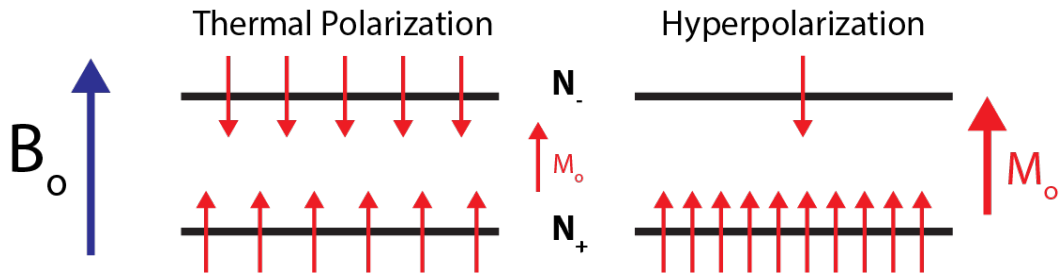

Figure 2.1 Under thermal equilibrium (a.) the two energy levels are almost equally populated, with a very small excess of spins in the lower energy state. With hyperpolarization, the spin system is forced into a non-equilibrium state where most of the spins occupy one of the two energy levels. N_+ and N_- denote the population of the two spin states.

Section 2.1.2: Spin Exchange Optical Pumping

While many hyperpolarization techniques exist, for gases the most commonly used hyperpolarization technique is spin exchange optical pumping (SEOP), a two-step process which can increase nuclear spin polarization of noble gases such as ^{3}He and ^{129}Xe by several orders of magnitude. During SEOP, the outer electron of an alkali-metal (usually, Rb, Cs, or K) is first polarized using circularly polarized laser light. In our polarizer we typically use Rb, and the laser light is tuned to the D1 spectral transition (795nm) of Rb. The rubidium electron polarization is then transferred to the xenon nuclear spin during spin-exchange collisions via Fermi contact interactions.

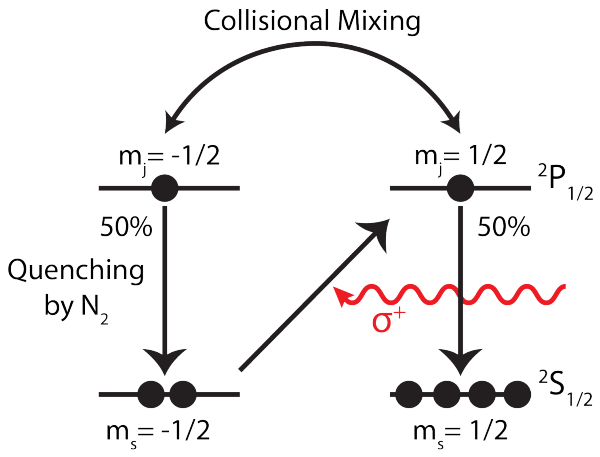

Figure 2.2 Illustrated optical pumping process for Rb.

A pictorial representation of the Rb electron pumping process is shown in Figure 2.2. When rubidium is placed in a magnetic field, the Zeeman sublevels split ($m_s = \pm ½$). This splitting is 466 kHz/G and varies linearly with the strength of the magnetic field at low fields. At thermal equilibrium, the population difference between these two sublevels is very small. However, circularly polarized light, resonant with the Rb D_1 line at 795nm, selectively excites the $^2S_{1/2}$ m=-½ to $^2P_{1/2}$ m=½ transition. Collisions with other atoms rapidly equalize the populations of the excited state sublevels, from which the electrons rapidly decay back to their ground states emitting unpolarized radiation at the D_1 frequency. In order to prevent depolarization of Rb atoms by the emitted unpolarized radiation, nitrogen is commonly introduced in the gas mixture as buffer gas. With the addition of nitrogen, excited Rb electrons decay back to the ground state by transferring their energy to the vibrational and rotational modes of the nitrogen molecules. Continuous selective depletion of the $^2S_{1/2}$ m=-½ state eventually depopulates this state, thus creating a population difference between the $^2S_{1/2}$ m=-½ state and the $^2S_{1/2}$ m=½ state.

The local steady state Rb polarization, P_{Rb}, can be described in terms of the mean optical

pumping rate per unpolarized alkali-metal atom $\gamma_{opt}(r)$, and the electron spin destruction rate, Γ_{SD}.

$$P_{Rb} = \frac{\gamma_{opt}(r)}{\gamma_{opt}(r)+\Gamma_{SD}} \text{ (2.8).}$$

The local mean optical pumping rate, $\gamma_{opt}(r)$ can be described as

$$\gamma_{opt}(r) = \int_0^\infty \Phi(r,\upsilon)\sigma_{op}(\upsilon-\upsilon_o)d\upsilon \text{ (2.9),}$$

where $\Phi(r,\upsilon)$ is the local laser intensity per unit frequency and $\sigma_{op}(\upsilon-\upsilon_o)$ is the light absorption cross section. The electron spin destruction rate is dominated by collisions of rubidium with other gas particles as opposed to wall collisions. This rate can be empirically measured but is highly dependent on experimental conditions.

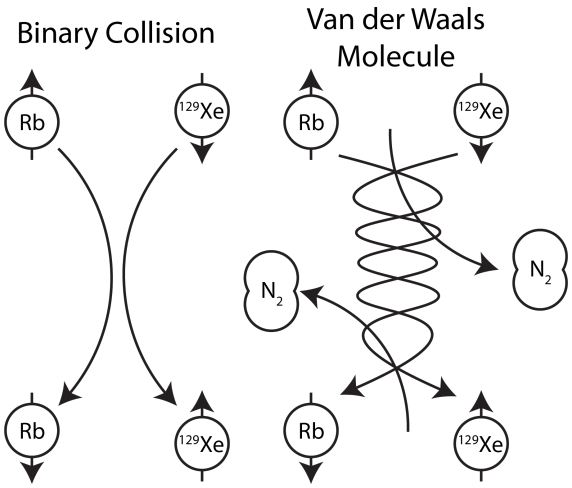

Figure 2.3 Spin transfer between the rubidium electrons and the xenon nucleus through binary collisions and through the formation of Van der Waals molecules.

Once the rubidium spins are polarized, the electron spin polarization is transferred to the nuclear spin of xenon through the Fermi contact interaction, during either binary collisions or during the formation of short-lived Van der Waals molecules. The overall spin exchange rate γ_{SE},

which depends on the temperature and concentration of the gases present in the gas mixture, determines, along with the average rubidium polarization, $\langle P_{Rb} \rangle$, and the spin destruction rate of xenon gas, Γ, the xenon polarization:

$$P_{Xe}(t) = \langle P_{Rb} \rangle \frac{\gamma_{SE}}{\gamma_{SE}+\Gamma}(1 - e^{-(\gamma_{SE}+\Gamma)t}) \quad (2.10).$$

The xenon spin destruction rate Γ is the result of the interaction of xenon atoms with other gas molecules, Γ_D, the interaction with paramagnetic impurities present on the optical cell walls, Γ_{wall}, and the spin relaxation caused by the possible diffusion of the atom in a magnetic field gradient, $\Gamma_{\Delta B}$.

$$\Gamma = \Gamma_D + \Gamma_{wall} + \Gamma_{\Delta B} \quad (2.11).$$

Section 2.2: Continuous-Flow Xenon Gas Polarizer

Two main setups are used to polarize ^{129}Xe gas via SEOP: stopped-flow and continuous-flow.[27–32] While it has recently been shown that stopped-flow SEOP can produce near unity xenon polarizations, continuous-flow SEOP is the most widely used setup for clinical applications as it enables the production of large volumes of gas in a relatively short time.[1]

Section 2.2.1: Polarizer Set-Up

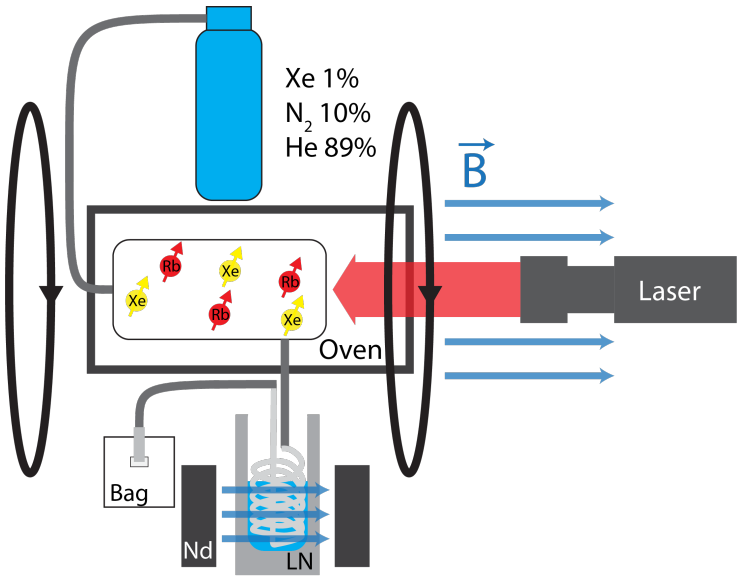

Figure 2.4 Simplified schematic of a continuous-flow polarizer. An optical cell containing Rb is heated in an oven in the presence of a weak magnetic field (~2mT). Circularly polarized laser light is shone on the optical cell, to polarize Rb electrons. A gas mixture containing Xe, N_2, and He, flows in and out of the optical cell, where spin-exchange occurs. After flowing out of the cell, the polarized Xe gas is extracted from the gas mixture and accumulated in the solid state by a liquid nitrogen trap, located in a relatively strong magnetic field (~200 mT). When enough gas is accumulated, replacement of liquid nitrogen with warm water is used to sublimate the solid xenon quickly, which is then transferred into a Tedlar bag (Jensen Inert Products) for delivery.

Figure 2.4 shows a simplified schematic of a continuous-flow polarizer. A lean mixture of 1% Xe, 10% N_2 and 89% ^{4}He is used to reduce the Rb-^{129}Xe spin destruction rate as this is the dominant relaxation process at high pressures.[8] The gas mixture flows into a glass-walled optical pumping cell that contains rubidium inside of a heated oven. Electromagnetic coils provide a magnetic field for the optical pumping to take place. As the gas flows through the cell, ^{129}Xe undergoes spin exchange with Rb for a duration t_{res}, i.e. the time the gas spends in the optical cell. The final polarization of ^{129}Xe gas strongly depends on the residency time and on the spin-up rate from Eqn. 2.10,

$$P_{Xe}(t_{res}) = \langle P_{Rb} \rangle \frac{\gamma_{SE}}{\gamma_{SE}+\Gamma}(1 - e^{-(\gamma_{SE}+\Gamma)t_{res}}) \text{ (2.12).}$$

At the low ^{129}Xe partial pressures used to polarize ^{129}Xe for biological imaging applications, Xenon must be removed from the buffer gases. As xenon freezes at 161 K, xenon is generally separated from the buffer gases and accumulated as frozen xenon using a liquid nitrogen trap. Assuming relaxation of the gas after exiting the optical cell is negligible, the final polarization of xenon will depend on the polarization of the gas leaving the cell, as well as on the accumulation time, t_a, i.e. the time the gas spends in the solid state, and on the relaxation time of solid state xenon T_1.[33]

$$P_{Xe}(t_a) = P_{Xe}(t_{res})\frac{T_1}{t_a}(1 - e^{-t_a/T_1}) \text{ (2.13).}$$

At strong magnetic fields and low temperatures (20-120K), relaxation of frozen xenon is dominated by the phonon-induced spin-rotation interactions between the nuclear spin of the ^{129}Xe atoms and the angular momentum of the ^{129}Xe atom itself or of a nearest-neighbor atom.[34] At a magnetic field strength above 1000G, this interaction and the resulting T_1, which is on the order of 5000s, is relatively field independent. Because of this, strong permanent magnet arrays are typically used to create large magnetic fields where xenon is accumulated and stored in the solid state. At higher temperatures, particularly those approaching the xenon melting point, 161 K, relaxation rates increase dramatically because of dipole-dipole interactions between ^{129}Xe and ^{131}Xe atoms, modulated by vacancy diffusion in the solid.[35]

Relaxation of xenon transiting from the optical cell to the cold finger may be significant. The presence of magnetic field inhomogeneities along the gas flow path can cause additional relaxation of hyperpolarized gases. This has been thoroughly studied and is a collision mitigated process well

described by the following relation:[36,37]

$$\frac{1}{T_1} = \frac{|\Delta B_T|^2}{B_0^2} \frac{D}{(1+\Omega_0^2 \tau_c^2)}) \quad (2.14),$$

where T_1 is the time constant of the longitudinal relaxation, D represents the diffusion coefficient of the gas, B_0 is the magnitude of the mean magnetic field, and ΔB_T is the transverse component of the spatial magnetic field gradient. The extra factor, $(1 + \Omega_0^2 \tau_c^2)$ accounts for rotation of spins between kinetic collisions, where Ω_0 is the Larmor frequency and τ_c is the diffusion correlation time, i.e. the time between collisions. Burant *et al.* 2016 showed, using Monte Carlo simulations of diffusing spins, that regions in which the magnetic field rapidly changes direction and areas of near zero field are the cause of significant depolarization in continuous flow set-ups, along with collisions of the gas with the walls of the container/pipes in which the gas flows.[3]

Section 2.3: Principles of MRI

Section 2.3.1: Bloch Equations and Spin Relaxation

Once an ensemble of spin is polarized, whether through hyperpolarization or thermal means, then the net magnetization, given by the sum of the single magnetic moments, can be measured globally (spectroscopy), or locally (imaging). In order to detect the net magnetization, $\vec{M}$, the magnetization needs to be decoupled from the main magnetic field. Thus the magnetization is typically rotated into a plane orthogonal to the direction of the main magnetic field $\overrightarrow{B_o}$ through the application of a second magnetic field, $\overrightarrow{B_1}$, orthogonal to $\overrightarrow{B_o}$. During the application of the rotating field $\overrightarrow{B_1}$, the evolution of the magnetization vector can be described by the Bloch equation:

$$\frac{d\vec{M}}{dt} = \gamma \vec{M} \times \vec{B}_{eff}, \text{ where } \vec{B}_{eff} = \overrightarrow{B_o} + \overrightarrow{B_1} \quad (2.15).$$

If the B_1frequency coincides with the Larmor frequency, the magnetization will be rotated away from the $\hat{z}$ direction by an angle that can be easily determined by:

$$\alpha = \gamma \int_0^{\tau} B_1(t)dt \text{ (2.16)},$$

where B_1 is the amplitude of the applied magnetic field and τ is its duration.

Following the excitation, the longitudinal and transverse component of the magnetization start to relax via two mechanisms: spin-lattice relaxation (T_1), and spin-spin relaxation (T_2), respectively. Spin-lattice relaxation describes the return to thermal equilibrium of the perturbed spin system, or magnetization vector. Spin-spin relaxation, or transverse relaxation, describes the loss of phase coherence within the spin system. Specifically, as each spin in the spin ensemble experiences slightly different temporal and spatial variations in the local magnetic field, they start to acquire slightly different phase-shifts that reduce the magnitude of the transverse magnetization vector. In presence of macroscopic field inhomogeneities across the sample, phase coherence is lost more rapidly, and the decay of the transverse magnetization is characterized by a shorter time-constant, $T_2^*<T_2$. Spin dephasing from macroscopic field inhomogeneities can be recovered, at least in part, by spin-echo experiments where spins are flipped and allowed to precess in the opposite direction for the same period of time, accumulating an equivalent but opposite phase. This is not true of the dephasing caused by temporal and spatial inhomogeneities present at the –nano and –micro scales that, due to spin diffusion, cannot be "rewound".

To account for these relaxation mechanisms, the Bloch equation is modified as 2.17,

$$\frac{d\vec{M}}{dt} = \gamma\vec{M} \times \vec{B}_{eff} - \frac{\vec{M}_x\hat{x}+\vec{M}_y\hat{y}}{T_2} - \frac{(\vec{M}_z-M_o)\hat{z}}{T_1} \text{ (2.17)}.$$

If we apply an RF-pulse such that $\alpha = \frac{\pi}{2}$, ideally all of the original longitudinal magnetization M_o will be tipped into the transverse plane where $M_z(0) = 0$ and $M_{xy}(0) = M_o$. If we stop the B_1 field and move into a reference frame rotating at ω_o about the B_o field, then the magnetization can be described simply:

$$\frac{dM_{xy}}{dt} = -\frac{M_{xy}}{T_2} \text{ (2.18)},$$

$$\frac{dM_z}{dt} = -\frac{M_o - M_z}{T_1} \text{(2.19)},$$

with the solutions:

$$M_{xy} = M_o e^{-\frac{1}{T_2}} \text{ (2.20)},$$

$$M_z = M_o(1 - e^{-\frac{1}{T_1}}) \text{ (2.21)}.$$

The detected signal M_{xy} will then be proportional to the equilibrium magnetization M_o, and will decay in time with a time constant T_2.

Section 2.3.2: Chemical Shifts

The Larmor frequency ω_o is directly proportional to the magnetic field felt by nucleus. This field is in general different than the external magnetic field B_o, because of the magnetic shielding produced by the electron cloud surrounding the nucleus. In general, the electron cloud shields the nucleus from the external magnetic field by producing an opposite field $B_o\sigma$. As a result, the local field felt by the nucleus can be described as 2.22.

$$B = B_o(1 - \sigma) \text{ (2.22)}.$$

The amount of shielding, and thus the resonance frequency of a specific nucleus ω, directly depends on the field B experienced by nucleus, and is a reflection of the electronic cloud and the chemical environment of the atom in which the nucleus resides:

$$\omega = \gamma B_o(1 - \sigma) \text{ (2.23).}$$

As this frequency is field dependent, one often likes to refer to a field-independent quantity, the chemical shift δ, defined as the field-normalized difference between the resonance frequency of the atom ω and the resonance frequency of a reference atom, ω_R:

$$\delta = \frac{\omega - \omega_R}{\omega_R} \times 10^6 \approx (\sigma_R - \sigma) \times 10^6 \text{ (2.24).}$$

For ^{1}H, the reference resonance frequency is the frequency of tetramethylsilane (TMS), assumed to be at 0 ppm. At room temperature, water is less shielded than TMS, with a chemical shift of 4.8 ppm. Lipid protons are typically more shielded than water protons, with a chemical shift ranging from 0.9 ppm to 5.31 ppm for the different chemical groups, as shown in the table below.

Chemical Group	Chemical Shift
	ppm
$-CH_3$	0.90
$-(CH_2)_n-$	1.30
$-CH_2-CH_2-COO$	1.59
$-CH_2-CH = CH-CH_2-$	2.03
$-CH_2-COO$	2.25
$=CH-CH_2-CH =$	2.77
$-CH = CH-$	5.31

Table 2.1 The different chemical groups of fats and their associated chemical shifts.

If an ensemble of chemically inequivalent spins is excited, the resulting signal will be a combination of the signals of the different chemical groups with their different frequencies. A Fourier transform of the time-dependent signal leads to the direct detection of the nuclear spin frequency distribution of the spin ensemble, with the area under each frequency line proportional to spin number density of the different chemical species. For a sample containing water and fat spins, the 3.5 ppm difference in chemical shift between the water and the fat peak (in this case the methylene peak $(CH_2)_n$, which is the most abundant species in fat molecules), is a significant 420 Hz at 3T and can easily be resolved (Figure 2.5).

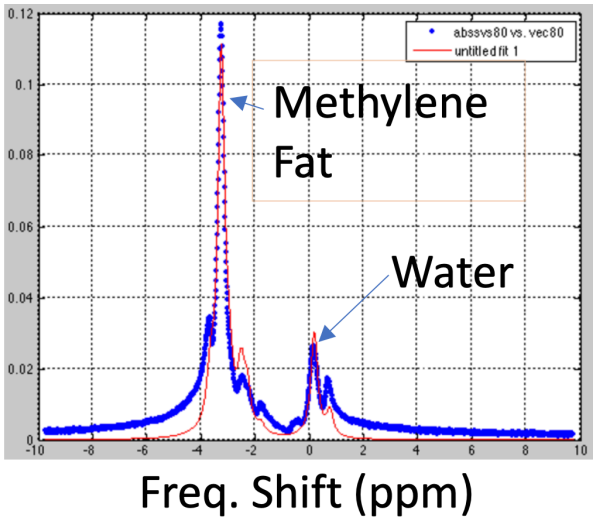

Figure 2.5 Frequency spectrum of an 80%-fat 20%-water phantom on a Siemens Biograph operating at a magnetic field strength of 3T, showing different resonance frequencies corresponding to different fat chemical groups and to water (centered at 0 ppm).

In general the chemical shift of a given nucleus depends not only on the chemical make-up of the molecule in which the spin resides, but also on the chemical environment in which the molecule is placed. The nature of surrounding molecules, pH, and temperature can all have large effects on the resulting chemical shift and, in general, the larger the electron cloud of the nucleus, the higher the sensitivity to its chemical environment. For example, whereas the nuclear spin of ^1H atoms has

a chemical shift range of just 10ppm, ^{129}Xe atoms have a nuclear spin with a chemical shift range of more than 300ppm.

Section 2.3.3: Magnetic Resonance Imaging

In magnetic resonance, in order to produce images the magnetization needs to be spatially encoded. Spatial encoding of the magnetization is accomplished via the application of spatially varying magnetic fields, or magnetic field gradients, typically denoted by G_x, G_y, G_z. Spatially varying magnetic fields produce spatially varying spin precession frequencies, enabling encoding of spatial information into frequency information. For example, a linear magnetic field gradient applied along the z-direction, as in figure 2.6, will produce a signal whose spectrum corresponds to the projection of the spin ensemble along the direction of the applied field gradient.

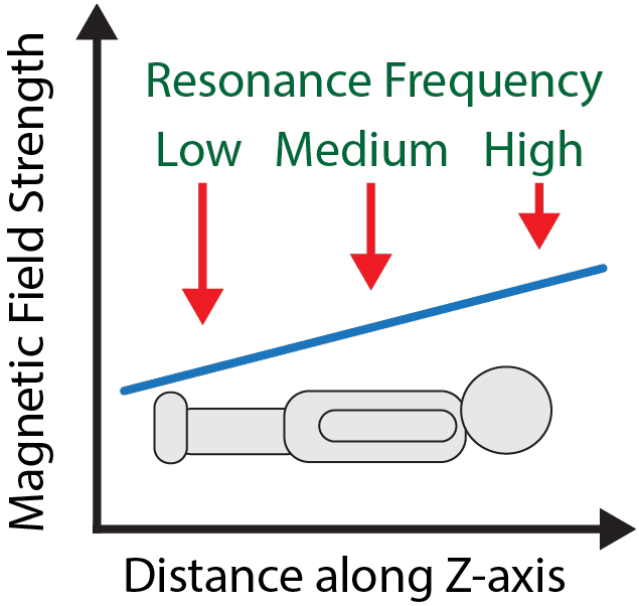

Figure 2.6 Illustration of the z-gradient field, with magnetic field strength varying linearly with position along the z-axis.

To spatially encode the spins in 2 or 3 dimensions, a two or three-dimensional k-space technique is commonly employed. A two-dimensional k-space technique often includes the

application of a gradient in conjunction with the application on an excitation pulse B_1. The gradient will produce a spatially varying frequency along its direction, and a resonance condition only for those spins whose resonance frequency is within the bandwidth of the B_1 field. By changing the center frequency of the B_1 field and its bandwidth, one can excite and detect the signal only from specific "slices".

To spatially encode the spins in the other two dimensions, magnetic field gradients are typically applied during the acquisition of the MR signal. These gradients impart to the spatially varying signal s(x,y) a phase evolution that depends on the strength of the applied gradients and on their position in the x-y plane. The time evolution of the MR signal during the application of these gradients is then given by:

$$S(t) = e^{i\omega_0 t} \iint^{FOV} s(x,y) e^{i\gamma G_x x t_x} e^{i\gamma G_y y t_y} dxdy \quad (2.25).$$

By renaming $k_x = G_x t_x$ and $k_y = G_y t_y$ we obtain the expression of the signal in k-space.[38]

$$S(k_x, k_y) = e^{i\omega_0 t} \iint^{FOV} s(x,y) e^{ik_x x} e^{ik_y y} dxdy \quad (2.26).$$

It is clear that an inverse Fourier transformation of the acquired signal $S(k_x, k_y)$will enable the reconstruction of the spatial signal distribution $s(x,y)$. The resolution of the resultant image depends on the magnitude of k_x , k_y , thus on the magnitude of the applied field gradient. This means that, unlike for other tomographic imaging techniques, the resolution of MRI is not diffraction limited. In principle the resolution could be as high as one would wish. In practice, however, resolution is ultimately limited by the available signal strength (higher resolution leads to smaller MR voxels, thus lower signals), and by diffusion of the observed atoms/molecules, which can "smear out" the frequency encoding imparted to the spins by the magnetic field

gradients.

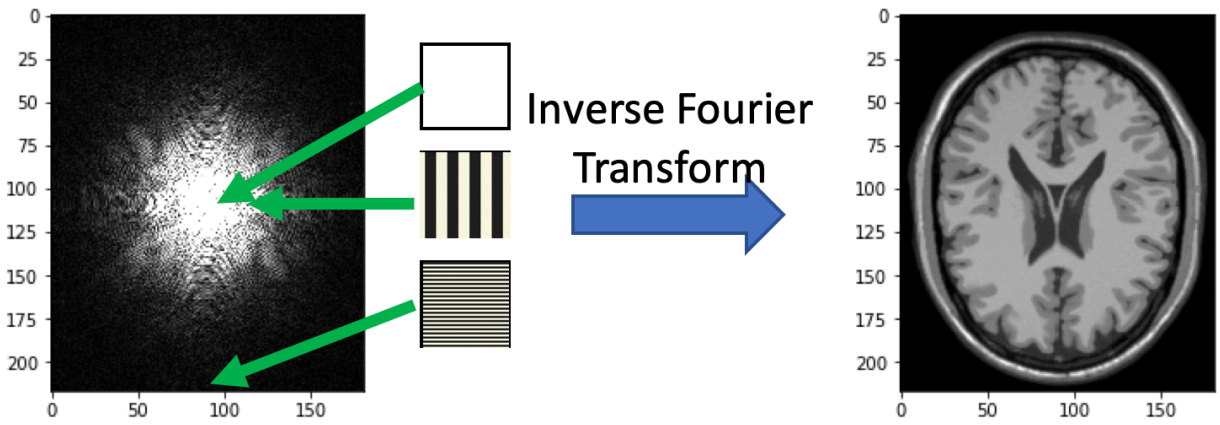

Figure 2.7 Illustration of k-space and its relation to "image-space". Points with high k values are those that contain high spatial frequency information, and therefore their acquisition leads to the acquisition of high resolution images. The MR signal is acquired in k-space. A FT then leads to image formation.

In a typical 2D imaging experiment a N_yxN_x matrix of the k-space is acquired using a gradient echo sequence (GRE), shown in Figure 2.8. In this sequence, a radiofrequency pulse is turned on in conjunction with a magnetic field gradient to selectively excite only those spins from a specific "slice" in the sample. A phase gradient and a "pre-read" gradient is then turned on to impart to the spins a position-dependent phase shift. In k-space, this is equivalent to a positive shift along k_y during the application of the phase-gradient (green arrow) and a negative shift in k_x (orange arrow), during the application of the pre-read gradient. During the acquisition phase, only the read gradient is turned on, enabling the acquisition of one line of k space along the k_x direction at a time. The process is repeated Ny times, each with a different value of the phase-encoding gradient. This methodology, called spin–warp, has been the most commonly used method in magnetic resonance to encode the MR signal spatially. A variable time delay between the excitation pulse and the acquisition of the center of k-space (echo time, or TE) can impart a different contrast to the image.

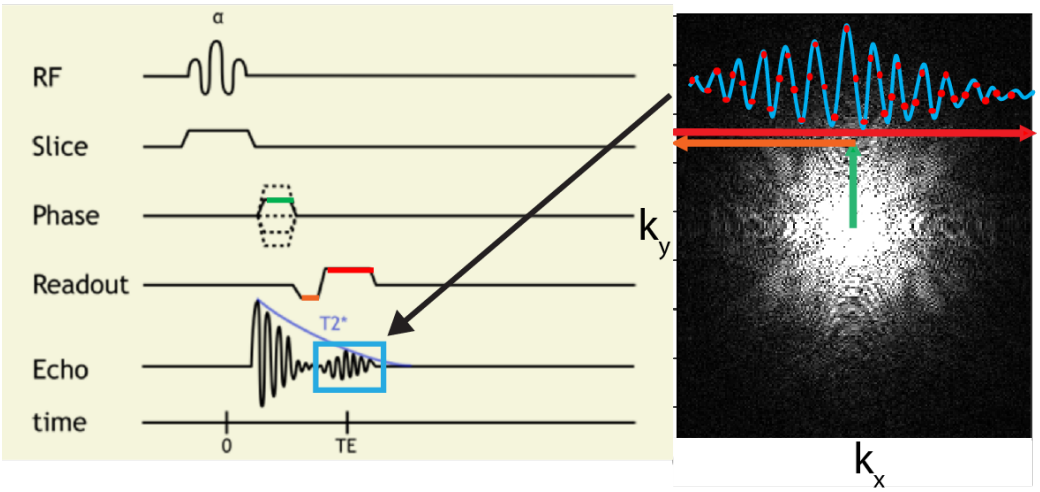

Figure 2.8 A pictorial explanation of a gradient echo sequence. The phase gradient (green) is shown to move the signal through k-space in the k_y direction (phase gradient assumed along the y-direction). The readout gradient is first applied (orange) to move the signal through k-space in the $-k_x$ direction and then applied (red) to sweep across k-space in the $+k_x$. During this sweep the signal is sampled N-times (red dots) with the signal being acquired at a controllable echo time (TE). This process is repeated N-times with N different phase-gradient strengths for an N by N matrix acquisition.

Section 2.4: PET Imaging

Positron Emission Tomography (PET) measures the two 511 keV photons that are produced from a positron-electron annihilation after positron emission (β^+) from a radionuclide tagged tracer molecule shown in Figure 2.9.

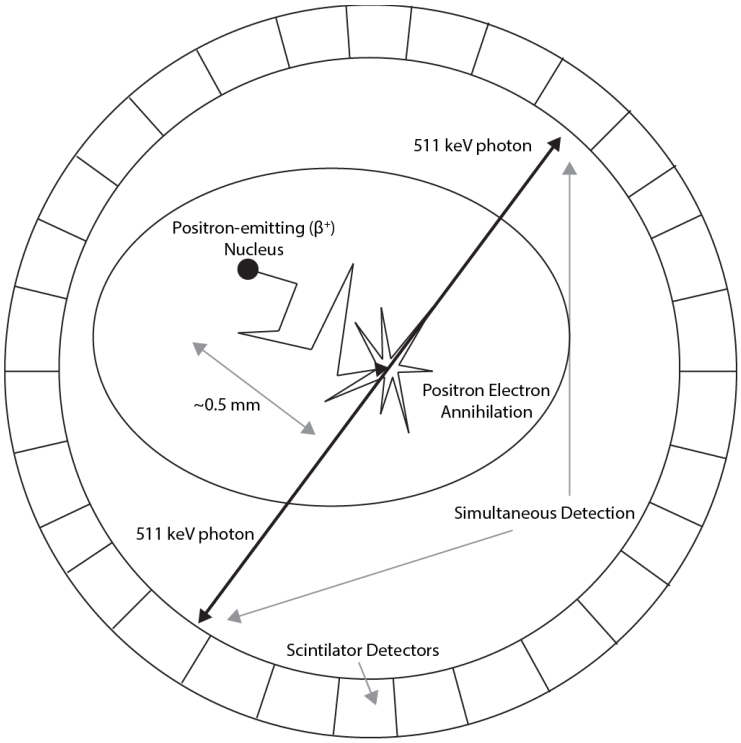

Figure 2.9 Pictorial representation of the general principles of PET detection: radioactive decay of a radio nuclide, positron (β^+) emission, positron-electron annihilation producing two 511 keV annihilation photons that simultaneously strike scintillator detectors located at two opposite sides. (Not to scale)

If detectors register a simultaneous event ($\Delta t < 10$ ns), a line of response is recorded along which the annihilation has occurred. From these lines of response, the image is reconstructed using a back projection reconstruction. In measuring lines of response, the PET detectors are essentially measuring projections of the object, $f(x, y)$, at multiple angles, $p(r, \theta)$. These projections can be smeared back over the object across all angles to reconstruct an image, where in practice the integrals are discrete sums.

$$f_{bp}(x, y) = \int p(r, \theta)\, d\theta = \int p(x\, cos\theta + y\, sin\theta, \theta)\, d\theta \quad (2.31).$$

However, this reconstructed image is blurry; to understand why we must look at the central slice theorem. The central slice theorem states that the 1D Fourier transform of a projection at an angle is equivalent to the slice at the same angle of the 2D Fourier transform.

$$\mathcal{F}_1\{p(r,\theta=\theta')\} = \mathcal{F}_2\{f(x,y)\}|_{\theta=\theta'} \text{ (2.32).}$$

This implies that summing over the projections at angles, θ, is equivalent to sampling the 2D k-space radially, $F(\omega,\theta)$. This oversamples the low-frequencies of the images by a factor of ω. To account for this oversampling, filtered-back projection is the most commonly applied reconstruction technique. In filtered-back projection, the projections are first Fourier transformed, a filter of $|\omega|$ is then applied to account for oversampling, and the projections are inverse Fourier transformed and then finally back projected to create the image.

$$f_{fbp}(x,y) = \int q(r,\theta)\, d\theta \quad \text{where} \quad q(r,\theta) = \mathcal{F}_1^{-1}\{|\omega|\mathcal{F}_1\{p(r,\theta=\theta')\}\} \text{ (2.33).}$$

PET images are subject to a number of artifacts affecting these images, the largest being the attenuation of the radiation by the object itself. The more tissue that the photons have to travel through, the larger the probability that they are scattered and don't reach the detector to form a "line of response." Therefore, the higher the amount of tissue passed through, the lower the observed activity level. To correct for this, an MRI or CT image is typically collect along-side the PET image, from which an attenuation map is computed and used to derive the attenuation-corrected PET image.

One common PET tracer used to look for metabolic activity is Fluorodeoxyglucose (^{18}FDG), a glucose analogue where the radionuclide ^{18}F is substituted for the normal hydroxyl group as shown in Figure 2.11.

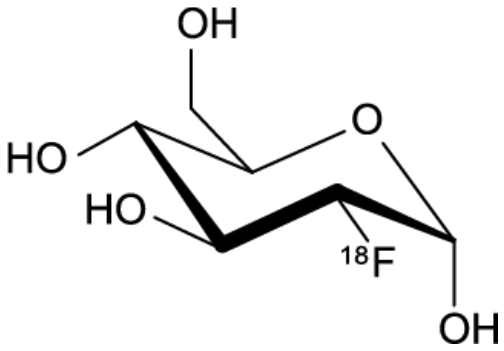

Figure 2.10 Structure of ^{18}FDG, a glucose molecule where the normal 2-hydroxyl group (-OH) is substituted for the radionuclide ^{18}F.

The ^{18}F radionucleide has a relatively short half-life of 110 minutes. In the body, FDG acts as a glucose analogue, being taken up into glucose avid tissues via glucose transporters and undergoing phosphorylation by hexokinase. Once phosphorylated, FDG cannot be transported quickly out of the cell or metabolized further, so it is trapped in the cell to be imaged. There are several methods for measuring the rate and total amount of FDG accumulation. All PET scanners measure the radioactivity concentration, which is directly related to the FDG concentration. What that concentration means *in vivo,* however, is dependent on the amount injected, the decay time, and the weight of the subject. For example, in larger subjects FDG is diluted. Therefore, images are typically rescaled to give a standardized uptake value (SUV) of the tracer, normalizing by the subject's body weight and injected dose to allow for comparison between different studies:

$$SUV = \frac{r}{(\frac{a'}{w})} \quad (2.34),$$

where r is the decay-corrected radioactivity concentration directly measured, a' is the amount injected and w is the weight of the subject.[39]

CHAPTER 3: MODELING AND BUILDING A CONTINUOUS-FLOW ^{129}XE POLARIZER

Section 3.1: Motivation

Hyperpolarized ^{129}Xe gas has been used for many different applications in magnetic resonance. Our group has used HP ^{129}Xe to detect and image brown adipose tissue, for temperature mapping in fatty tissues, and for imaging lung ventilation in patients with CF. For dissolved-phase imaging applications, such as the detection of brown fat or temperature mapping, the largest barrier continues to be the low xenon polarization obtainable with current continuous-flow spin exchange optical pumping setups. Current models of continuous flow SEOP considerably overestimate the final xenon polarization able to be achieved experimentally. Where theoretically polarization values should approach 90%, in practice they hover around 30%, with the exception of few cases.[2,33] This implies that current models are ignoring some important sources of depolarization and/or lack the complexity to accurately model what is happening inside of the optical cell. A lot of work has been done by our group to identify potential sources of gas depolarization on current ^{129}Xe polarizers.[2,3] Our polarizer is a commercially polarizer: a Polarean 9800 continuous flow ^{129}Xe Polarizer. As this polarizer is used for current human studies, it cannot be modified because of the liability associated with these studies, which are typically performed under an investigational new drug application (IND) to ensure the safety of the gas. One of my research projects was to build a new continuous flow ^{129}Xe polarizer with modifications that mitigate xenon depolarization, while leading to enhanced cell residency time and polarization.

Section 3.2: Potential Sources of Polarization Loss

Section 3.2.1: Cell Residency Times

Our group is currently modeling what is happening inside of the optical cell during continuous-flow SEOP using a more realistic geometry of the optical cell, which includes not only the main body of the optical cell, but also the inlet pipes, which are expected to strongly affect the dynamics of the gas. We are also modeling Rb vaporization and distribution inside the cell, which in all previous models has been assumed to be homogenous and at thermal equilibrium. These simulations have shown that turbulence and gas recirculation within the optical cell, for our given cell geometry, occurs at very low flow rates. Recirculation leads to a reduction of the effective cell volume, and thus to a reduction of the residency time which, as discussed in section 2.2.1, will ultimately affect final xenon polarization. Residency time has so far been modeled assuming a plug flow in the cell, with $t_{res} = \frac{V_{cell}}{Flow\ Rate}$. Our flow simulations for the more realistic model of the optical cell shows that there is actually a distribution of residency times and that the distribution heavily depends on experimental conditions. As illustrated in Figure 3.1, while a small percentage of xenon atoms spend a lot more time in the cell, the majority of the xenon gas spends significantly less time in the cell than is assumed by the plug flow model. This decrease in residency time leads to a significant decrease in polarization. More importantly, under certain temperature conditions and flow rates, recirculation of the gas in the optical cell can lead, in the case of a non-homogenous distribution of Rb vapor, to a significant reduction in the final xenon polarization. This means that if designing a new cell, a much larger volume needs to be chosen to avoid gas recirculation while increasing gas residency time.

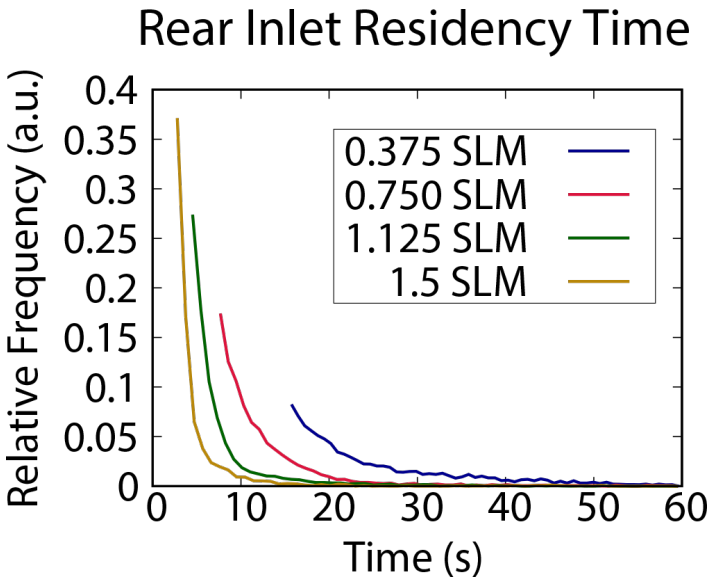

Figure 3.1. Plot of residency times for four different flow rates in a rear-inlet cell. Note that for all flow rates the majority of xenon atoms spend less time in the cell than on average with a very small percentage having very long residency times.

Section 3.2.2: Freezing and Thawing Times

Another possible source of depolarization occurs during collection and storage of polarized xenon in the solid state. As discussed in section 2.2.1, at a high field (above 1000G) and low temperatures (<120K) the T_1 of solid xenon is on the order of hours. These are the most favorable conditions for the accumulation and storage of polarized xenon in the solid state. During the process of freezing and sublimation, however, temperatures are no longer lower than 120K, and the longitudinal relaxation rate increases exponentially as interactions between ^{129}Xe and ^{131}Xe begin to dominate the relaxation process, as shown by Cates *et al.* 1990 (Figure 3.2).[40] To reduce relaxation during freezing and sublimation, these processes need to occur as fast as possible. To increase heat transfer between xenon and liquid nitrogen (freezing stage) or water (sublimation stage), we need a good thermal contact. To this end, we have replaced the commercial cylindrical cold finger with a spiral shaped cold finger that maximizes surface area through which heat is

exchanged. However, for larger batches (~1L), the xenon ice thickens, clogging the cold finger and causing thaws to take up to 5-10 seconds, during which a significant amount of polarization may be lost. To overcome this issue, the new polarizer model includes a much larger cold finger that enables the formation of a thin layer of xenon ice, while enabling the collection of larger quantities of xenon.

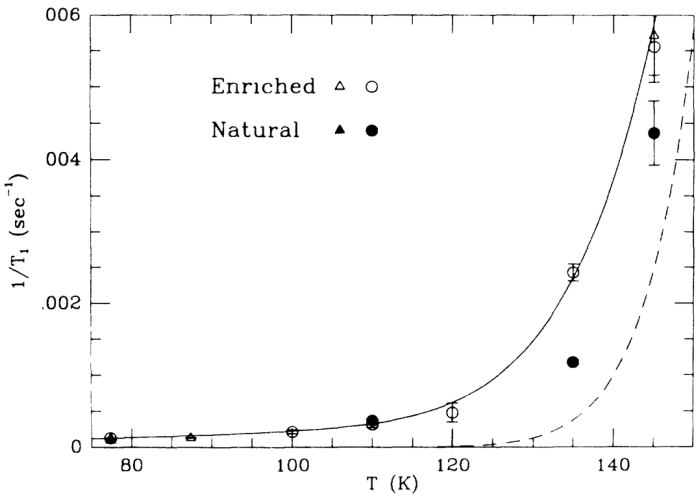

Figure 3.2 Spin-lattice relaxation rates, $1/T_1$, as function of temperature in both enriched and natural abundance ^{129}Xe. Note that, at high-temperatures (>120K), the relaxation rate increases exponentially. Figure taken from Cates *et al.* 1990.[40]

Section 3.2.3 Magnetic Field Gradients

Much work has been done within our group to identify potential sources of polarization loss that may explain the low polarization yield experienced with continuous flow SEOP set-ups.[2,3] As discussed in the section 2.2.1, the presence of magnetic field gradients has a well-established depolarizing effect on fast diffusing gases. Burant *et al.* 2016 looked at polarization losses cause by flow of gas in the inhomogeneous magnetic field present between the outlet of the optical cell and the inlet of the cold finger.[3] The relaxation rate in presence of a magnetic field gradient has a quadratic dependence on the strength of the gradient, and an inverse dependence on the strength

of the main magnetic field. Therefore, diffusing through regions, in which the magnetic field is weak and changing direction (zero crossing), can cause a significant loss of xenon polarization. Using COMSOL Multiphysics to modeling the magnetic field distribution in our polarizer and Monte-Carlo simulations to investigate gas depolarization from spin diffusion in these magnetic field gradients, we were able to show that our current set-up had two zero crossings. One, shown in Figure 3.3, was easily eliminated by a small change in the permanent magnet geometry, while the other (not shown here) requires a complete redesign of the polarizer.

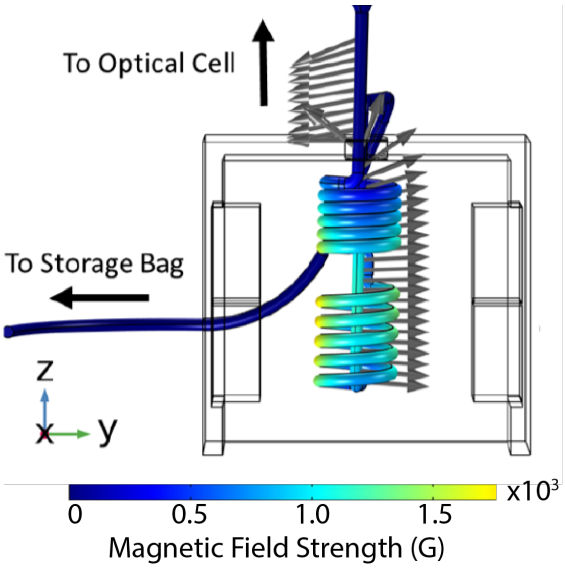

Figure 3.3 Shows strength and direction of the magnetic field experienced by the gas entering the cold-finger, housed within a permanent magnet in the Polarean 9800. Note the drastic change in the magnetic field orientation present on the top of the permanent magnet. Taken from paper Burant *et al.* 2016[3]

Section 3.3: Addressing Polarization Loss in Design

In light of the above observations, the new polarizer was designed such that: 1) It could house a larger optical cell, to increase residency time while reducing gas recirculation ; 2) it could accommodate a larger cold finger, to minimize freezing and thawing times; 3) It avoids zero-field crossing or drastic changes in magnetic field orientation along the path of the polarized xenon gas.

Section 3.3.1: Increasing Residency Time

The first and most straightforward way to increase the residency time in the optical cell is to increase the optical cell volume. However, if we just scale up the dimensions of our current optical cell, we would end up with a similar wide distribution of residency times. In order to narrow the distribution of residency times, we decided to increase only the cell length, leaving its diameter more or less unchanged. A narrow long cell is expected to give rise to a longer residency time and less recirculation. While this would seems like a relatively obvious, easy solution, increasing cell length introduces a number of design constraints on the new polarizer: 1) Increased oven size; 2) Increased region of homogenous magnetic field; 3) Increased laser power.

Section 3.3.1.1: Oven Size

The concept is extremely straightforward. In order to have a longer cell, we will need a longer oven. The oven should be adaptable to future changes in cell design, and should be built from aluminum so as to perturb minimally the magnetic field across the optical cell. The final design is shown below in Figure 3.4.

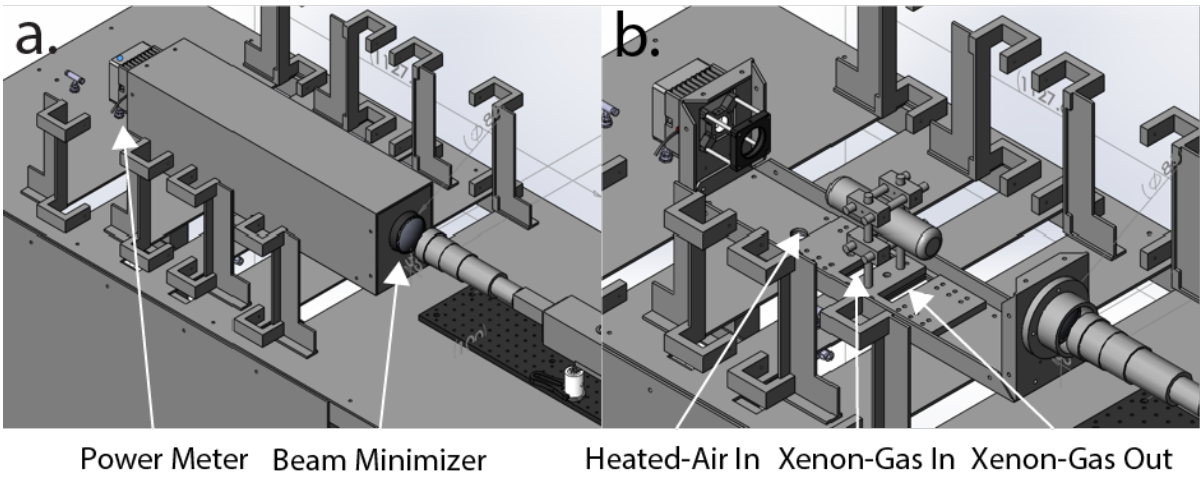

Figure 3.4 Solidworks model of the polarizer oven a.) with the cover on b.) with the cover off. The model shows the main components: power-meter/beam-dump, heated-air inlet, xenon gas in and out, beam minimizer, and adjustable stand.

The oven was built from aluminum sheet with the help of the UNC physics machine shop and insulated with fiberglass insulation. The adjustable stand was built from ULTEM plastic which has a glass transition at 217°C.

Section 3.3.1.2: Polarization Field

The strength of the polarization field does not impact xenon polarization. However, the direction of the field relative to the circularly polarized laser beam is important. The skew, defined as the angle between the direction of the magnetic field and the direction of light propagation, $\emptyset$, directly impacts rubidium polarization such that the Rb polarization:[41]

$$P_{Rb} \propto \cos\emptyset \quad (3.1).$$

A misalignment can have disastrous effects on the polarization cell. For example, a skew of only 3.1° can attenuate up to 50% of the laser light.[41] In order to avoid this misalignment, we needed to create a field that is aligned over the entire optical cell. For a short cell, such as the one

we have on the current commercial polarizer, a Helmholtz coil pair does a sufficient job. However, to produce a homogenous magnetic field over a much larger region, a multi-coil arrangement is needed. For that we chose the four coil Lee-Whiting arrangement,[42] which is characterized by a larger uniform magnetic field compared to Helmoltz coil of similar size, while still employing circular coils. The Lee-Whiting arrangement employs four circular coils with diameter, d, positioned at -0.4704d/-0.1216d/0.1216d/0.4704d, and with an ampere-turn ratios of 9/4/4/9. This arrangement produces a much larger homogenous field region when compared to Helmholtz system, as shown in Figure 3.5 by Kirchvink 1992.[42]

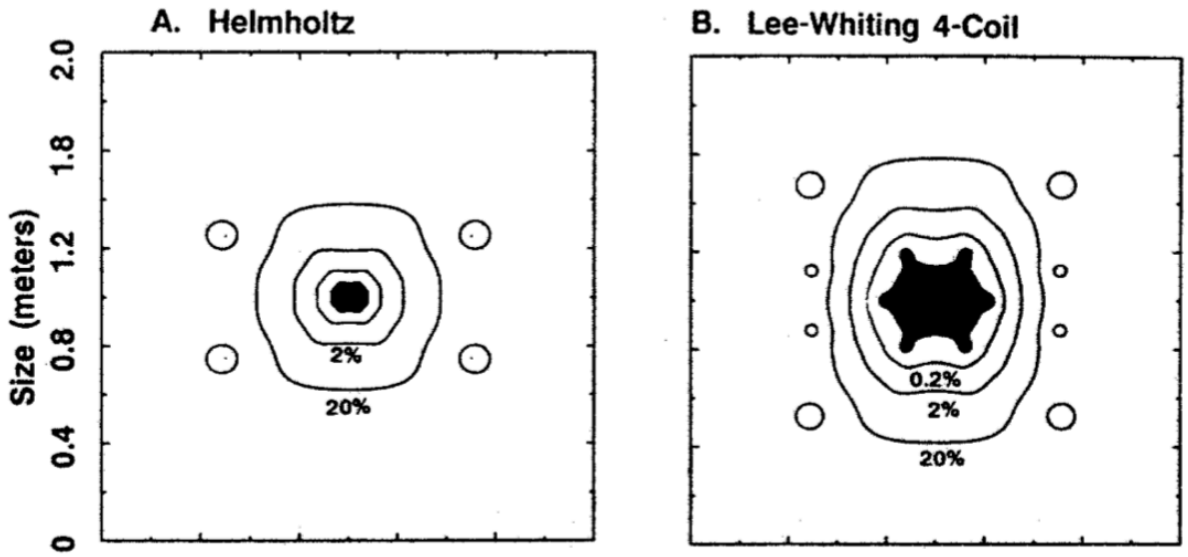

Figure 3.5 Results of numerical calculations of field homogeneity for a Helmholtz coil and a Lee-Whiting coil, with dark regions showing areas with field uniformity better than 0.02%. Taken from Kirchvink 1992.[42]

While the uniformity should allow for better characterization of the xenon polarization across the optical cell, the skew of the coil arrangement has a direct effect on final xenon polarization. To characterize the skew of this coil arrangement we used COMSOL Multiphysics. As shown in Figure 3.6, if we confine the optical pumping region to an area with a skew of less than 1°, the coil

configuration will allow for a pumping region that goes from a 10 cm by 20 cm long pumping area to a 30 cm by 50 cm long pumping area.

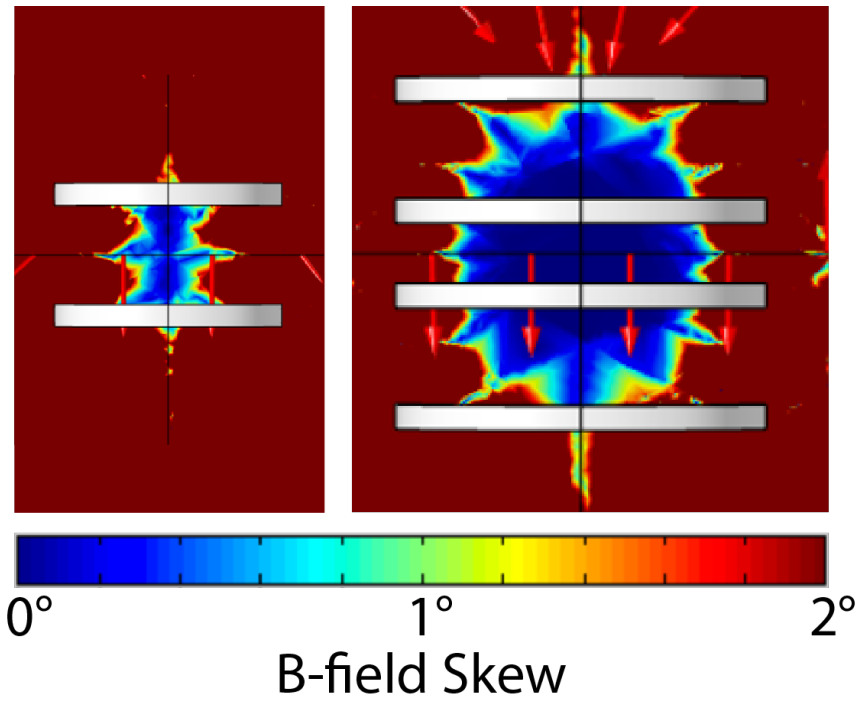

Figure 3.6 Map of B-field skew for current Helmholtz and Lee-Whiting Coil set-ups.

After designing the coils, the coils were built by Acutran LP, on a 23.6" ID Mold with 12 gauge square copper wire, inner coils had 128 turns and outer coils had 288 turns. Custom adjustable mounts were designed and built from aluminum and plastic by the UNC machine shop.

Section 3.3.1.3: Laser

The local laser power determines the local optical pumping rate. The local optical pumping rate, along with the spin destruction rate, determines the rubidium polarization. The local laser power decreases as it is absorbed by the rubidium as it passes through the cell. If there is not

enough power left at the back of the cell, un-polarized "dark" rubidium is left. Any "dark", un-polarized rubidium effectively reduces the length of the polarization region. To avoid that, we had to increase our laser power from 50W to 170W, a much higher power that can easily cover the entire cell length. The new laser is the QPC Brightlock diode laser with an internal Bragg grating for narrowing and wavelength stabilization, a ¼ wave plate in the optical train to produce the circularly polarized light, and a 3-inch diameter beam. After aquiring the laser, initial testing was done to characterize the laser.

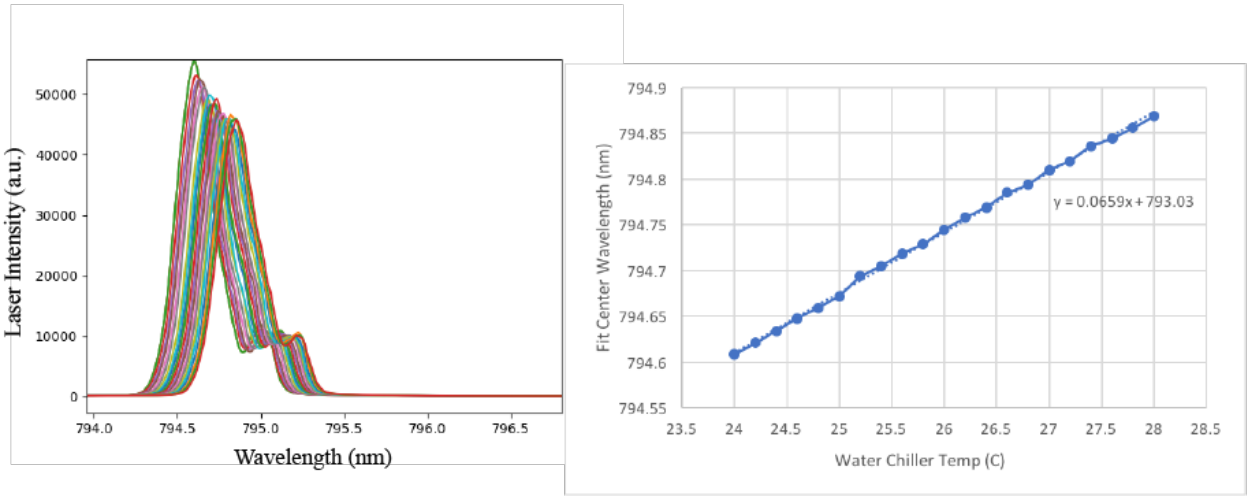

Figure 3.7 Initial laser testing showing how, by adjusting the chiller temperature one can make slight adjustments to the center frequency of the laser light. The laser light is characterized by a linewidth of less than 1nm at 170W. The chiller allows for a frequency adjustment of 0.66 ppm/°C.

Section 3.3.2: Increasing Cold-Finger Size

To increase cold finger size and therefore decrease thaw times for large batches of xenon, a larger, high-field permanent magnet set-up was needed. Based on our cold-finger size requirements, a permanent magnet array with a field larger than 1000G and length of larger than 10cm was needed. In addition, this strong field had to be constrained as much as possible in order to not perturb the homogeneity of the magnetic field in which the SEOP process occurs. To create

an array that maximized field strength and field confinement, we chose the eight-magnet Halbach array design. Halbach arrays are made from n-identical bar magnets and display high homogeneity, close to optimum use of mounted magnetization and very small stray field because of its extremely high flux return.[43] The new cold-finger magnet array consists of two 3-D printed bodies with eight neodymium bar magnets glued into place.

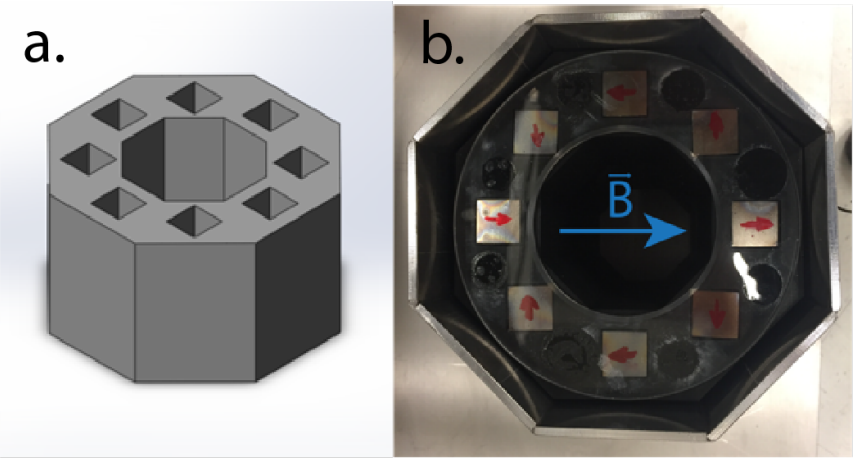

Figure 3.8 Picture of the a.) model and b.) 3-D printed neodymium magnet Halbach array.

Section 3.3.3: Post-Polarization Flow Path

To find a post-polarization flow path such that the polarized gas does not experience a zero-field crossing or drastic change in magnetic field orientation, we modeled the magnetic fields distribution along the polarized gas flow path for different orientations of the Lee-Whiting polarization coils and the new Halbach array. Computations of the magnetic field distribution were run in COMSOL Multiphysics. As shown in Figure 3.9, these simulations showed that, in order to avoid abrupt changes in the magnetic field orientation along the polarized gas flow path, the Halbach array had to be placed directly beneath the optical cell.

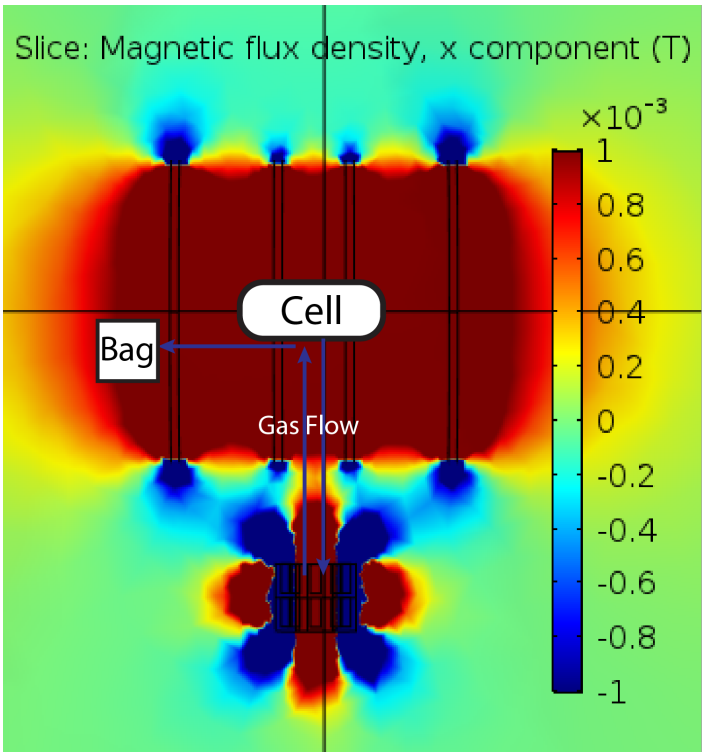

Figure 3.9 A map of the x-component of the magnetic field showing the field produced by the permanent magnet joining the field of the Lee-Whiting coils to create a gas-flow path without a change in field direction when placed directly beneath the polarization cell.

Section 3.4: Addressing Polarization Loss in Build

The new design implements all of the changes needed to increase polarization using a non-magnetic aluminum frame. The new polarizer frame and oven were first completely modeled in Solidworks before being built by the UNC physics machine shop. After delivery, gas tubing, as shown in Figure 3.11, was mapped in Solidworks and assembled using Swagelok fittings. Copper tubing (1/4 in OD) and brass valves were used for all tubing that does not come into contact with polarized gas. For the tubing section from the polarization cell exit to the first valve, an oxygen-cleaned anodized aluminum valve and tubing were used, while for the rest of the polarized gas path, we used plastic PTFE tubing and PFA Swagelok valves.

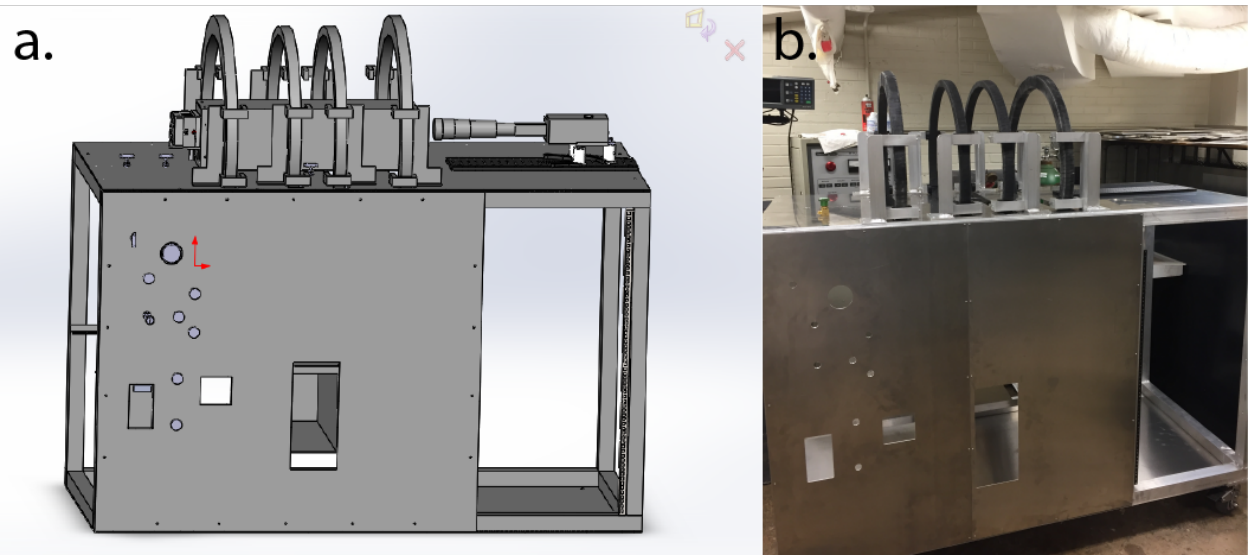

Figure 3.10 a. Solidworks model of the polarizer frame **b.** aluminum frame built by the Physics shop.

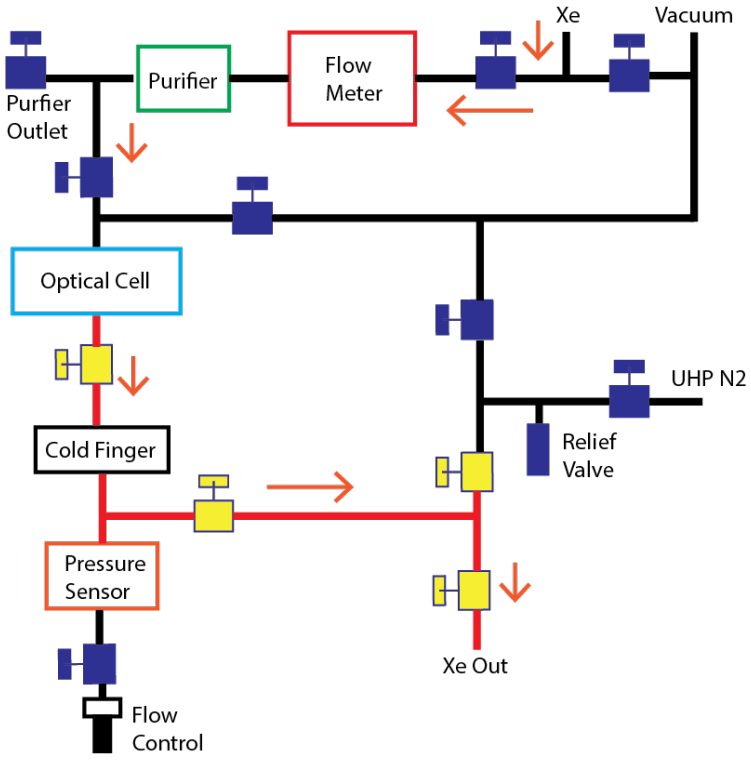

Figure 3.11 A map of the tubing assembly. Black indicates tubing in copper, while red indicates tubing in PTFE plastic and PFA valves, that are known to minimize gas depolarization. The orange arrows show the xenon gas mixture path. The other tubing allows for purging of oxygen and contaminants using UHP N_2 from gas lines.

Section 3.5: Future Work

After initial testing of the laser, it became apparent that there was significant degradation in the laser beam quality. Specifically laser light intensity began to drop after the first few uses of the laser. The newly designed laser was sent back to the manufacture, QCP. Future work involves characterization of the parameters space of the polarizer with the new laser and the current polarization cell. After this has been completed, a new, longer cell will need to be designed, built, filled with rubidium, and characterized. Comparison of the experimental polarization results, along with NMR spectroscopic measurements of xenon polarization across the cell length, and Rb density across the cell length, will be used to further optimize the geometry of the optical cell and Rb distribution. Once optimization is completed, the polarizer will be moved into the small animal imaging facility for use in small animal MRI and NMR experiments, before its use for human experiments.

CHAPTER 4: COMPARISON OF ^{129}XE WITH ^{19}F IN CYSTIC FIBROSIS LUNG DISEASE

With the improvements in gas polarization, MRI with hyperpolarized (HP) gas has allowed for 3-dimentional high-resolution imaging of void spaces in the lungs during a single breath-hold. Hyper-polarizaed ^{129}Xe gas MRI has been shown to provide regional information about lung ventilation function that pulmonary function tests alone cannot provide,[44] measuring a range of functional biomarkers such as the ventilation defect percentage (VDP).[45] In addition, thanks to the relatively large tissue-solubility and large chemical shift (~200ppm) of ^{129}Xe, dissolved-phase HP ^{129}Xe imaging is also feasible,[12,46,47] and could potentially provide valuable insights into the pulmonary gas-exchange processes in both healthy and CF lungs. Despite these improvements, gas hyperpolarization is still a technically difficult process.

Fluorine-19 (^{19}F) imaging has been proposed as a simpler, thermally polarized alternative to HP gas for void-space imaging. This is possible because ^{19}F has a higher gyromagnetic ratio (~3.4 times ^{129}Xe), high natural abundance (100%), higher spin-density than ^{129}Xe, and very short T_1 (1-20 ms compared to ~20 s for ^{129}Xe).[4] The very short T_1 allows for the use of very short repetition times (TR), thus signal averaging to enhance the ^{19}F image SNR. All taken together, these properties partially make up for the difference in polarization between the two gases, allowing for gas-phase imaging though at a much lower resolution. Feasibility studies, performed in humans, have produced promising void space images upon inhalation of gas mixtures containing 79% sulfur hexafluoride (SF_6) or perfluoropropane (C_3F_8 or PFP) and 21% oxygen (O_2).[48] Without the need for a complicated hyperpolarizer, ^{19}F gas imaging could potentially provide the same ventilation

information as ^{129}Xe.[49] The ^{19}F ventilation images, which are typically much lower in resolution and signal-to-noise ratio (SNR) when compared to ^{129}Xe images, are typically acquired over the course of multiple breaths, which allow the acquisition and averaging of multiple images to further increase SNR.[49,50] In addition, to increase SNR further, very short echo time pulse sequences and phased-array RF coils are used.[51] However, phased-array RF coils often lead to image artifacts due to inhomogeneities in the spatial sensitivity of the coil array.[4] Ventilation defects have been observed in diseased populations using ^{19}F imaging[52] and promising comparisons between ^{19}F and ^{129}Xe ventilation images have been recently performed in healthy volunteers.[50] However, because of the limited resolution and SNR achievable with ^{19}F imaging, it is still an open question whether ^{19}F images can provide the same functional biomarkers such as VDP in diseased populations.[50]

Section 4.1: Biological Motivation

Cystic fibrosis (CF) is caused by the most common, fatal, single gene defect in Caucasians. In CF subjects, there is a defect in the chloride and bicarbonate ion transport of epithelial cells. This causes issues with secretions throughout the body, and in the lungs specifically, the airway epithelium is vulnerable to fluid hyperabsorption. This leads to the production of abnormally concentrated and viscous mucus. Mucus in small airways, that cannot be cleared by cough, accumulates, clogs airways, and results in local infections and inflammation.[53,54]

High-Resolution Computed Tomography (HR-CT) is currently the gold standard for quantitative morphological measurements of the lungs; however, the risk associated with repeated radiation exposure limits the use of CT, particularly in serial imaging studies and longitudinal studies monitoring disease progression in the relatively young CF population.[55] Magnetic Resonance Imaging (MRI) is a potentially ideal modality for analyzing lung structure and function

as it is non-invasive, non-ionizing, and therefore can be performed in longitudinal studies. Although historically, structural lung MRI has been poor because of low density and extremely short transverse relaxation time of water protons in the lungs, advances in ultrashort-echo-time (UTE) and zero-echo-time (ZTE) techniques have allowed for structural imaging of lung parenchyma, blood vessels, and mucus plugging.[56] In addition to structural information, MRI has the potential to offer functional information in the form of ventilation imaging.[57] Ventilation defect percentage from ^{129}Xe MR imaging has been shown to correlate with markers of disease severity such as lung clearance index in pediatric subjects with cystic fibrosis.[58] This allows ^{129}Xe MR possibly to provide more specific and accurate information on CF treatment response in interventional trials. The scope of this work was to perform a comparison between ^{19}F and HP ^{129}Xe gas MRI for the detection of lung ventilation defects in subjects with CF at 3T.

Section 4.2: Imaging in CF patients

This study was approved by the research ethics board at the UNC Chapel Hill (number 17-2569) and all participants provided written inform consent to participate in the study at the time of the enrollment. In collaboration with the UNC Cystic Fibrosis Center, we enrolled a total of eight participants diagnosed with cystic fibrosis to undergo a study where both ^{19}F and ^{129}Xe ventilation images were taken in a single imaging session. Participants had to be ≥ 18 years of age, non-smokers (<10 pack year history and no active smoking in the past year), displaying stable lung disease as evidenced by no change in respiratory medications or change in FEV1, (Forced Expiratory Volume) of >15% from baseline over the preceding 4 weeks prior to enrollment, and having a baseline FEV1 >70% of predicted. Before the imaging session, all vital signs, including height and weight, were obtained by the research coordinator. A limited physical exam (ENT, cardiovascular, and pulmonary) was performed by an MD or PA. Right before and right after the

imaging session, all subjects underwent also a spirometry test, according to the standards set forth by the American Thoracic Society. All imaging was performed on a Siemens PRISMA 3T MR scanner (Siemens AG) with multinuclear capabilities and subjects were randomized to begin with ^{19}F or ^{129}Xe imaging.

Three-dimesnional ^{1}H scans were run before and after each ^{129}Xe and ^{19}F scan to obtain anatomical information and to facilitate co-registration of ^{129}Xe images with ^{19}F images. These ^{1}H images were acquired by using a 3D stack-of-spirals GRE sequence with 5° excitation flip angle, a repetition time of 2.42 ms, an echo time of 0.05 ms, a 224 by 224 acquisition matrix, and with a resolution of 2.1 mm x 2.1 mm x 2.5 mm.

Section 4.2.1: ^{19}F Imaging

The ^{19}F acquisitions were performed using an ^{19}F-tuned, 8-channel chest coil (ScanMed, NE). Prior to placing the subject in the scanner, a home-built ^{19}F phantom, was scanned for quality assurance and to establish the ^{19}F center frequency. Subjects were placed inside the scanner and inhaled a pre-mixed, medical grade gas mixture (79% PFP to 21% oxygen) delivered using a continuous-breathing, custom gas delivery device shown in Figure 4.1 as described in Halaweish *et al.* 2013.[52]

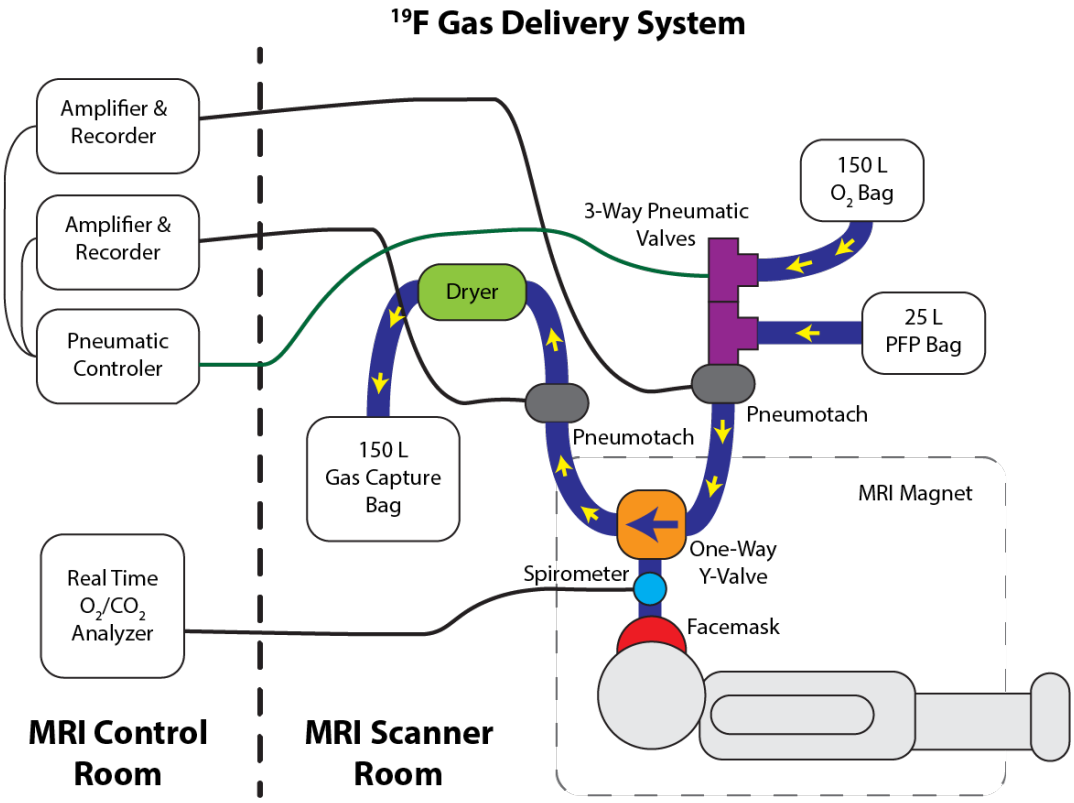

Figure 4.1 Schematic representation of the gas delivery and physiologic monitoring setup used for ^{19}F lung imaging. Physiologic monitoring systems were located in the MRI control room. The pneumatic valve controls were used to switch between normal room-air breathing and PFP breathing, as determined from the respiratory trace recorded by the pneumotach. Real-time recording of blood-oxygen levels, heart rate, inhaled oxygen, and CO_2 levels provided a continuous evaluation of the imaging sessions and the respiratory efforts of the subject.

The PFP was administered with the aid of a full-face Hans Rudolph 6500 V2 disposable oral-nasal non-invasive ventilation mask with anti-asphyxia vents and a standard Douglas Bag system. A non-rebreathing valve allowed the inspired gas to be switched easily from PFP to room air. Prior to ^{19}F imaging, subjects took two controlled tidal volume breaths of the contrast gas followed by a 12-second breath-hold and scan, during which time images were acquired. A total of five such imaging cycles during PFP inhalation (wash-in) were performed, followed by an identical five cycles during inhalation of room air (wash-out). For the entire duration of the imaging scan, ventilation was monitored using a pneumotachometer, along with blood oxygenation, exhaled

CO_2, and heart rate. Also, 3D images were acquired using a 2D GRE sequence with a 70° flip angle, an echo time of 1.62 ms, a repetition time of 13 ms, a 64 by 64 acquisition matrix with a 130 Hz/pixel bandwidth, and a resolution of 6.25mm x 6.25mm x 15mm.

Section 4.2.2: ^{129}Xe Imaging

The ^{129}Xe imaging was performed using a flexible ^{129}Xe-tuned quadrature chest coil (Clinical MR Solutions, WI). For each subject, two images were acquired, each during a single 12-second breath hold of 750 ml of isotopically enriched ^{129}Xe, polarized up to ~14% with a Polarean 9800 129Xe Polarizer (Polarean, Inc., Durham, NC), mixed with 250ml of N_2. During the first inhalation, the ^{129}Xe center frequency was acquired followed by a low-resolution 3D image. A high-resolution image was acquired during the second inhalation, 10-40 minutes from the first inhalation. The two 3D ^{129}Xe images were acquired using 2D GRE sequences with a 10° excitation flip angle, a repetition time of 9ms, an echo time of 4 ms, a resolutions of 2.2 mm x 6.4 mm x 21.0 mm (low resolution image) or 2.2 mm x 4.4 mm x 10.5 mm (high resolution image), and with a 128 by 128 acquisition matrix with a bandwidth of 260 Hz/pixel.

Section 4.3: Definition of Ventilation Defects

In order to quantify ventilation defects from MR images with the two gases, a clear procedure for defining ventilation defects in both ^{19}F and ^{129}Xe imaging needed to be established. For this study, after evaluating different methodologies typically used for this type of image analysis, we defined regions of ventilation defects as those regions in which signal intensity was within the 95th percentile of the noise distribution.[49]

Defining ventilation defects using metrics previously used for ^{129}Xe ventilation studies proved to be difficult because of the large difference in SNR between images acquired with the two gases. K-means binning and other algorithmic VDP segmentation analysis methods typically depend on image noise level. Specifically, these techniques break down when image SNR is low, as in ^{19}F images. Additionally, the use of a multi-channel ^{19}F lung coil, led to severe B_1 inhomogeneities. These inhomogeneities are typically subject dependent and coil position dependent, and cannot be easily corrected. These B_1 inhomogeneities made ventilation thresholds dependent on lung position, preventing the application of typical linear binning techniques that delineate regions of high, medium, and low intensity areas based on an universal thresholds.[59] Moreover, retrospective bias-field estimation techniques, often used to reduce subject-dependent B_1 effects in ^{129}Xe studies,[59] create spurious gas filled regions from noise level intensity in low-SNR ^{19}F images. This should not be surprising as these techniques have been developed for high-SNR images, and in ^{19}F images, SNR is on the order of the bias-field correction, artificially changing image intensities by a factor of 2 or 3.[59,60] Another difficultly was deciding which time points in the continuous-breathing ^{19}F ventilation images to evaluate. To mitigate this problem, we decided to compare multiple ^{19}F time points, specifically the early-breath as well as late-breath maximum-ventilation ^{19}F images.

Registration and masking of the images was performed using MIM Software (Cleveland, OH). For both ^{129}Xe and ^{19}F imaging sessions, ^{1}H lung masks were generated via a semi-automated segmentation of the ^{1}H lung-cavity images, using a simple region-growing algorithm. Following generation of the lung masks, the ^{1}H images were registered to their ^{129}Xe and ^{19}F equivalents through the use of a rigid registration transform, allowing for matching of anatomic and functional coverage. The ^{1}H lung cavity images were used as lung masks to eliminate noise regions outside

the lung region of interest (ROI). For the max-vent image, the two highest intensity ^{19}F time points were averaged to increase SNR, for the early-breath image, the first ^{19}F time point to show ^{19}F signal was used.[50] Finally, ^{129}Xe and ^{19}F imaging sessions were registered through the use of a rigid registration transform on their respective ^{1}H images, shown in Figure 4.2. The registered images and masks were then exported to MATLAB (version 2017b; MathWorks, Natick, MA) for further processing using in-house scripts. Specifically, all voxels with an intensity below the 95th percentile of the noise distribution were labeled as ventilation defects.[49] The noise distribution was determined from an ROI defined outside the lung regions. The VDP was then defined as the percentage of the lung volume labeled as a ventilation defect. The SNR was calculated as the ratio of the 90th percentile of the lung interior distribution to mean noise signal.

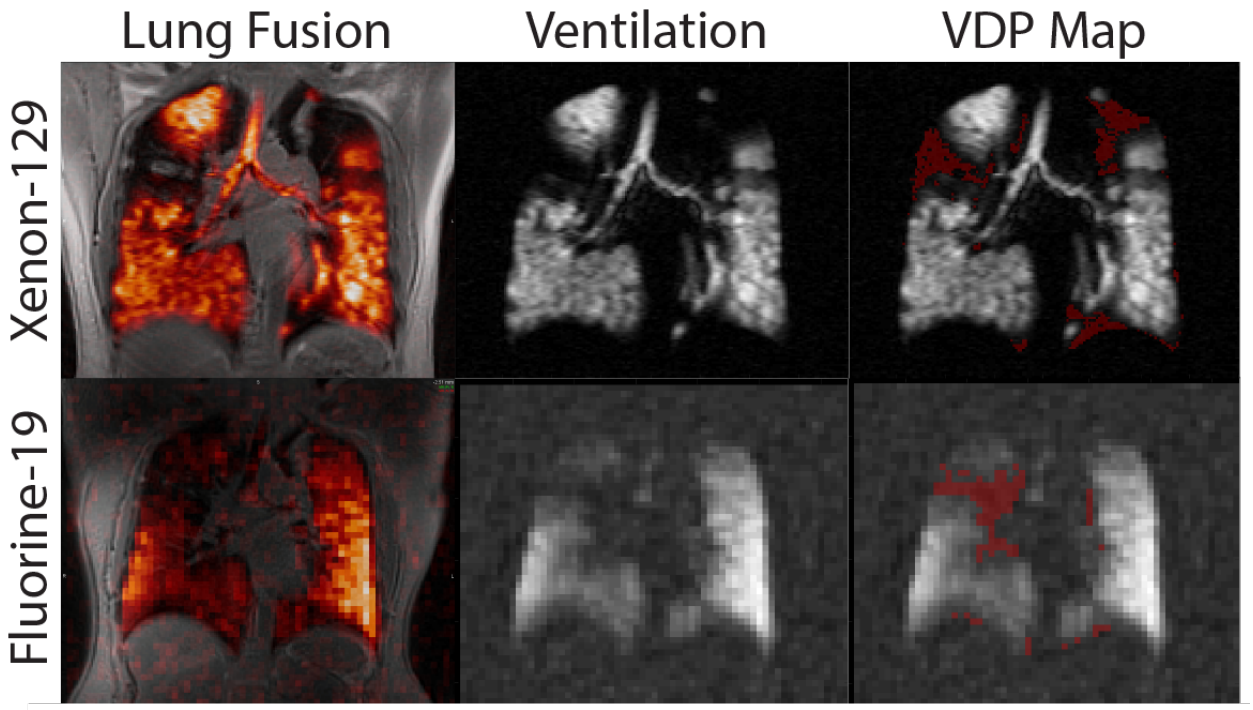

Figure 4.2 Representative images showing fusion of anatomic and high-res ^{129}Xe and max-vent ^{19}F images. Masks were made from the anatomic images to determine lung volumes and applied to the ventilation images shown. A threshold was applied to define regions of ventilation defect creating ventilation defect maps (red masks). VDPs were calculated as the percentage of ventilation defect in the anatomic mask.

Section 4.4: Ventilation Defect Maps

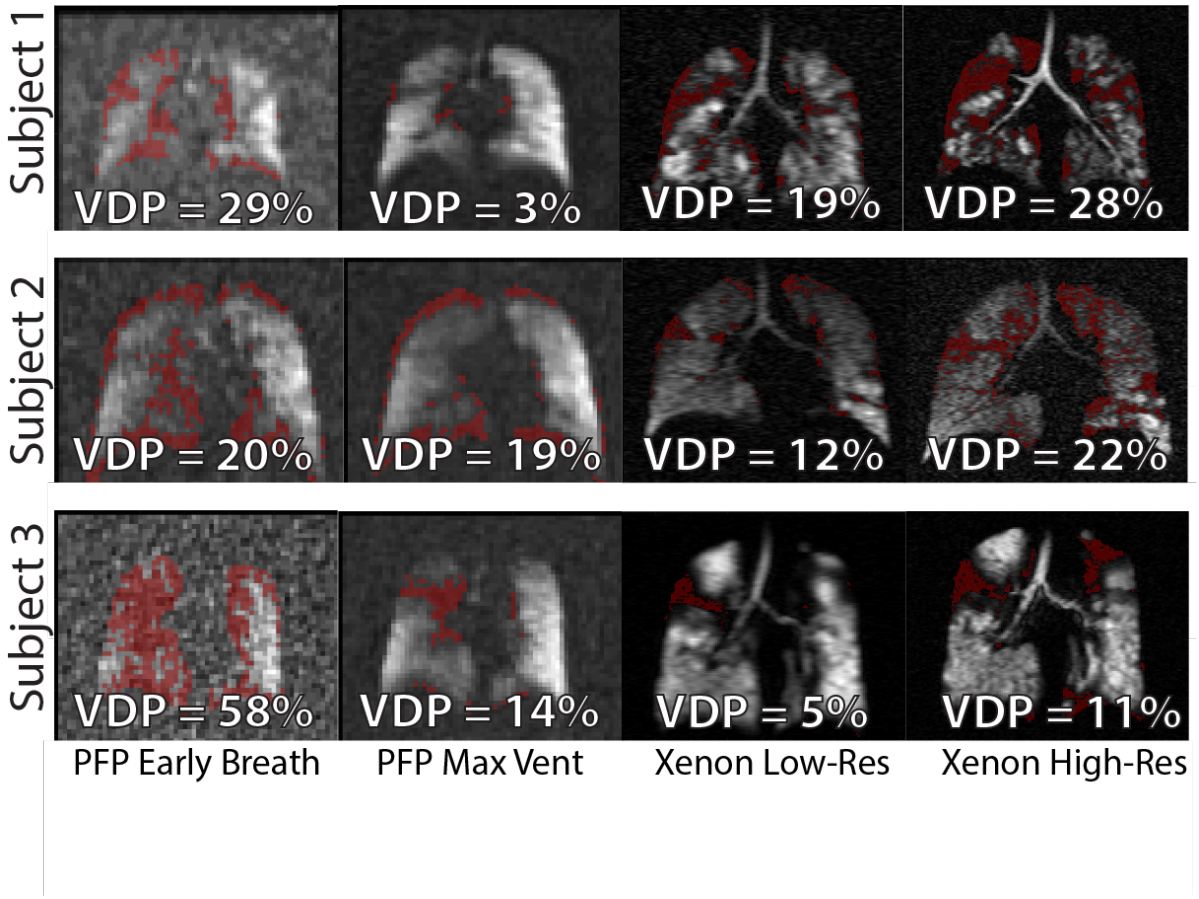

Figure 4.3 Images show ventilation defects maps (red masks) from early-breath and max-vent ^{19}F gas and high-res and low-res HP ^{129}Xe gas MR imaging, in three subjects. The VDPs in early-breath images are higher than in max-vent images, and high-res ^{129}Xe images display higher VDPs than low-res images. Similar defect regions can be seen in many images.

Comparing defects in low-res and high-res ^{129}Xe images, low-res images show consistently lower VDPs; however, defect locations are consistent with that of the high-res images. This trend was noted across all subjects, as shown in Figure 4.5, with plots of low-res vs. high-res VDP displaying a significant (r^2=0.72, p=0.04) with a slope of 0.53 and the Bland-Altman plot showing a significant (p=0.0035) mean difference in VDP of -8.9% that further decreases with increasing VDP.

Ventilation defects were not consistent between ^{129}Xe and ^{19}F images, and defect detection capability of ^{19}F images varied from subject to subject when compared to ^{129}Xe images, as shown in Figure 4.3. The SNR of the ^{19}F images was significantly lower than that of the ^{129}Xe images and SNR in max-vent ^{19}F images was significantly higher than in early-breath ^{19}F images (p=0.049), as shown in Figure 4.4.

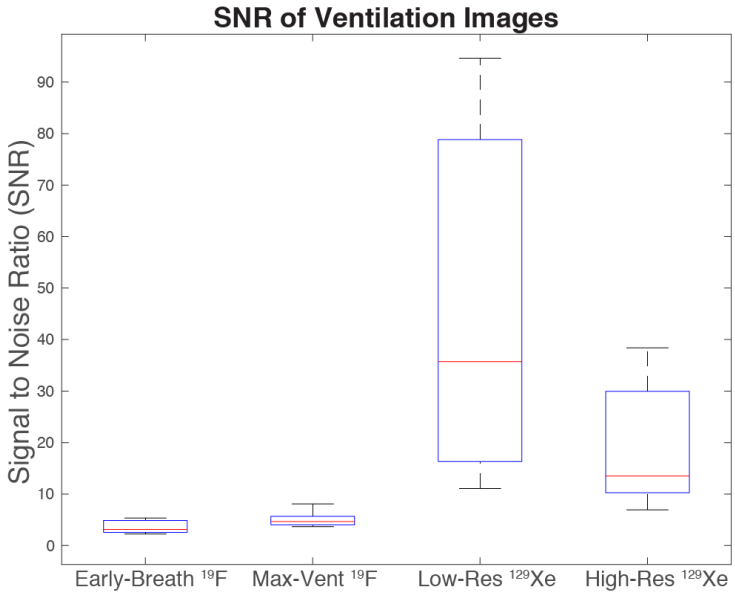

Figure 4.4 Boxplot showing distribution of ventilation images SNRs across all eight subjects. Significant differences can be seen between early-breath and max-vent ^{19}F imaging (p=0.04) as well as between ^{19}F and ^{129}Xe imaging (p<0.001). The mean SNRs for all four methods: early-breath ^{19}F, 3.6 ± 1.2; max-vent ^{19}F, 5.0 ± 1.5; high-res ^{129}Xe, 19.1 ± 12.1; low-res ^{129}Xe, 42.4 ± 31.3.

In Subject 1, the ventilation defects from early-breath ^{19}F images matched that of the high-res ^{129}Xe, whereas the max-vent ^{19}F shows almost complete filling of the lung airspaces, showing only 3% defect. In Subject 3, the ventilation defects from the max-vent ^{19}F matched that of the high-res ^{129}Xe whereas the early-breath ^{19}F showed nearly the entire right lung as a defect with 68% defect. This inconsistency between ^{19}F and ^{129}Xe image defects was shown across all subjects.

Max-vent ^{19}F vs. high-res ^{129}Xe VDP displayed no significant correlation with an r^2=0.10 and p=0.82 and the Bland-Altman plot showing a significant (p=0.022) mean difference in VDP of -10% for Max-vent ^{19}F with respect to high-res ^{129}Xe. The range of VDP differences is large at 29% with individual subjects displaying larger max-vent ^{19}F VDPs. Plots of early-breath ^{19}F to high-res ^{129}Xe VDP displayed no significant correlation (r^2=0.13 and p=0.38) with Bland-Altman plot showing no significant (p=0.33) mean difference in VDP. The early-breath ^{19}F to high-res ^{129}Xe correlations were dominated by couple of low SNR images with huge VDPs in ^{19}F illustrated by Subject 3 in Figure 4.3.

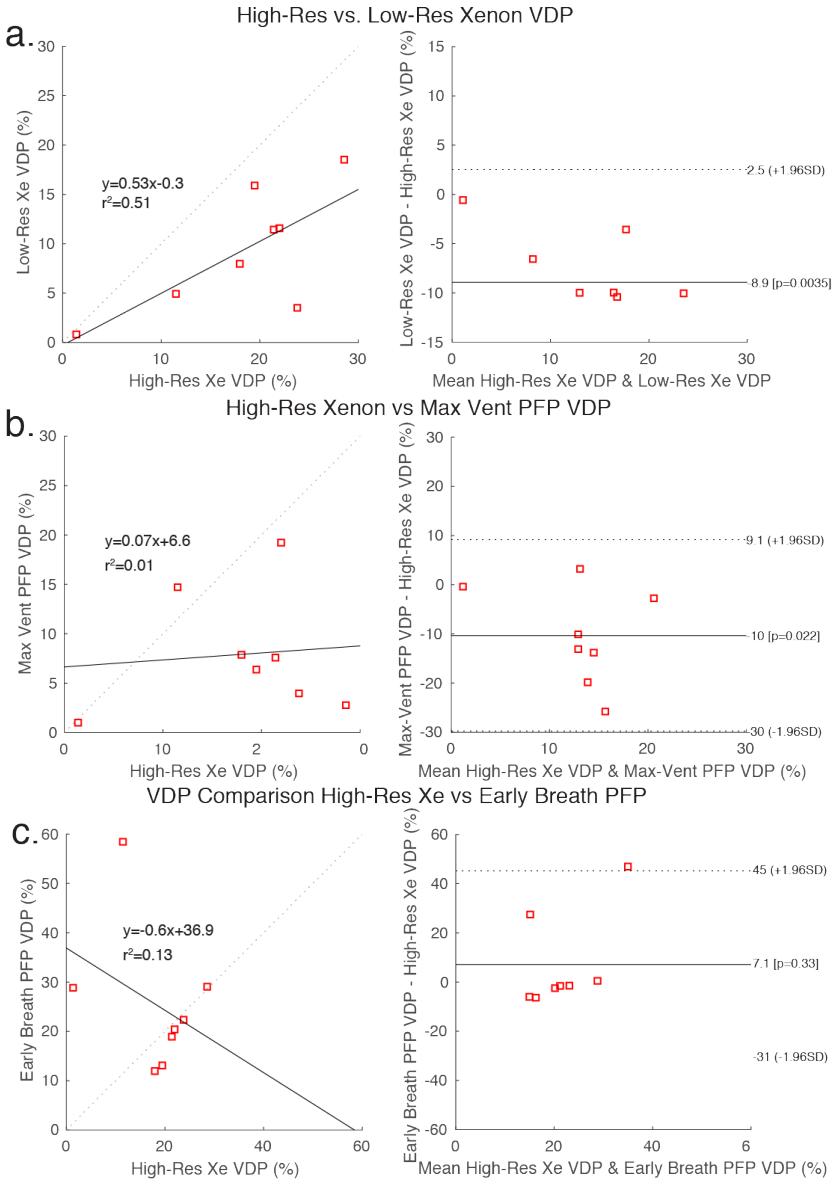

Figure 4.5 **a.** Correlation and Bland-Altman plots showing comparison of VDP measurements from high-resolution ^{129}Xe and low-resolution ^{129}Xe images including all subjects. Correlation plot shows a linear fit between measurements. The calculated correlation coefficient was 0.51. The Bland-Altman plot shows estimated bias (-8.9%) and 95% limits of agreement (±11%) that increases with increasing mean VDP. **b.** Correlation and Bland-Altman plots showing comparison of VDP measurements from high-resolution ^{129}Xe and max-ventilation ^{19}F images in all subjects. Correlation plot shows a linear fit between measurements. The calculated correlation coefficient was 0.01. The Bland-Altman plot shows estimated bias (-10%) and 95% limits of agreement (±19%). **c.** Correlation and Bland-Altman plots showing comparison of VDP measurements from high-resolution ^{129}Xe and early breath ^{19}F images in all subjects. Correlation plot shows a linear fit between measurements. The calculated correlation coefficient was 0.13. The Bland-Altman plot shows estimated bias (7%) and 95% limits of agreement (±38%).

If the subjects displaying large overestimations of early-breath ^{19}F VDP relative to high-res ^{129}Xe VDP are removed, there is a significant correlation between the VDPs measured by the two imaging gases, with an r^2=0.97 and p=0.0004 with a significant (p=0.04) mean difference of -2.9% shown in Figure 4.6. The Bland-Altman plot displays an underestimation of early-breath ^{19}F VDP at lower mean VDP that approaches zero with increasing VDP.

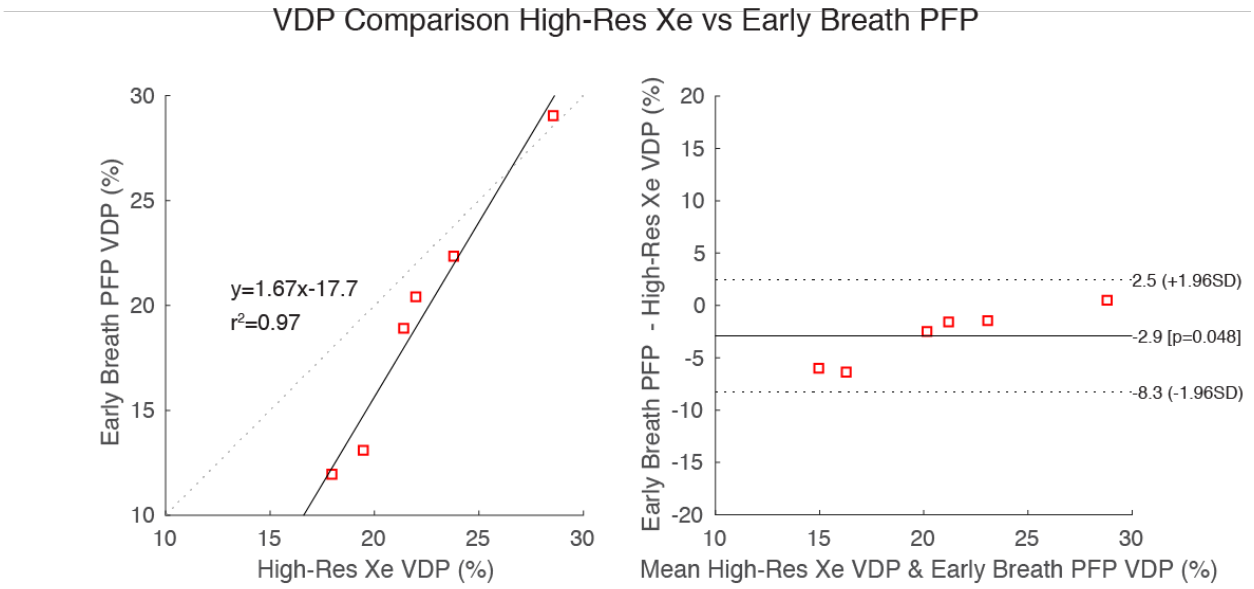

Figure 4.6 Correlation and Bland-Altman plots showing comparison of VDP measurements from high-resolution ^{129}Xe and early-breath ^{19}F in subjects with and SNR > 2.5. Correlation plot shows a linear fit between measurements. The calculated correlation coefficient was 0.97. The Bland-Altman plot shows estimated bias (-2.9%) and 95% limits of agreement (±5%) that increases with decreasing mean VDP.

Section 4.5: Discussion

This study reports the first comparison of VDP values obtained from ^{19}F and HP ^{129}Xe gas MRI in subjects with cystic fibrosis. Both ^{19}F and HP ^{129}Xe gases lead to MR images with large differences in SNR. As previously discussed, the difference in SNR was a major limitation in this study, which prevented the application of typical ventilation binning techniques that have been

used for HP ^{129}Xe gas ventilation imaging. These techniques could not be applied to ^{19}F images as they break down at very low image SNRs. For this reason, a threshold of the 95th percentile of the noise distribution, was used.[49]

Direct comparison between single breath ^{19}F images and single breath ^{129}Xe images, although tried in a few subjects, could not be made because of the intrinsically low SNR of ^{19}F images. To mitigate this problem, we decided to compare single breath ^{129}Xe images to both averaged max-vent ^{19}F images and early-breath ^{19}F images as defined in Section 4.3. When evaluated across all subjects, early-breath ^{19}F and high-res ^{129}Xe VDP values displayed no significant correlation. However, a more in depth analysis revealed this comparison to be skewed by two subjects, whose early-breath images were characterized by a very low SNR. In these subjects, the inherently low SNR, coupled to B_1-inhomogeneities, reduced the signal from ventilated regions to noise level, leading to an overestimation of VDP by up to 50%. However, when these two subjects were removed from the analysis, as in Figure 4.6, a strong correlation was seen between early-breath ^{19}F and high-res ^{129}Xe VDP. The slope of the linear fit, however, was greater than one, with the Bland-Altman plot showing the early-breath ^{19}F imaging less sensitive to defects in lungs with low VDPs. This insensitivity, however, goes away as VDP increases. This relative insensitivity of ^{19}F to smaller defects is caused partially by the lower resolution of ^{19}F, which leads to partial volume effect, as demonstrated by the comparison between low-res and high-res HP ^{129}Xe images, and to the diffusion of ^{19}F and collateral ventilation that inevitably occur during the inhalation over multiple breaths. This suggests that, early-breath ^{19}F may be a viable substitute to HP ^{129}Xe MRI in subjects with large ventilation defects, provided that high SNR ^{19}F images can be acquired.

One potential solution to increasing ^{19}F SNR is to average multiple breaths as we did for the max-vent image. As shown in Figure 4.4, signal averaging from multiple breaths leads to a

significantly higher SNR (p<0.05). However, image averaging from multiple breaths also leads to reduced sensitivity to small ventilation defects as ^{19}F gas diffuses into slow filling lung airspace regions. For this reason, max-vent ^{19}F VDP was not correlated with the high-res ^{129}Xe VDP. A few subjects had ventilation defects that appeared in both high-res ^{129}Xe VDP and max-vent ^{19}F as shown in Figure 4.3 (Subject 3); however in most, the ^{19}F gas filled the majority of defects (Subject 1).

When measuring VDP values, image resolution also seems to play a role. In our study, direct comparison of VDP value from high-res ^{129}Xe and low-res ^{129}Xe ventilation images allowed for the isolation of the effect of resolution on VDP. As expected, relative to high-resolution scans, low-resolution scans are more prone to partial volume effects and consistently underestimate VDP. This underestimation is larger at higher VDPs, with the trend showing low-res scans underestimating VDP by about half regardless of VDP. This trend suggests that while we would expect the lower resolution to impact ^{19}F VDP, we would expect underestimation to be higher at larger VDPs. This is the opposite of the trend in high-SNR early-breath ^{19}F VDPs. This suggest that while resolution does contribute to an overall underestimation, the specific underestimation at low VDPs in early-breath ^{19}F imaging is also a result of differences in gas-dynamics and image SNR. Further work would be needed to isolate the contributions.

Other issues encountered in this study can be attributed to the co-registration of ^{19}F and ^{1}H images. Proton images of the thoracic cavity and gas ventilation images were obtained during different breath-holds. As a result, differences in lung inflations led to co-registration errors, particularly in ^{19}F images, where the participant breathed freely, as opposed to a set volume of gas, as for the acquisition of the ^{129}Xe/^{1}H image pairs. Differences in lung inflation led to additional ventilation defects around to the lung edges, which artificially inflated VDP (Figure 4.3, Subject

2). Thus there may be additional benefit from the acquisition of anatomical and ventilation images within a single breath-hold, which has already been shown for HP ventilation imaging.[61,62] Recent work done to accelerate ^{19}F image acquisition could allow for acquisition of $^{19}F/^{1}H$ images during a single breath hold.[63]

Section 4.6: Conclusion

In CF subjects, ^{19}F ventilation images are characterized by significantly lower SNR and resolution compared to HP ^{129}Xe images. The low SNR and low resolution of ^{19}F images makes image acquisition and ventilation defect analysis more difficult, but with improvements in ^{19}F ventilation imaging, early-breath ^{19}F has potential for mapping large ventilation defects in cystic fibrosis patients. The VDP values obtained from early-breath ^{19}F ventilation images with SNR>2.5, although underestimated, correlate well with VDP values from HP ^{129}Xe scans. When, in an effort to further increase SNR, the averaging of more breaths is used, the majority of ventilation defects disappear.

CHAPTER 5: BROWN ADIPOSE TISSUE DETECTION AND FAT FRACTION

Once xenon enters the lungs, it easily diffuses across tissue barriers and enters the blood stream. Once in the blood stream, it is quickly carried to organs and tissues throughout the body. The ability to detect hyperpolarized xenon in distal organs depends on the relaxation of xenon in blood and in the given tissue. Xenon relaxation in blood is less than 10s, while in tissues it varies depending on tissue composition. For example, the T_1 of xenon dissolved in fat is quite long, as measured in our lab, ranging from 30s at 3T to about 60s at 11T. For other tissues it is typically lower, but as long as xenon accumulates quickly enough into the tissue, dissolved-phase xenon spectra and images can be acquired. The rate of xenon accumulation into a given tissue is typically a function of the blood flow to the tissue and the solubility of xenon in the tissue. Using xenon-enhanced CT our group has confirmed that the lipophilic xenon accumulates very rapidly in brown adipose tissue (BAT) when BAT thermogenesis is stimulated. Stimulation of BAT thermogenesis leads to an enhancement in blood flow to BAT of more than 10-fold. The time dependence of xenon concentration in this tissue, and in any other tissue, can be easily computed using the Kety-Smith equation, once the partition coefficient of xenon between tissue and blood, and the flow to the tissue is known (Figure 5.1).[64] The strong and rapid accumulation of xenon in BAT, which leads to its detection by both xenon-enhanced CT and xenon-enhanced MRI (HP Xe MRI), is of particular relevance as brown adipose tissue has recently been discovered to be metabolically active in adult humans where, as in rodents, it seems to have a primary role in the regulation of body weight and blood glucose level.[9,10,65,66]

In this chapter I will discuss some of the work I have done in this area, specifically on the detection of BAT by alternative ^{1}H –based MR techniques, which in our lab were often used in conjunction with ^{129}Xe –based MR techniques and FDG-PET for the detection of BAT. Specifically I will show how direct comparison of ^{1}H –based MR techniques with FDG-PET reveals that these techniques are not as specific to BAT as one may think.

This work has been published in the Journal of Magnetic Resonance in Medicine, McCallister et al. 2017.[21]

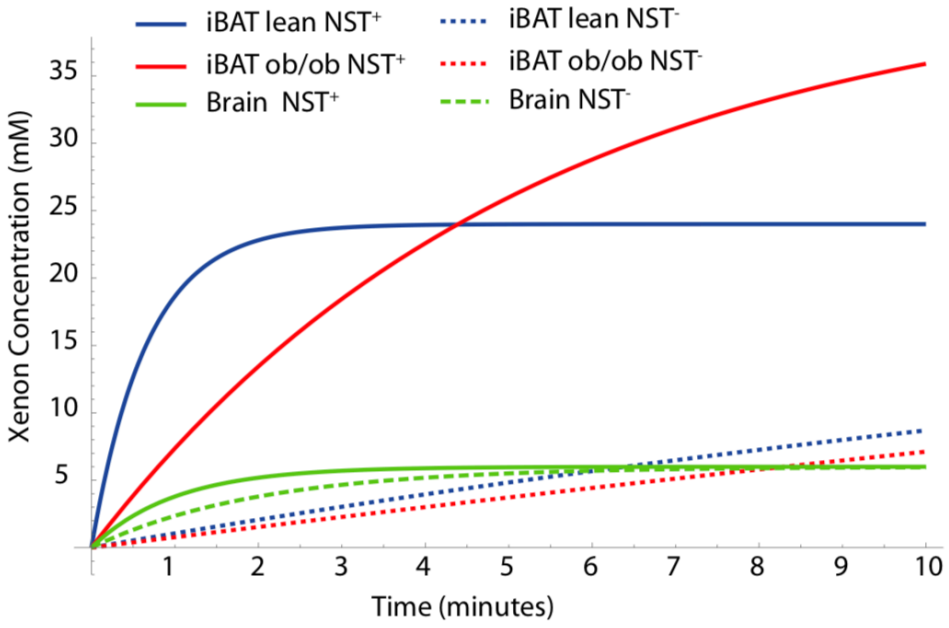

Figure 5.1 Modeling of xenon concentration in BAT and brain before (dotted) and during (solid) stimulation of non-shivering thermogenesis (NST) in lean and obese mice. Figure taken from Branca et. al. 2018.[64] Uptake was modeled using the Kety–Smith equation where inert gas absorption depends not only on the degree of tissue perfusion, but also on the solubility of xenon in the given tissue.[67] By using reported tissue blood-flow and tissue/blood partition co-efficient values for brain and BAT, xenon accumulation was modeled in both lean and obese mice in the absence and presence of NST.[68–70]

Section 5.1: Brown Adipose Tissue

Section 5.1.1: Biological Function and Relevance

In mammals, adipose tissue can be categorized into two main types: white adipose tissue (WAT) and brown adipose tissue (BAT).[9] These two tissues are structurally different and seem to have very different functions. While WAT's main function is to store energy as fat, BAT's main function is to help maintain core body temperature through a process called "non-shivering thermogenesis"(NST).[71] During non-shivering thermogenesis, this tissue can generate heat at a rate of more than 0.7 watts/g.[72] This means that 50g of this tissue can dissipate, when fully stimulated, 700 kCal/day. As such, this tissue is strongly innervated, highly vascularized, and equipped with a large number of mitochondria where fatty acids, the main substrate for heat production, are oxidized to produce heat.[73]

Thermogenesis in BAT can be stimulated by both cold (cold-induced non-shivering thermogenesis) and high fat diet (diet-induced non-shivering thermogenesis).[74,75] In rodents, the activity of this tissue is known to strongly impact energy metabolism and insulin sensitivity.[76–79] For example, healthy mice are known to develop obesity after BAT ablation[5], while transplantation and activation of BAT enables blood glucose regulation without insulin in animals models of type 1 diabetes.[80] Because of this, BAT has become the subject of considerable research and it is now considered a possible new target for anti-obesity and anti-diabetes therapies in humans.[5,8,80,81] However, whether or not this tissue plays the exact same role in humans as it does in rodents is still an open question.[7,82]

Section 5.1.2: ^{18}FDG-PET Imaging of BAT

One of the largest barriers to our understanding of human BAT's physiology and significance is the detection of this tissue.[82] The technique most commonly used to detect BAT in humans is ^{18}F-fludeoxyglucose positron emission tomography (FDG-PET) combined with computed tomography (CT). When active, because of its relatively high metabolic rate, BAT can be distinguished from surrounding tissues by an increased FDG uptake, while CT offers corresponding anatomical information.[10,81] However, while the general consensus is that an increase in FDG uptake can mark metabolically active BAT in the supraclavicular depot, it is not necessarily a biomarker for BAT thermogenesis.[11] Indeed, glucose uptake can vary greatly among individuals since endogenous glucose may compete with the injected FDG tracer.[6] Also, FDG uptake can be increased in BAT by insulin, without a corresponding increase in thermogenic activity.[83] Finally, since FDG-PET and CT both expose the subject to ionizing radiation, longitudinal studies of BAT by FDG-PET/CT are hard to justify in infants, children, and healthy adults.

Section 5.1.3: HP ^{129}Xe MR Imaging and Thermometry of BAT

Our group has shown that hyperpolarized xenon offers a radiation free alternative to FDG-PET for the detection of BAT. The lipophilic nature of xenon and the strong increase in blood flow to BAT that occurs during stimulation of thermogenic activity allows for the detection of this highly-vascularized tissue via both HP-Xe MRI and xenon-enhanced CT.[84] Dissolved-phase hyperpolarized xenon not only allows for BAT detection but also provides metabolic information. Our group has indeed shown that the lipid-dissolved xenon frequency has a very strong temperature dependence (-0.2 ppm/°C)[85]. This temperature dependence, by being 20-fold higher

than the temperature dependence of the water 1H chemical shift often used for MR thermometry, enables more accurate tissue temperature measurements by MRI. In addition our group has shown that, by referencing the temperature-dependent chemical shift of lipid-dissolved xenon to the temperature-independent chemical shift of fat protons, one can obtain absolute temperature information.[12,86] By using this method developed in our lab, we have been able to detect BAT and track its thermogenic activity in both healthy and obese adult humans by HP 129Xe MRI. While these studies represent the first direct detection of BAT thermogenesis in humans, measurements of BAT mass by HP 129Xe MRI still remain an unmet need. Measurement of BAT mass requires the acquisition of HP 129Xe images with high spatial resolution. As described in Chapter 2, the ability to acquire images with high spatial resolution strongly depends on the available SNR, which in the case of dissolved-phase xenon MRI is quite low.

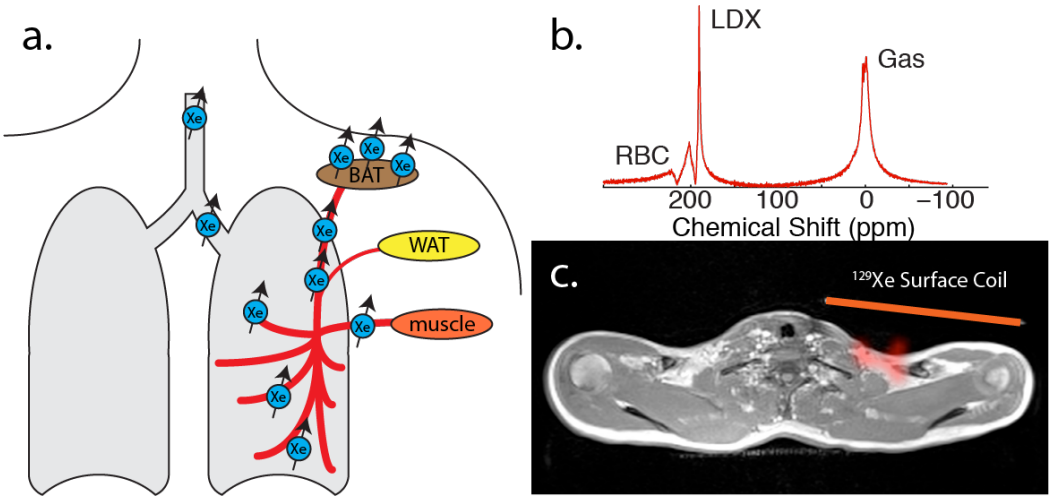

Figure 5.2 a. Illustration of Xenon accumulation in BAT due to high perfusion to this tissue and high solubility of xenon in fat. b. HP ^{129}Xe spectra obtained with a surface coil in a healthy adult human exposed to cold temperatures. A broad peak corresponding to xenon dissolved in red blood cells (RBC) is shown at the highest frequency. The peak corresponding to xenon –dissolved in lipids (LDX) is one of the narrowest peaks, enabling accurate measurements of its frequency, from which temperature is calculated. The gas-phase peak (Gas) originating from the apex of the lungs is shown at the lowest frequency. c. An axial slice through the supraclavicular area showing the positioning of the ^{129}Xe surface coil and a GRE image of the dissolved xenon in BAT.

Section 5.1.4: ^{1}H-Based MR Techniques for BAT Detection

A high-resolution ^{1}H-based MR alternative for quantifying BAT volumes has been proposed; MR fat-fraction maps of tissue lipid content. They may be able to differentiate the hydrated BAT from less hydrated WAT and, possibly, even track lipid consumption in BAT during stimulation of thermogenic activity.[87] Such MR fat fraction maps, for example, have been shown to reliably detect BAT not only in rodents but also in infants and young children.[13,88] This is not surprising, as similarly to mice that are constantly under thermal stress, infants and young children are incapable of shivering and need to rely on BAT thermogenesis to maintain core body temperature. Owing to chronic activity, BAT fat fraction is considerably lower than WAT fat fraction and, more importantly, BAT is homogenous and concentrated in well known, specific areas.[89] In adult humans, although the tissue is still confined to specific areas, is no longer homogenous. Histology shows that, in adult humans,' BAT is sparse (infiltrated with normal WAT), and highly heterogeneous at the microscopic scale.[90,91] Differences in R2* between BAT and WAT have also been reported and proposed to increase the specificity of fat fraction measurements to BAT.[14] However, given the heterogeneity and scattered nature of human BAT, and the limited spatial resolution achievable with MRI (~1 mm^3) differences between BAT positive regions and BAT negative regions that are easy to see in rodents may not be observed in humans.

Section 5.2: Water-Fat ^{1}H MRI

The nuclear spins of the ^{1}H atom in water and fat molecules are the main source of signal in magnetic resonance imaging experiments. In a typical MRI experiment, unless specific suppression techniques are employed, both spins contribute to the observed signal. Water-fat ^{1}H MRI techniques are often employed to separate these two contributions. This is done by leveraging

the difference in chemical shift between these two spin species. As such, these techniques often go by the name of chemical-shift encoded techniques (CSE).

The average chemical shift separation between the water peak and the methylene peak (the major lipid peak of fat molecules originating from ^1H atoms in the CH_2 group) is ~3.5 ppm. At 3T this leads to a frequency separation of about 420 Hz. Fat quantification techniques take advantage of this frequency difference to separate the contribution to the signal of water spins from that of fat spins. This is done by collecting the signal at different echo-times (TEs), during which water and fat spins acquire a different relative phase because of their different precession frequency. Images acquired at different echo times will inherently have different signal intensities. The highest signal intensity will be obtained for those echo times in which the two spins are in phase, and the smallest signal intensity will be obtained for those echo times in which the two spins are in opposite phase (180°). By knowing the relative precession frequency of the two spins and the TEs at which each image is acquired, one can then separate the two contributions to the signal and reconstruct separate maps of fat and water signals.

Section 5.2.1: Two-Point Dixon

The first to propose a frequency-based method to separate water and fat contribution to the MR signal was Dixon.[92,93] The basic idea was to acquire two images at two different echo times" one in which the two spins were "in-phase"($S(in)$), and one in whihc the two spins were "out-of-phase"($S(out)$), i.e. had acquired a phase shift of π. By adding and subtracting the intensity of the images, one can then obtain a selective water image $S(W)$, and fat image $S(F)$.

$$S(in) = S(W) + S(F) \text{ and } S(out) = S(W) - S(F) \quad (5.1)$$

$$S(W) = S(in) + S(out) \text{ and } S(F) = S(in) - S(out) \quad (5.2)$$

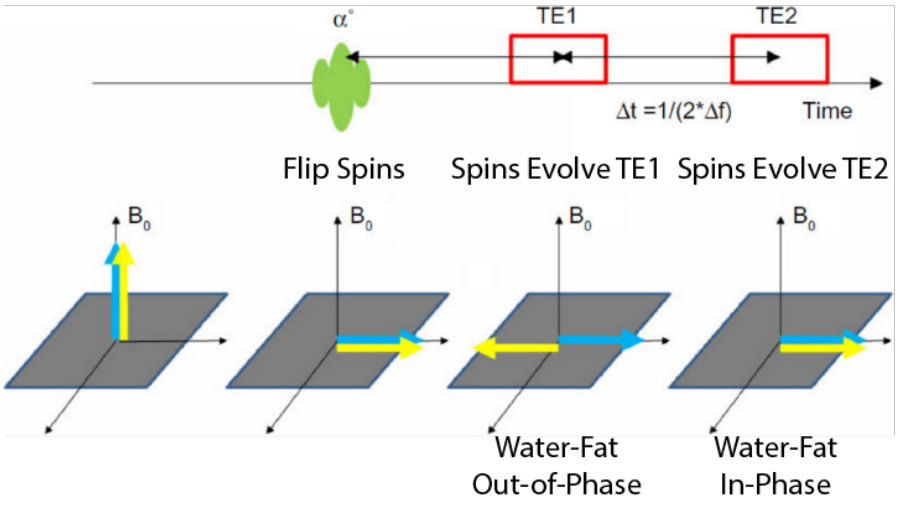

Figure 5.3 Pictorial representation of the two-point Dixon sequence, where blue represents the magnetization of water spins and yellow represents the magnetization of fat spins.

The two-point Dixon method works well to obtain a qualitative distribution of fat spins. This is because this method makes a number of assumptions that are not necessarily true. For one, that the main magnetic field B_o is homogenous. Although in magnetic resonance imaging experiments shimming is always preformed to make the magnetic field as homogenous as possible, there is still significant B_o inhomogeneity, especially in large magnetic fields such as those used for human imaging. The second assumption is that there are only two types of spins that contribute to the MR signal: water and methylene spins, and that these only acquire a relative phase shift with respect to each other. In reality the water and fat spins are not just dephasing relative to each other, but also among themselves. Because of significant macro- and microscopic field inhomogeneities, the spins experience significant T_2^* decay. This decay causes the magnetization vector of water and fat spins not only to move in and out of phase, but also to decrease in magnitude at a tissue-dependent rate. In addition, water and methylene spins are not the only spins that contribute to the detected signal. The fat signal contains several spin components, not just the CH_2 (methylene)

group (Figure 2.5). Therefore, by assuming that only water and methylene spins contribute to the detected signal, and ignoring transverse relaxation of these spins, can lead to relatively large errors in fat quantification (>10%).

Section 5.2.2: Multi-Echo Methods

In order to address these issues, Reeder et al.[25] developed a method called the "Iterative Decomposition of water and fat with Echo Asymmetry and Least-squares estimation", or IDEAL, where fat and water signals are fit based on a maximum likelihood of the signal. Multiple images, often six or more, are taken at different echo times to account for the different contributions to the MR signal as well as for the transverse relaxation. Current multi-echo CSE methods account for T2*, macroscopic field inhomogeneities, and the multiple peaks of the fat spectra.[26,94] The signal model used to fit the acquired data is then:

$$S_n = (M_w + C_n M_f) e^{-R_2^* TE_n} e^{j(2\pi\gamma TE_n)} \quad (5.3),$$

where M_w and M_f are the respective magnitudes of the water and fat signals, R_2^* is the signal decay ($1/T_2^*$) caused by dephasing from any intra-voxel microscopic inhomogeneities as well as motion, TE_n are the echo times at which the images are acquired and for which the spins were allowed to evolve, and γ is the frequency difference caused by inter-voxel macroscopic field inhomogeneities. C_n is a known complex coefficient describing the contribution to the fat signal from p fat components:

$$C_n = \sum_{i=1}^{p} w_i e^{j(2\pi\Delta f_i TE_n)} \quad (5.4)$$

Six, seven, and nine-peak fat spectral models are most commonly used in CSE reconstruction protocols, with no specific choice having currently been proven to be superior to the rest, but

showing significant improvement over single peak fat spectral model.[95] In these experiments, the intensity and frequency separation between the different lipid protons and the relative separation between water and lipid protons is either set using spectra from previous studies, or calibrated in a pre-scan protocol.[95–98]

If the magnitude of the signal is fit, contributions from the external macroscopic field inhomogeneities are removed and the signal can be easily modeled and fit.[25] Fitting the complex signal is a bit more complicated because the effect of macroscopic B_o-field inhomogeneities and eddy-currents must be taken into account.[94,99] Yu *et al.* 2011 showed that magnitude based fitting had much lower errors in quantification at high and low fat fractions while complex based fittings had slightly lower errors immediately around FFs of 50%.[26] To account for this they proposed a protocol that employs a combination of both methods. Specifically, applying a Fermi weighting function to the resultant magnitude and complex-fit FF maps leads to better complex fittings and the resolution of phase-errors at high and low FFs.[26]

Section 5.3: Implementation and Acquisition of Protocol on the Hybrid PET/MRI scanner

The scope of this work was to assess: 1) the spatial correlation, within the supraclavicular fat depot, between BAT maps, as obtained by MR fat fraction measurements alone (BAT_{MRI}) and those obtained by combined fat fraction measurements and FDG uptake measurements ($BAT_{PET/MRI}$); 2) whether differences exist in tissue fat fraction and R2* between BAT_{MRI} areas that are glucose avid and those that are not glucose avid; 3) the feasibility of monitoring changes in human BAT fat fraction during stimulation of thermogenesis by MRI.

To meet these aims we designed a joint ^{18}FDG-PET fat fraction MRI study, which was then performed in 16 healthy subjects, whose characteristics are described in Table 5.1. The hybrid

PET/MR system (a Biograph mMR scanner from Siemens Healthcare, Germany) recently installed at the Biomedical Research Imaging Center at UNC, was one of the first in the country and gave us an unique advantage for performing these studies, where ^{18}FDG-PET and fat fraction MRI measurement were directly compared on the same subject, thus almost completely eliminating co-registration errors caused by subject motion and/or repositioning. Images were acquired using a personalized cooling protocol to maximize BAT thermogenic activity.[100] The study was approved by the Institutional Review Board of the University of North Carolina at Chapel Hill and was conducted in compliance with the Helsinki Declaration. All subjects gave written, informed consent.

Subject	**A**	**B**	**C**	**D**	**E**	**F**	**G**	**H**	**I**	**J**	**K**	**L**	**M**	**N**	**O**	**P**
Sex	M	M	F	M	M	M	F	F	M	M	F	F	M	F	M	F
Age	24	30	30	53	25	20	25	27	23	22	24	23	21	38	43	49
BMI	25.9	27.1	19.3	27.8	24.0	24.5	20.6	23.8	24.5	22.1	24.2	21.0	23.3	29.6	36.6	34.4

Table 5.1. Subjects' demographics displaying sex, age, and BMI.

In seven of the sixteen subjects, changes in fat fraction were additionally investigated. For these scans, the subjects were not cooled and then transferred into the scanner, instead a similar personalized warming/cooling/warming procedure was performed inside the PET/MR scanner to minimize motion and repositioning artifacts. Then MR fat fraction measurements were performed both at thermoneutrality (water temperature set at 30°C for 40-50 minutes) and every 30-45 minutes during cold exposure, which lasted for 1 hour before and 1.5 hour after the injection of the radiotracer. Additional MR fat fraction measurements were performed during and after PET image acquisition, when the subject was brought back to thermoneutrality.

Section 5.3.1: Phantom Preparation

A combination of three different fat fraction MR methods were used to establish any dependence of BAT delineation on the specific MR method used. A phantom study was performed to compare the results of the different reconstruction methods. Specifically, six different emulsions, 0%, 20%, 40%, 60%, 80%, and 100% oil, were created using different concentrations of corn oil in water. Stable homogenous emulsions of corn oil and distilled water were first prepared following the same procedure described in Bernard *et al.* 2008.[101] Specifically, 15 mmol of sodium dodecyl sulfate (Sigma-Aldrich, St. Louis, MO) and 5 g of carrageenan were added to a liter of deionized and demineralized water, which was then stirred by using a magnetic hotplate and heated to 50°C. The emulsions were homogenized, checked for absence of microbubbles and creaming, and imaged using the same fat fraction MR protocols used for human imaging. Images were then analyzed similarly to human fat fraction images. All phantoms were allowed to equilibrate next to the PET/MR magnet bore for at least hour prior to scanning in order to allow all phantoms to reach the same equilibrium temperature and to avoid any possible additional frequency shift of the temperature dependent water frequency.

Section 5.3.2: Imaging Protocols

The MR images were acquired to cover the entire region from the neck to the apex of the lungs. A 3D dual echo Dixon sequence and a T2*-corrected six-echo Dixon sequence, with single and multi-frequency fat signal modeling, respectively, were used to acquire fat-fraction maps of the supraclavicular region in 9 subjects. The dual echo Dixon sequence was also used in an additional 7 subjects to acquire fat-fraction maps and glucose uptake maps during stimulation of thermogenic activity, which was performed entirely inside the PET/MRI scanner. Fat-fraction maps using both

protocols were also acquired on samples of varying fat content to compare the accuracy of the two protocols for the quantification of fat content.

A magnitude based fitting protocol employing a Levenberg-Marquardt non-linear fitting algorithm was then used within the Siemens' Image Calculation Environment (ICE) program to fit the magnitude of the complex signal of the multi-echo data to the signal model,[94] which is the magnitude of Eqn. 5.3 and 5.4.

$$|S_n| = \left|(M_W + c_n M_F)e^{-TE_n R2^*_{eff}}\right| \quad (5.5)$$

Where $R2^*_{eff}$ is an effective R2* for both water and fat spins and c_n is a complex fat dephasing function based on a six-peak human fat spectral model. The spectral model is the same used previously in human BAT differentiation by Hu et al. 2013,[19] with the following chemical shifts and relative resonance areas: 0.90 ppm, 125.8; 1.30 ppm, 956.4; 1.59 ppm, 109.1; 2.03ppm, 146.0; 2.25 ppm, 100; 2.77ppm, 23.4; 5.31 ppm, 63.9.[102]

This fitting scheme was compared in three participants to the combined magnitude and complex fitting protocol described in Yu et al. 2011. A complex fitting protocol was used within the Siemens' Image Calculation Environment (ICE) program to fit the complex signal model with relaxation rate R(x), field map w(x), background phase P(x), eddy current phase O(x), and readout polarity $a = \pm 1$.[99]

$$S_n(x) = \big(W(x) + c_n F(x)\big)e^{-R(x)TE_n + iw(x)TE_n + aO(x) + iP(x)} \quad (5.6)$$

Positron emission tomography scanning was performed in the 3-dimensional mode with 6 minutes per bed position and a total of 3-4 bed positions to cover an area from the skull to the

kidney. Resolution was 4.1mm x 2.6mm x 3.1mm. Standard uptake values (SUVs) were calculated from the measured radio activity r, decay corrected injected dose a', and subjects' body weight w.[39]

$$SUV = \frac{r}{a'/w} \quad (5.7)$$

Section 5.3.3: Image Analysis

All MRI and PET images were analyzed, after reconstruction by the Siemens ICE program, using MIM software (MIM Software Inc. Cleveland, OH). In the 7 subjects cooled inside the scanner, intensity-based deformation software was applied to each water component of the two-echo Dixon image to correct for unavoidable subject motion during the extended imaging time (~3 hours). Their corresponding fat component images were then transformed using the same transformation matrices. From the deformed water component images (W) and co-deformed fat component images (F), fat fraction (FF) images were then created where *FF=F/(F+W)* for FF≥50% and FF=1-W/(F+W) for FF<50%.

In the 9 subjects in which single two-echo and six-echo Dixon FF maps were acquired simultaneously with PET images, the deformation algorithm was not needed and was not applied. The two-echo FF images were again created from the fat and water component images while the reconstruction of the six-echo Dixon automatically provided FF, water-fraction, and R2* maps.

In all MRI imaging data sets, regions of interest (ROIs) were defined using the following steps: 1) A ROI was first drawn around the supraclavicular region excluding background, bone, muscle, major blood vessels and skin. 2) A FF range between 40% and 100% was used to define, within

this region, regions containing BAT (BAT_{MRI}). (Figure 5.4). 3) An additional constraint of SUV > 1.5 was applied to define regions of BAT constrained by both FF values and SUV values ($BAT_{PET/MRI}$). 4) The ratio between (BAT_{MRI} -$BAT_{PET/MRI}$)/ BAT_{MRI} was then used to calculate the percent disagreement of BAT volume constrained by FF values alone (BAT_{MRI}), versus BAT volume constrained by both FF and SUV values ($BAT_{PET/MRI}$). Finally, FF values and R2* values in $BAT_{PET/MRI}$ regions were compared to those in BAT_{MRI} excluded from $BAT_{PET/MRI}$.

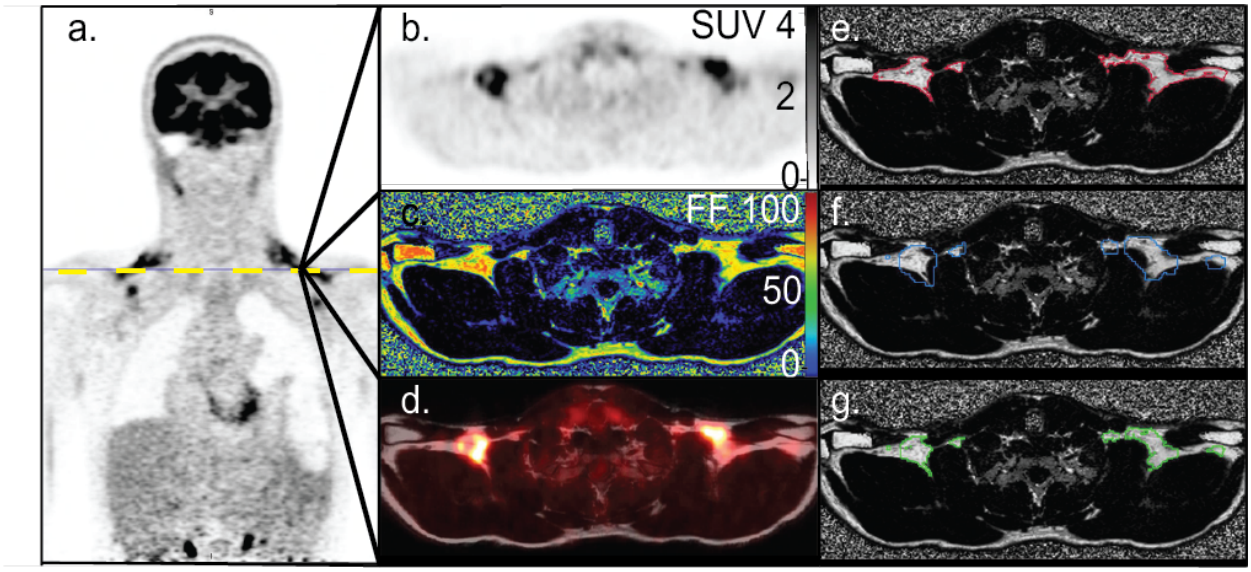

Figure 5.4 Identification of supraclavicular BAT depot using FF values and FDG uptake values in subject I. a. Coronal FDG-PET image showing intense glucose uptake in supraclavicular region. b. Axial FDG-PET image, across the dotted yellow line. c. Corresponding axial FF image. d. FDG-PET image fused with the corresponding MR fat image, illustrating FDG-PET uptake in the supraclavicular fat depot. e. FF map and a contour identifying supraclavicular fat depots with a FF greater than 40% (red) f. Contour of tissue with a SUV > 1.5 (blue) over a FF image. g. BAT volume identified by using a FF > 40% and an SUV value > 1.5 (green).

In order to examine further, pixel by pixel, any possible correlation between SUV values, FF values, and R2* values within BAT_{MRI} regions, PET and MR images were also exported to MATLAB (Mathworks, Natick, MA), where PET images were resampled to the MR resolution using linear interpolation, and a linear regression was run on the resultant pixel-by-pixel data.

A comparison of the two-echo and six-echo protocol was also performed in the nine subjects in whom fat-fraction maps were acquired using FF protocols as well as for the phantom studies. For this comparison, a ROI was drawn around the supraclavicular region excluding background, bone and skin. Thresholds were applied on the six-echo Dixon images to define regions with a FF range between 0%-10%, 10%-20%, 20%-30% and so on, up to 100%. These contours were applied directly to the corresponding two-echo Dixon FF maps. For each region and for each subject, mean FF value obtained with the six–echo Dixon protocol was compared to mean FF value obtained with the two–echo Dixon protocol. A second order binomial trend line was used to fit the relation between FF values obtained from the two protocols for each region and from each subject. The resultant expression was then used to correct FF values obtained with the two-echo Dixon protocol in the 7 subjects that underwent cooling inside the magnet and in which BAT FF changes were assessed during stimulation of thermogenic activity using the two-echo Dixon protocol alone. This correction, however, does not completely correct for all FF biases; the correction factor is unable to account for difference in R2*.

For the phantom images, the same ROI was drawn on the two FF maps acquired with the two fat-fraction protocols. Bland–Altman plots were then constructed by plotting the difference in FF values obtained with the two methods against the true FF value and against the six-echo FF value, which, in this case, was considered as a reasonable gold standard.

Section 5.4: Results

Section 5.4.1: Comparison of Two-Echo and Six-Echo MR Methods

In the supraclavicular region, the two-echo Dixon protocol, relative to the six-echo Dixon protocol, appears to overestimate FF at low FF values (<60%) and underestimates FF at high FF

values (>60%) as shown in Figure 5.5.a. The relation between FF values as estimated by the two-echo Dixon protocol and FF values estimated by the six-echo Dixon protocol is consistent across all subjects and, while non-linear, can be well approximated by a second order polynomial function (linear regression analysis with R^2=0.96). In Figure 5.5.b, the phantom results display the same trend between the two protocols and shows, as expected, that the six-echo Dixon protocol more accurately measures fat fraction than the two-echo Dixon protocol. Figure 5.5.c shows the Bland–Altman plots for the in-vivo and in-vitro data relative to the six-echo Dixon. A large over-estimation of FF values by the two-echo Dixon protocol relative to the six-echo Dixon protocol is seen for fat fractions less than 60%. Between 60% and 80%, as measured by the six-echo Dixon, the difference in FF values between the two protocols decreases to zero. For FF values greater than 80%, the two-echo Dixon protocol underestimates FF value when compared to the six-echo Dixon protocol. When looking at the magnitude of the change in FF, for FF values less than 40%, the two-echo Dixon protocol underestimates the change in FF with respect to the six-echo Dixon protocol by only 4%. However, for fat fraction values between 50% and 85%, changes in FF values are underestimated by as much as 66%. Figure 5.5.d shows the Bland–Altman plots for the in-vitro data relative to the true FF, which reveal a mean difference from the true fat fraction equal to -2.1% for the six-echo, and equal to 6.3% for the two-echo protocol. Maximum differences were 8% (six-echo) and 20.1% (two-echo). Of note, there was a general underestimation for both protocols at high fat fraction values (> 80%). Excluding the values from fat phantoms greater than 80% FF, the mean differences were equal to -1.2% (two-echo), 13.3% (six-echo) and 14.5% (between the six-echo and two-echo).

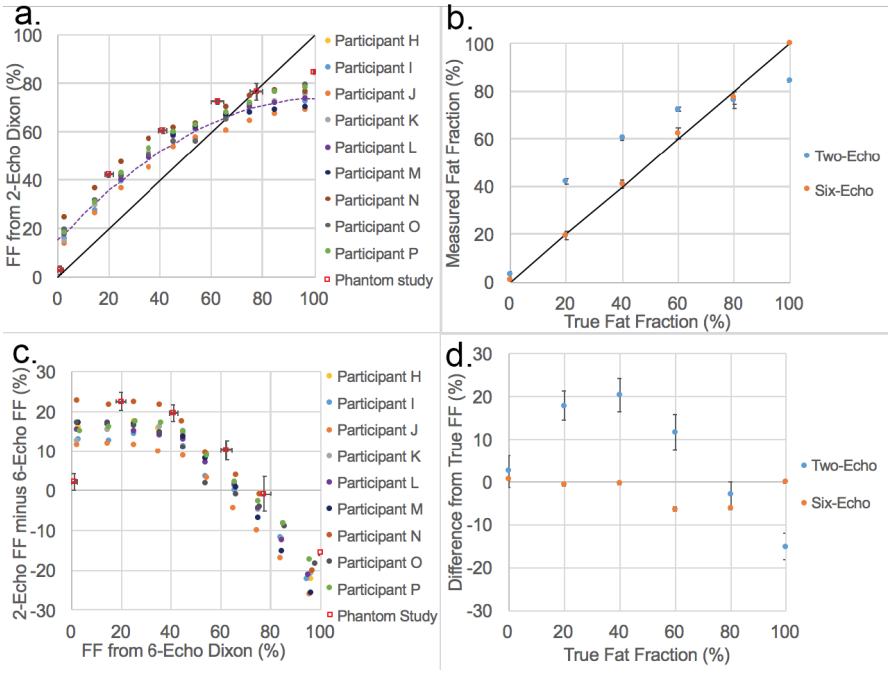

Figure 5.5 a. Comparison of FF values obtained from phantoms and from the supraclavicular region of 9 subjects by using the two-echo and the six-echo Dixon protocol. The fit of the in-vivo data is a second order polynomial $y = -0.0054x^2+1.1248x+15.436$ with $R^2=0.96$ b. Plot of percentage fat fraction (by volume) for each of the 6 water-fat phantoms against FF value as measured by two-echo and six-echo Dixon protocol. c. Bland–Altman plot of the FF difference between the two-echo and six-echo Dixon protocol relative to the FF measured by the six-echo Dixon protocol for both the 9 subjects and the in vitro phantom study. d. Bland–Altman plot of the in vitro phantom study showing the FF difference between the measured FF maps for both the two-echo and six-echo Dixon protocols and the FF as measured by volume.

Section 5.4.2: Comparison of Magnitude and Magnitude/Complex Reconstruction

In 5 subjects (L, M, N, O, and P) FF maps were obtained by using the magnitude-based water-fat separation algorithm as well as by using a combined magnitude-based and complex-based water-fat separation algorithm, as described in Yu *et al.* 2011, to assess difference in fat fraction quantification between these two methods.[26] Both methods are described in Section 5.3.2. As is shown in Figure 5.6, FF values obtained with the two reconstruction algorithms are the same in the supraclavicular fat region, identified as BAT_{MRI} (FF > 40), in all 5 subjects analyzed. On the

other hand, differences were found in regions with a FF of about 30%, mainly at boundaries between different tissues and at boundaries between tissue and blood vessels.

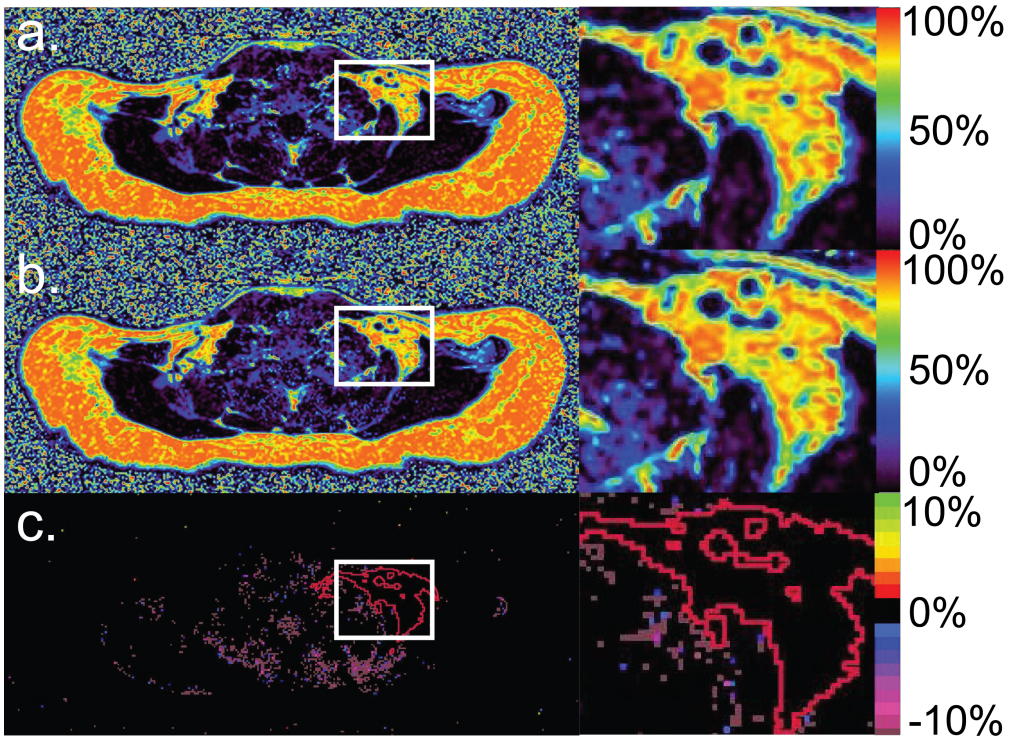

Figure 5.6 Example of FF maps obtained with different FF separation algorithms for an axial slice encompassing the supraclavicular fat depot from subject P. a. FF map obtained by using the magnitude-based algorithm b. FF map obtained by using the combined magnitude-based and complex-based separation algorithm. c. Difference map. Right side shows the supraclavicular fat depot with the region corresponding to BAT_{MRI} (FF>40%) outlined in red. No differences in FF were observed within the supraclavicular fat depot.

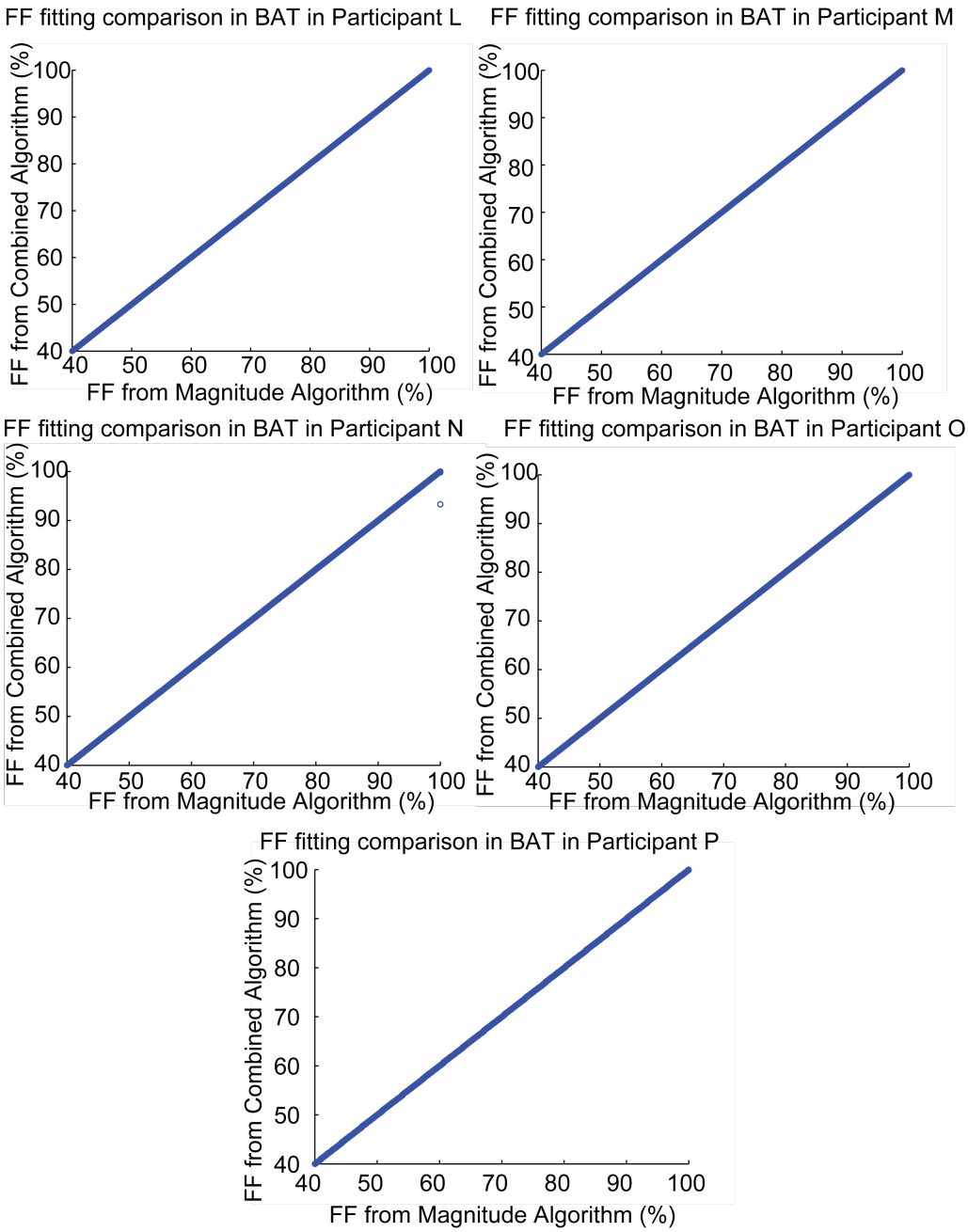

Figure 5.7 Plots showing FF values obtained with the two different algorithms for each voxel within the supraclavicular fat depot identified as BATMRI (FF>40%). For all 5 subjects, the same FF values were obtained by using the two algorithms (linear trend with a R^2=1, slope=1, and y int.=0).

Despite the combination of complex-based and magnitude-based separation methods having been shown to be more accurate than magnitude-based separation methods for FF quantification

in general,[26] in the regions of the supraclavicular depot identified as BAT_{MRI} (FF>40%) the two methods gave the same FF values.

Section 5.4.3: Comparison of FDG-PET and MRI BAT Maps

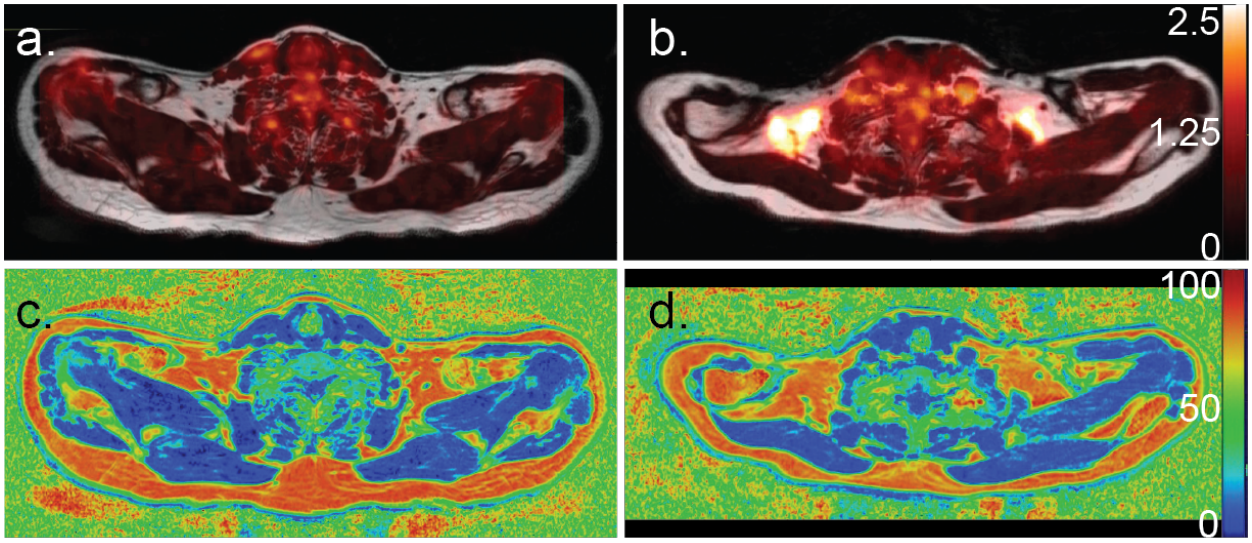

Figure 5.8 a. Axial FDG-PET image overlaid on a fat component Dixon image of subject D, which resulted BAT-negative in the FDG-PET scan. Very little FDG uptake is seen in the supraclavicular fat depot. b. Axial FDG-PET image of subject C, which resulted BAT-positive in FDG-PET scan, overlaid onto the corresponding fat image. c. Corresponding MR FF map of the same region of subject D. d. Corresponding MR FF map of the same region of subject C.

Of all of the subjects, only subjects D and O, a 53 y.o. male with a BMI of 27.8, and a 36 y.o. male with a BMI of 36.6, produced BAT-negative results according to FDG-PET scans. Figure 5.8 shows representative PET-MRI fusion images and FF maps of a BAT-negative (subject D) and a BAT-positive (subject C) subject. Despite their supraclavicular fat depot presenting similar FF values, one (subject D) results BAT negative and the other (subject C) results BAT positive. Moreover, in the BAT positive subject, despite the entire supraclavicular fat depot displaying a FF above 40%, only about 50% of the region has an SUV of greater than 1.5. In fact, in all subjects, BAT_{MRI} volume was larger than $BAT_{PET/MRI}$ volume. Figure 5.9 plots the percent disagreement in

BAT_{MRI} volume compared to $BAT_{PET/MRI}$ volume as a function of the Maximum Standardized Uptake Value (SUV_{max}) found in the supraclavicular fat pad for all FDG positive subjects. A strong inverse correlation (R^2= 94% and p<0.00001) was found between the degree of disagreement and SUV_{max}, meaning that disagreement was much smaller (~2%) in subjects in which BAT activity was particularly strong.

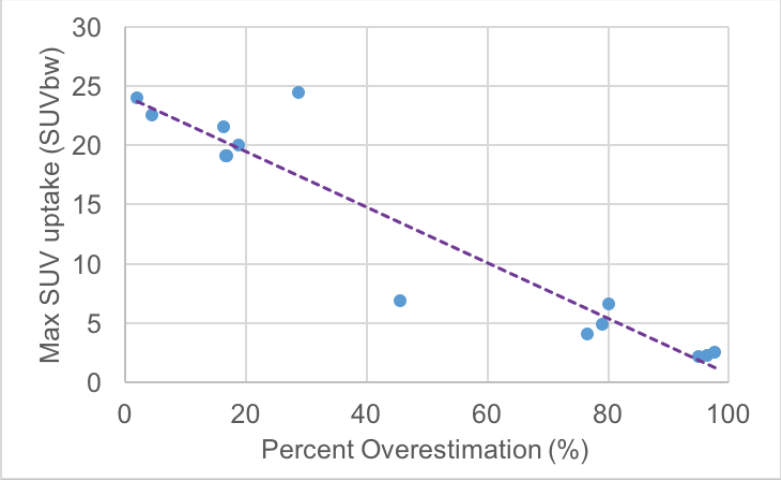

Figure 5.9 Scatter plot of max SUV versus BAT_{MRI} percent difference with respect to $BAT_{PET/MRI}$ for all BAT-positive subjects showing a linear fit y=-0.235x+24.16 with a Pearson correlation coefficient of r = -0.951 and p < 0.0001.

This disagreement between BAT_{MRI} volume and BAT_{PETMRI} volume leads to the question: "is the fat fraction different between the FDG(+) and FDG(-) BAT_{MRI} regions?". As Figure 5.10 shows, no significant difference in FF was found between FDG(+) and FDG(-) BAT_{MRI} regions, independent of the FF protocol used. We did the same analysis for R2* maps and got similar results shown in Figure 5.11. Again, a slight difference in the R2* average was seen only in lean subjects but it was insignificant and was not in all subjects. Differences in R2* were observed within individual subjects but opposite trends were observed across subjects.

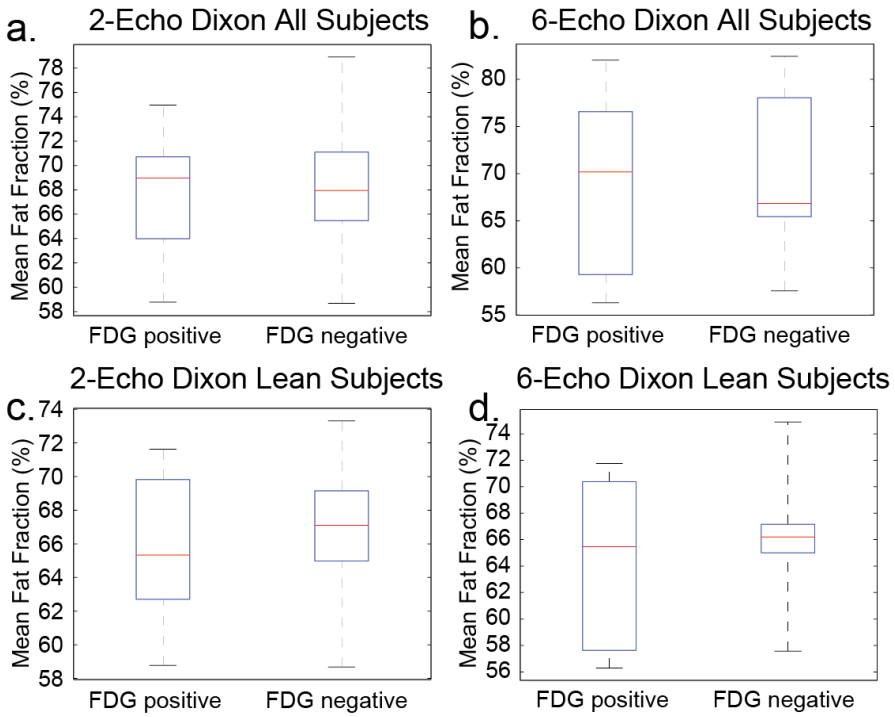

Figure 5.10 Box plot of the mean FF in FDG(+) and FDG(-) regions a. Mean FF values in BAT_{MRI}, as measured by the two-echo Dixon protocol, in all BAT+ subjects: Mean FF: FDG(+) 68±5%, FDG(-) 67±5%, p=0.6429. b. Mean FF values in BAT_{MRI}, as measured by the six-echo Dixon protocol, in all BAT+ subjects: FDG(+) 70±9%, FDG(-) 69±11%, p=0.7873 c. Mean FF values in BAT_{MRI}, as measured by the two-echo Dixon protocol, in all lean (BMI<26), BAT+ subjects: Mean FF: FDG(+) 67±4%, FDG(-) 66±5%, p=0.6383. d. Mean FF values in BAT_{MRI}, as measured by the six-echo Dixon protocol, in all lean (BMI<26), BAT+ subjects: Mean FF: FDG(+) 66±6%, FDG(-) 64±7%, p=0.6557.

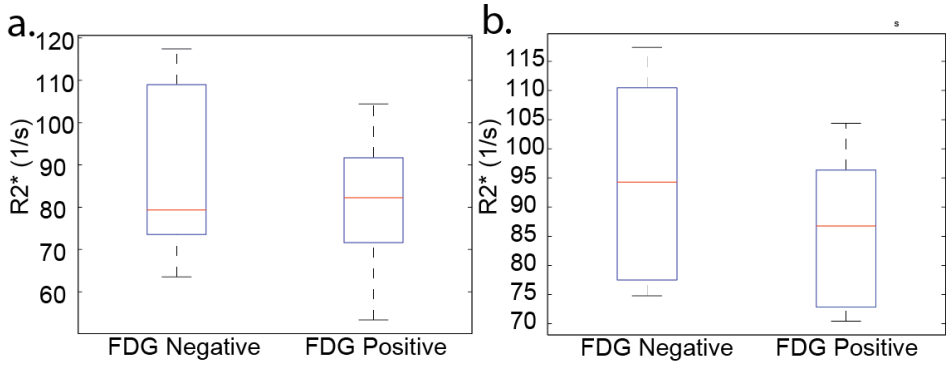

Figure 5.11 Box plot of the mean R2* as measured by the six-echo Dixon in FDG(+) and FDG(-) regions a. In all subjects mean R2* was: FDG(+) 81±60 s^{-1}, FDG(-) 83±63 s^{-1}, p=0.9297. b. In all lean subjects mean R2* was: FDG(+) 86±56 s^{-1}, FDG(-) 95±65 s^{-1}, p=0.7315

To further investigate the relationship between FDG uptake and fat fraction and R2* independent of the threshold chosen to demark FDG(+) tissue, we looked at correlation plots of FDG uptake and FF as well as R2* in every voxel as shown in two representative subjects in Figure 5.12. No clear, general trend was observed between FF and glucose uptake in the subjects analyzed. We anecdotally did observe some areas of very high FDG uptake (SUV>5) appearing to display lower fat fractions in a couple of subjects as shown in Figure 5.13, but there was no way to predict which low FF areas would display high FDG uptake.

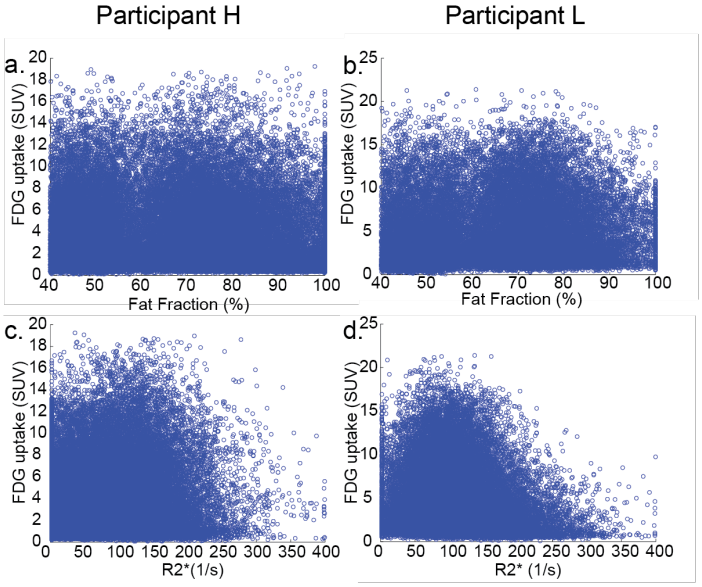

Figure 5.12 Scatter plots of the SUV vs. the FF values in each BAT_{MRI} voxel for a. Subject H and b. Subject L. When a linear regression was run R^2 was 0.0008 and 0.13 respectively. Scatter plots of the SUV vs. R2* values in each BAT_{MRI} voxel for c. Subject H and d. Subject L. When a linear regression was run R^2 values were 0.053 and 0.014 respectively. A linear regression run on both FF and R2* together allowing for interaction and quadratic terms gave an R^2 of 0.03 and 0.06 respectively.

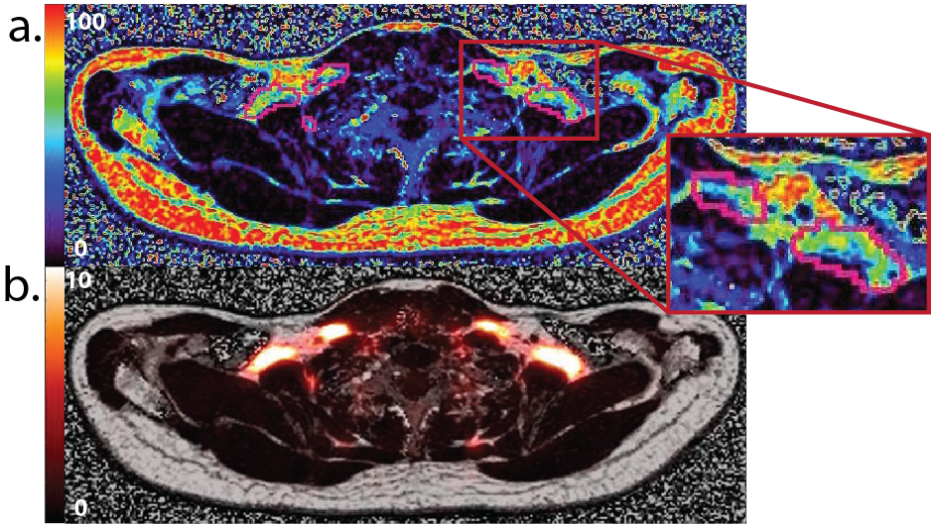

Figure 5.13 A comparison of FDG-uptake and FF in subject K. a. Axial image showing SUV in supraclavicular area b. Axial image showing FF values obtained with the six-echo Dixon protocol. Marked ROI contours regions of very-high uptake with SUV greater than 5.

If FF and R2* are not correlated with FDG uptake, there is still the idea that perhaps we can identify BAT by looking for a decrease in FF over time. Of the seven subjects cooled inside the magnet, six of them resulted BAT-positive according to FDG-PET scans. Of these, half of them (subjects A, E, and F) showed a decrease in BAT fat fraction during the individualized cooling protocol. Figure 5.14 a. shows this decrease in subject A with a drop of ~2% as measured by the two-echo Dixon protocol. Considering the underestimation produced by the two-echo Dixon protocol in this range, this change truly corresponds to a change of ~4%. Figure 5.14 c. shows the change in fat fraction in muscular tissue in the same subject, which, as expected, does not show a linear decrease and varies only slightly (0.5% as measured by the two-echo Dixon or ~0.1% when normalized to the six-echo Dixon protocol). Figure 5.14 b. shows the fat-fractional changes of BAT in subject B, who did not show a decrease in FF. In this subject, a fluctuation in tissue fat fraction as large as 2% was measured during cooling by the two-echo Dixon protocol. Figure 5.14

d. shows the fat fraction in muscular tissue of the same subject (subject B). With respect to subject A, muscle FF in this subject clearly shows a considerably large fluctuation, ~3%.

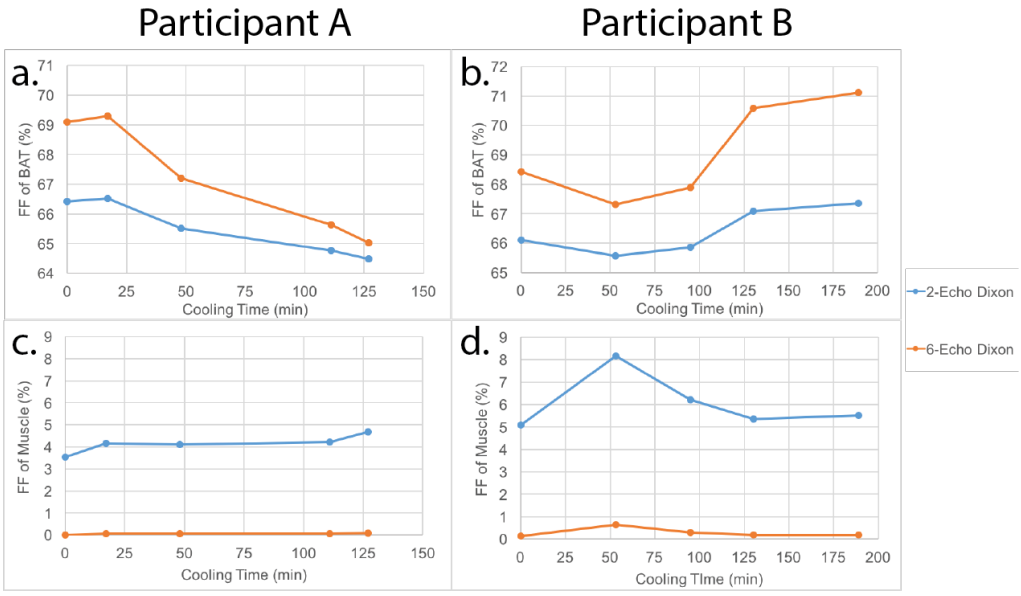

Figure 5.14 FF values during the individualized cooling protocol. a. FF values in $BAT_{PET/MRI}$ of Subject A. $BAT_{PET/MRI}$ were defined as regions with FF >40% and SUV>1.5. The data was well fit (R^2=.96) with a significant linear decrease ($p<0.0001$). b. FF values in $BAT_{PET/MRI}$ of Subject B. The data did not show a linear trend (R^2=.61). c. FF values in muscle of Subject A. d. FF values in muscle of Subject B.

Section 5.5: Discussion

The goal of this study was to analyze the performance of FF ^{1}H MRI techniques in identifying BAT regions as compared to that identified by PET/MRI measurements. In this study we found absence of a strong correlation between BAT_{MRI} and $BAT_{PET/MRI}$ in subjects with low glucose uptake. One may argue that in these subjects, areas with decreased glucose uptake correspond to areas with reduced BAT activity, not reduced BAT content. However, given what we know about the scarcity of this tissue in the supraclavicular area, especially in those subjects in which BAT has a very low activity,[103] it is unlikely that this would be the case. It is also unlikely that upon

maximal stimulation of thermogenic activity by cold exposure, some BAT is activated and takes up glucose while some does not.

A strong and significant negative correlation seems to exist between percent disagreement in BAT maps and maximum standardized uptake values. This means that the lack of correlation of BAT volume is smaller in subjects that display highly active BAT. This is not surprising considering that the subects in our study that presented the highest glucose uptake in their supraclavicular fat were young, lean subjects and are expected to have a higher percentage of BAT in their supraclavicular region. The general consensus is that this tissue, if not used, becomes infiltrated and ultimately dominated by true white adipocytes.[103,104] When this happens, the concentration of BAT cells in major BAT locations can drop dramatically.[90,91,103,104] A similar effect is known to occur in rodents in which the periphery of the interscapular BAT is often made by a mixture of brown fat cells with reduced thermogenic capacity and white adipocytes, leading to a substantial reduction in FDG uptake.[105] However, though the periphery of this mixed characteristic tissue can be easily spotted in MR FF images in rodents, in adult humans this does not seem to be the case. Areas with intense glucose uptake do not have a consistently lower FF value than areas of low glucose uptake across all subjects. This may be caused by the heterogeneity of BAT in humans, where regions containing mostly WAT and vasculature may be indistinguishable from regions containing BAT by fat fraction alone. As FDG is not the main substrate for BAT thermogenesis, it may be argued that the FDG negative fat may contain similar amounts of BAT that did not display uptake. This however seems unlikely because of our use of a personalized cooling protocol that maximally stimulates BAT and the proximity of FDG positive and FDG negative regions within the supraclavicular depot.

We also investigated the performance of the two-echo Dixon protocol versus the six-echo protocol. We found that the two-echo Dixon protocol can produce very different FF values with respect to the six-echo Dixon protocol, especially in tissues with a FF lower than 40%. Smaller errors are made in tissues with a fat fraction higher than 40%.

In other work, R2* values have been used to improve detection specificity or to directly detect BAT activation.[14,17,19] A lack of significant difference in R2* values was found in this study between FDG(+) and FDG(-) BAT_{MRI} areas. Only in lean subjects could a small difference between FDG+ and FDG- regions be detected. In view of the heterogeneity of the supraclavicular depot, the inconsistency of the results of this study with previous rodent studies is not surprising.

When looking for BAT with MR techniques in humans, most studies have examined differences in FF and R2* between the supraclavicular region and abdominal or subcutaneous WAT.[14,19,22,106] While there exist measurable differences in FF and R2* between WAT in the abdominal region and supraclavicular fat, this does not entail that there exist differences between WAT and BAT in the supraclavicular area. This could be the case if BAT were present in sufficient amounts and had a particularly low fat content, but this is known not to be the case in humans.[104,107]

Section 5.6: Conclusions

We have found that fat fraction ^{1}H MR methods cannot replace the specificity of FDG-PET for identification of BAT, especially in those BAT-positive subjects with low BAT activity. Although fat fraction and R2* measurements are not specific to BAT in all subjects, they are certainly a better alternative to CT. They are radiation free and they can be used to provide anatomical reference for PET images as well as to monitor tissue hydration and lipid consumption during stimulation of thermogenic activity. The measurement of lipid consumption does present

some challenges, though. First, a quantitative fat fraction protocol should be used when looking at changes in fat fraction in the supraclavicular region. The decrease in tissue fat fraction seen in human BAT is indeed much smaller than what is typically observed in rodents (~30%).[14,22,108] This means that an underestimation of fat fraction of a couple of percent can make a significant difference in the detection. When sensitive to such small differences, even temperature changes could be a confounding factor.[109] Second, subject's motion or repositioning can mask changes in fat fraction, especially in those subjects with low BAT activity. To this end, a quantitative fat fraction protocol, coupled with a personalized cooling procedure that maximizes BAT activity and which is performed inside the scanner (to minimize co-registration errors), should be used. This, however, considerably increases imaging cost and may be prohibitive for larger studies.

CHAPTER 6: EFFECT OF MAGNETIC SUSCEPTIBILITY ON THE ACCURACY OF MR FAT FRACTION QUANTIFICATION TECHNIQUES

As previously discussed, over the years ^{1}H –based MR fat fraction techniques have been refined to model better the detected MR signal and improve the accuracy of MR FF quantification. However, all models proposed so far have assumed a constant frequency separation between water and fat spins, despite the fact that water and fat spins are typically segregated in different tissue compartments with very different magnetic properties. In the present work, the effect of the difference in magnetic susceptibility between water and fat compartments is computed and measured experimentally, in phantoms as well as in tissues, like BAT, that are known to be very inhomogeneous at the microscopic level.

This work has been published in the Journal of Magnetic Resonance Imaging, McCallister et al. 2018.[110]

Section 6.1: Fat fraction Spectral Models

Fat-fraction quantification methods were originally proposed and developed to replace non-targeted tissue biopsy for the detection of liver steatosis in humans.[98,111] For this purpose, chemical-shift encoded acquisitions (CSE) have been developed,[95,112] where the signal from multiple echoes is acquired and then fit to a specific water-fat spectral model. To reduce errors in FF quantification, the acquisition and the signal model have evolved over time to include the effect of different transverse relaxation times (T2*) between water and fat spins, as well as the effect of macroscopic field inhomogeneities.[26,94] Also, 6,7, or 9-peak fat spectral models have been

proposed and used to reconstruct the MR signal.[95] In these experiments, the relative intensity and frequency separation between the different lipid protons and the relative separation between water and lipid protons is either set using spectra from previous studies, or calibrated during a pre-scan.[95–98]

Although the frequency separation between the different lipid protons is expected not to vary notably, the water-fat frequency separation is expected to be very sensitive to a number of factors such as temperature and magnetic susceptibility gradients.[113] The effect of temperature, which is known to reduce the water-fat separation by 0.01ppm/°C, on CSE fat quantification protocols was recently investigated by Hernando et al.[109] Authors showed that even a temperature variation of 10°C, which produces a water-fat frequency shift of just 0.1ppm, could lead to large FF quantification errors, on the order of 5% or higher. To this end, the scope of this work was to analyze how the accuracy of FF MR techniques in supraclavicular fat is affected by microscopic susceptibility gradients present at the microscopic level and that are also expected to change the water-fat frequency separation by a few tenths of a ppm.

Section 6.2: A New Model to Account for Susceptibility-Induced Frequency Shifts

While macroscopic magnetic field gradients produce a frequency shift of the entire ^{1}H spectrum, microscopic susceptibility gradients that exist within a voxel (typically on the order of few mm^3) that contains mixtures of water and fat spins are expected to change the water-fat frequency separation. In order to quantify these susceptibility-induced relative frequency shifts and assess their effect on the accuracy of MR FF quantification methods, two magnitude-based reconstruction algorithms were used. Magnitude-based (only the magnitude of the signal is retained in the analysis) reconstruction algorithms were chosen over complex-based (real and

imaginary part of the signal is analyzed) reconstruction algorithms as these are immune to macroscopic field in homogeneities, which generally produce an overall phase shift of the signal (thus affect both the real and imaginary part of the signal) without affecting its magnitude, thus enabling for an independent assessment of the effect of microscopic inhomogeneities generated by susceptibility gradients.

The first algorithm (which we called the fixed spectral model) used was a standard magnitude-based reconstruction algorithm. This was a three-variable, magnitude-based reconstruction algorithm, where the magnitude of the signal was fitted by using the following equation:

$$|S_n| = |(M_w + C_n M_f) e^{-R^*_{2eff} TE_n}| \quad (6.1),$$

with C_n being:

$$C_n = \sum_{i=1}^{7} w_i e^{j(2\pi \Delta f_i TE_n)} \quad (6.2).$$

For this model, a seven-peak fat spectral model with well defined w_i and Δf_i values (fixed spectral model), as described in Ren J. *et al.* 2008,[102] was assumed, as previously done by Hu *et al.* 2013 and Zhong *et al.* 2014.[19,94]

The signal fit was then optimized in Python (Python Software Foundation, Wilmington, Delaware, USA) using a Levenberg-Marquardt algorithm, as described by Zhong *et al.* 2014, where all unknowns (M_w, M_f, and R^*_{2eff}) are estimated for each voxel, separately.[94]

A second magnitude-based CSE algorithm (which we called the variable spectral model) was implemented by modifying the above reconstruction algorithm to include an additional fitting parameter, the susceptibility-induced water-fat frequency shift δ, which accounts for possible

variations of the water-fat frequency separation:

$$C_n = \sum_{i=1}^{7} w_i e^{j(2\pi(\Delta f_i + \delta)TE_n)} \quad (6.3).$$

In this case, the parameters were estimated by using the results of the fixed spectral model as initial values for the second Levenberg-Marquardt-based reconstruction algorithm to estimate FF and δ values.

Section 6.3: Computational Experiments

We first simulated the magnetic susceptibility gradients produced by a variety of different microscopic water-fat distributions. We then looked at the effect of the simulated fields on FF quantification. The simulated water-fat distributions included multiple cylindrical, droplet and layered geometries, as well as a few including different water-fat distributions within the same voxel, as shown in Figure 6.1 a.

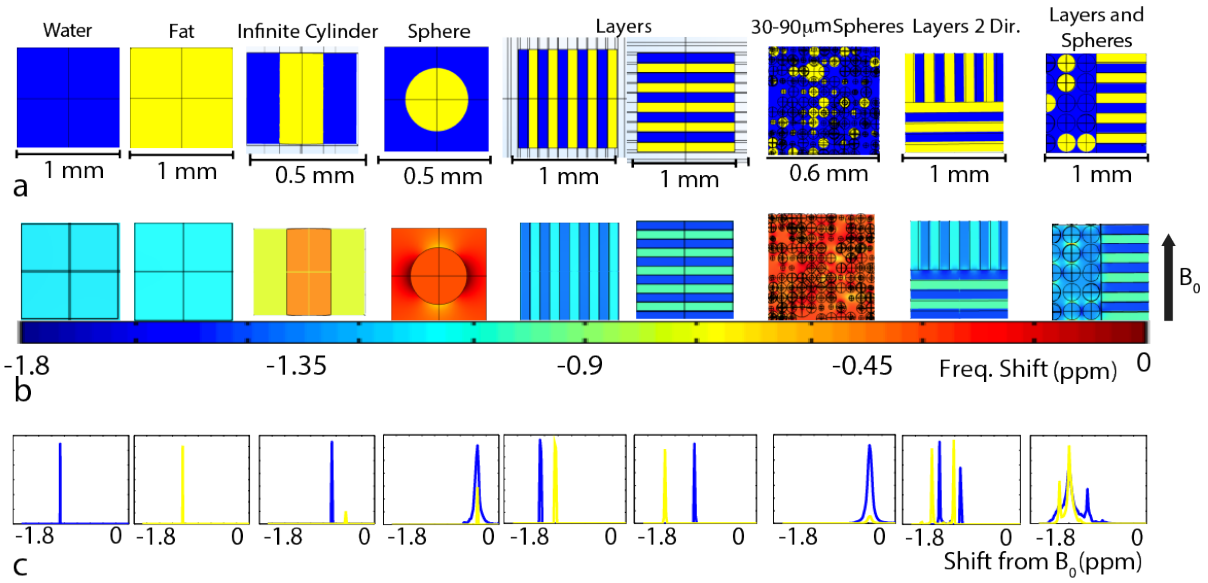

Figure 6.1 a. Cartoon of simulated water (blue) and fat (yellow) distributions. Please note the small scale used to analyze the effect of intra-voxel susceptibility gradients b. Map of the magnetic susceptibility-induced frequency shift for the above distributions. c. Histograms of the water (blue) and fat (yellow) frequency distributions for the simulated voxel.

For all simulations, COMSOL Multiphysics software (COMSOL Inc., Palo Alto, California, USA) was used to compute the field distribution. All simulations were performed assuming a static magnetic field B_o of 3T (the same field strength used experimentally), and a volume magnetic susceptibility of -9.04 ppm,[114] in SI units, for water compartments, and -7.79 ppm for fat compartments.[115] After solving the Maxwell equations in COMSOL, the sphere of Lorentz correction was applied,[116] and the computed 3D magnetic vector field, shown in Figure 6.1 b, was exported to MATLAB. The water and fat signal evolution was then computed for each spin in the given voxel for several echo times: TE_n= [1.12, 2.34, 3.56, 4.78, 6.00, 7.39] ms, which matched those used experimentally. The frequency distribution of water and fat spins, shown in Figure 6.1 c, their relative difference, and the ratio of fat and water spins (true FF) was computed for each distribution by using the field map, assuming a T2* = 25 ms, and a macroscopic B_0-field inhomogeneity of 0 Hz.[109] Signal magnitude and phase for each of the above echo times were fed into the reconstruction algorithms to obtain a FF measure as well as the value of δ in field-independent units (ppm), using the fixed ($\delta = 0$) and a variable spectral model. The results of these computations are shown in Table 6.1.

Geometry	Water Shift (ppm)	Fat Shift (ppm)	Water-Fat Susceptibility induced Shift (ppm)	True FF (%)	Estimated δ (ppm)	FF δ=0 (%)	FF Variable δ (%)
Water	1.07	N/A	N/A	0.00	N/A	0.00	N/A
Fat	N/A	1.04	N/A	100.0	N/A	99.92	N/A
Vertical Infinite Cylinder	0.67	0.46	0.217	13.4	0.217	12.80	13.39
Horizontal Infinite Cylinder	0.67	0.75	-0.083	14.2	-0.096	13.25	14.52

Infinite Vertical Layers	1.26	1.04	0.217	50.0	0.217	48.03	49.97
Infinite Horizontal Layers	0.92	1.35	-0.434	50.0	-0.434	32.46	50.00
30 um fat sphere	0.34	0.34	0	8.0	-0.010	8.37	8.42
Fat spheres 30um to 90um in random distribution	0.35	0.35	0.001	18.4	-0.007	18.78	18.82
Vertical and Horizontal Layers	1.09	1.19	-0.104	53.0	-0.107	50.34	52.94
Vertical Layers and fat spheres	1.14	1.12	0.018	37.9	0.053	39.55	39.37
Horizontal Layers and fat spheres	1.16	1.21	-0.055	37.9	-0.037	38.95	39.22

Table 6.1 Results of the B-field computations. From the water and fat frequency distribution, average water frequency shift, the average fat frequency shift, and the average water-fat frequency separation were calculated. The true FF value was the one used in the simulations. The estimated δ was the one computed by the variable spectra fit. The FF and variable FF were taken from the fixed spectra fit ($\delta = 0$) and variable spectra fit, respectively.

Overall, microscopic susceptibility gradients shifted water and fat resonances by different amounts in non-spherical geometries. This caused the relative water-fat frequency separation to vary from -0.4 ppm to 0.2 ppm. As these simulations show, not only the relative water-fat distribution, but also its orientation with respect to B_o matters, as one would expect. For example, for the infinite layers sample, a simple rotation of the sample with respect to the B_o field was able to induce a water-fat frequency shift as large as 0.6 ppm. These shifts induced an error in the standard FF quantification as large as 18% when water-fat frequency shifts of 0.4 ppm are seen. In other geometries, the susceptibility-induced shift was on the order of 0.2 ppm, inducing a FF error on the order of 2-3%.

The reconstruction algorithm with the variable water-fat frequency separation was able to quantify correctly the average water-fat frequency separation computed from the field map within 0.011 ppm, and estimate the true FF with an error of less than 1%, compared to an average error

of 4.5% of the reconstruction algorithm with the fixed water-fat frequency separation. However, when the distribution of water and fat spins gave rise to a bimodal frequency distribution for one or both spin species, errors as large as 3% were seen, even when a spectral model with a variable water-fat frequency separation was employed. In these cases, accounting for a susceptibility-induced frequency shift was not enough to correctly quantify FF.

Section 6.4: Phantom Experiments

Phantom experiments were preformed to validate the magnitude of the simulated susceptibility-induced shifts and resultant FF differences. For these experiments, samples consisted of one heterogenous mixture of water and fat spins: a bovine meat sample containing layers of muscle, fat, and bone, and a homogeneous mixture of water and fat spins: 20% intralipid fat emulsion sample (Sigma-Aldrich, St. Louis, Missouri, USA). Single-voxel spectroscopy (SVS) and CSE data were acquired. Each sample was then rotated by 90° with respect to the B_0 field and Spectroscopy and CSE data were re-acquired.

In-vitro experiments were performed on a Biograph mMR 3T (Siemens Healthcare, Germany). For all experiments, samples were equilibrated for 1.5 hours at bore temperature, measured by using a fiber optic temperature probe. For SVS measurements, a point-resolved spectroscopy (PRESS) sequence was used. The ^{1}H spectra were fit in MATLAB by using pseudo-Voigt profiles and, from each spectrum, the water-methylene resonance frequency shift was measured. Spectra with distorted lineshapes, where peaks were split, could not be accurately fitted and were excluded from the analysis. The 3D CSE imaging data were processed using the two reconstruction algorithms. Since all in-vitro experiments were performed with a sample temperature of 24°C, a mean water-fat frequency separation of 3.53 ppm was used to account for the temperature-induced

shift (-0.01ppm/°C) of the water resonance frequency.

The spectroscopy data showed the water-fat frequency, δ, displayed a significant dependence on field orientation in the meat sample. Shown in Figure 6.2, the mean value and the standard deviation of the water-fat frequency separation for the meat sample were: 3.75±0.15 ppm, when the muscle and fat layers were oriented orthogonal to the B_o field; 3.59±0.04 ppm, when the muscle and fat layers were oriented parallel the B_o field (P=0.049); 3.67±0.04 ppm, when looking across both orientations. Although the mean difference in water-fat frequency separation between the two orientations was 0.2 ppm, across the entire sample, the difference was measured to be as large as 0.42 ppm. This is in line with the magnitude of the shifts predicted computationally. For the intralipid solution, the mean water-fat frequency separations and standard deviations were: 3.57±0.03 ppm for parallel position; 3.61±0.13 ppm for a position perpendicular to the B_o field; (P=0.099) 3.59±0.01 ppm for the combined positions. In this case, a rotation of the sample with respect to the main field B_o did not produce any significant change in the water-fat frequency difference, as one would expect given the isotropy of the sample.

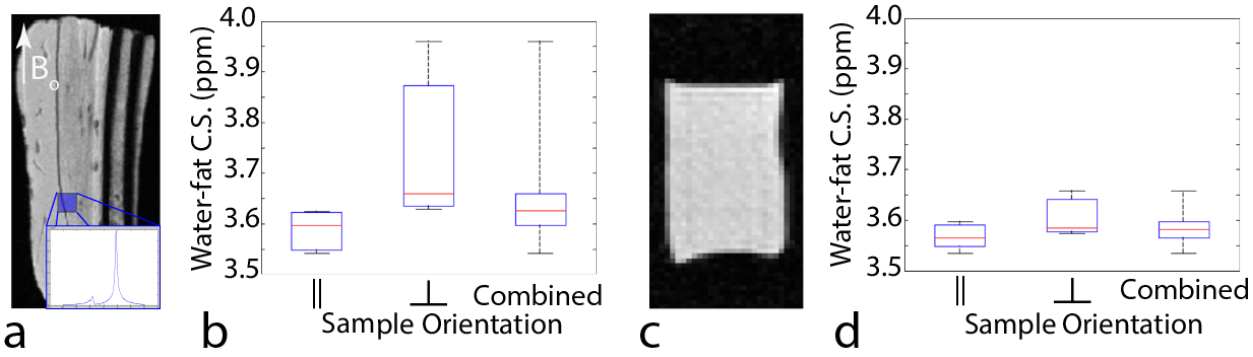

Figure 6.2. a. Coronal slice of a 3D gradient echo data set of the meat sample, sketching the location of one of the spectroscopy voxels and the direction of B_o for the fat layers aligned parallel to B_o. b. Box plot of the water-methylene frequency separation obtained from N=5 SVS spectra acquired on the meat sample oriented with the fat layers aligned parallel to the direction of B_o, orthogonal to the direction of B_o, and for the combined alignments. c. Axial slice of the first echo

image of the intralipid phantom illustrating the geometry. d. Boxplot of the water-methylene frequency separation obtained from N=5 SVS spectra taken with the main axis of the centrifuge tube aligned parallel and perpendicular to the main magnetic field, and for the combined sample orientations.

We then analyzed the question whether the variable signal model was able to model correctly these shifts and what the effect was on the accuracy of the FF calculation. The water-fat shift, δ, maps in the inhomogeneous phantom shown in Figure 6.3, show that when muscle-fat layers are oriented along the main field B_o, the largest susceptibility-induced frequency shift (δ=± 0.7 ppm) is seen at water-fat boundaries and the standard deviation in the frequency shift is around 0.20 ppm. As expected, and in agreement with the simulated results, a larger susceptibility-induced frequency shift (δ=±1ppm) is seen when the muscle-fat layers are oriented perpendicular to the direction of the main field B_o. These significant shifts in δ lead to large differences in FF between signal models. Shown in Figure 6.4, the larger differences in FF on the order of 5% are seen predominately at the interfaces between the muscle and fat layers, however significant differences are obtained also within the muscle and fat layers with the standard deviation in the FF difference being on the order of 3% for both orientations.

To make sure that the differences in FFs we are seeing in the meat sample were driven by shifts in the water-fat shift, δ, we looked at the relationship between FF and δ shown in Figure 6.5. As expected, FF difference increases sharply with δ, with a FF difference of 3% being caused by a δ of 0.3 ppm. Interestingly however, this dependence levels out, with only a small increase in FF difference for $\delta > 0.3$ ppm.

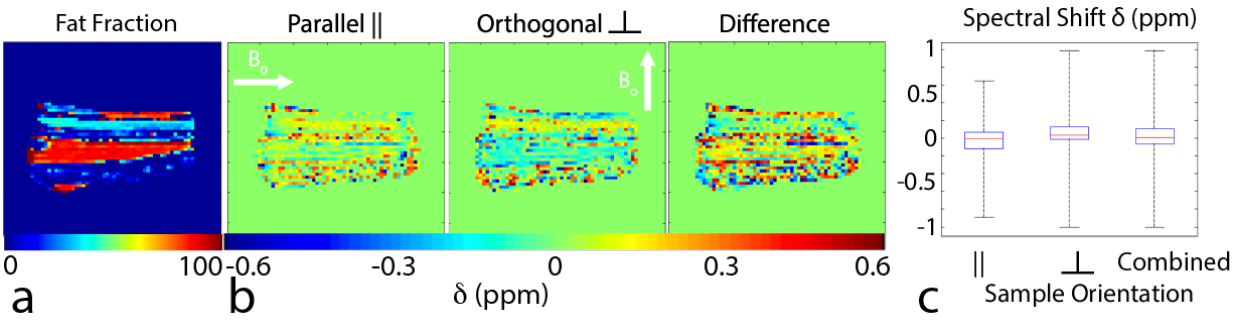

Figure 6.3. a. FF map obtained using the reconstruction algorithm with the fixed water-fat separation. b. 2D maps and box-lot of the susceptibility-induced water-fat frequency shift (δ) for different orientations of the meat sample. c. Boxplots of the susceptibility-induced water-fat frequency shift (δ) for both orientations and the two orientations combined. The mean susceptibility-induced frequency shift δ and standard deviations were: orthogonal, -0.01±0.19 ppm, parallel 0.05±0.17 ppm, (P<0.001), combined 0.02±0.18 ppm.

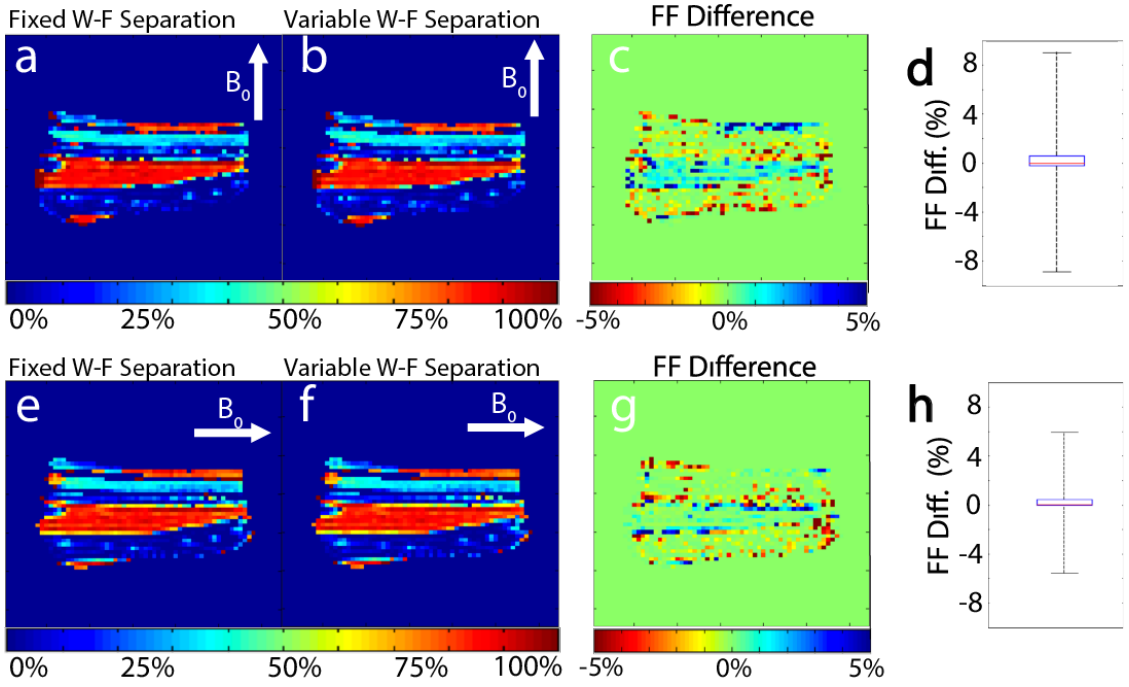

Figure 6.4. a-b. FF map of the meat phantom with the fat layers oriented orthogonally to the B_o field as obtained with the two algorithms: magnitude-based algorithms with a fixed (a) water-fat frequency separation and a variable (b) water-fat frequency separation. c. Difference map between the two reconstruction algorithms. d. Boxplot of the difference in FF values. Mean FF difference and standard deviation: 0.48±2.98%. e-f. FF map of the meat phantom with the fat layers oriented parallel to the B_o field as obtained with the magnitude-based reconstruction algorithms with a fixed (e) and a variable (f) water-fat frequency separation. g. Difference map between the two reconstruction algorithms. h. Boxplot of the difference in FF values. Mean FF difference and

standard deviation: 0.22±2.88%. For the two orientations, the distributions of the difference in FF values showed significant differences using a two-sample t-test (p<0.03).

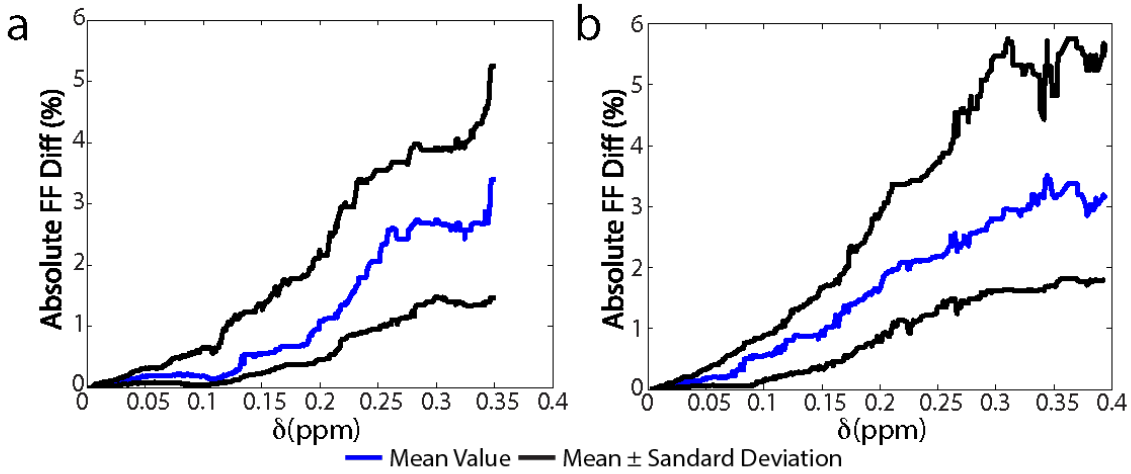

Figure 6.5. a-b. Plot of the difference in FF values obtained from the two reconstruction algorithms as a function of the susceptibility-induced frequency shift δ for the meat sample in the (a) orthogonal and (b) parallel orientation. Individual voxels were ordered based on FF difference and 15 voxels on either side were interpolated over to determine the mean water-fat frequency separation and standard deviation for each FF difference. The blue line shows the mean frequency shift while the black lines shows the mean FF ± the standard deviation.

Section 6.5: Experiments in Humans

To assess the impact of the magnetic susceptibility shifts on FF quantification in vivo, we acquired 3D CSE and spectroscopic data in the supraclavicular region of 14 healthy volunteers. New MR scans were acquired simultaneously with FDG-PET maps in nine of them using a protocol previously described in Chapter 3, and in McCallister *et al*. 2017.[117] All PET images in the supraclavicular area were acquired simultaneously with the 3D CSE data, which were acquired using a ^{1}H chest coil strapped around the shoulders. The CSE data were then fit using the two reconstruction algorithms with a water-fat frequency separation (water-methylene) of 3.4

ppm at 37°C[109].Chemical shift imaging (CSI) and single voxel spectroscopy were also acquired on a PRISMA 3T scanner (Siemens Healthcare, Germany) in five additional volunteers. From the spectrum of each CSI voxel containing supraclavicular fat tissue, the water-methylene resonance frequency shift was extracted. Again, spectra with distorted lineshapes or bimodal water and fat frequency distributions that could not be accurately fitted were excluded from the analysis.

Overall, there was a significant difference in FF between the two signal models as shown in Figure 6.6. Although the mean supraclavicular FF measured with the two spectral models was quite similar; 70% compared to 69% with a mean difference of 0.8% FF and a standard deviation of 2.8%, differences in FF in individual voxels was on the order of 5%. These differences in FF were caused by a water-fat frequency separation that, for some voxels, deviated from the nominal 3.4 ppm by as much as 0.5 ppm. When the goodness of the individual fit models was examined voxel by voxel by using the Bayesian information criterion (BIC), 88% of voxels within the supraclavicular fat depot showed that the second reconstruction algorithm, the one that accounted for a susceptibility-induced water-fat frequency shift δ, was significantly better (difference in BIC > 6) than the first reconstruction algorithm, which didn't account for a variability in the water-fat frequency separation.

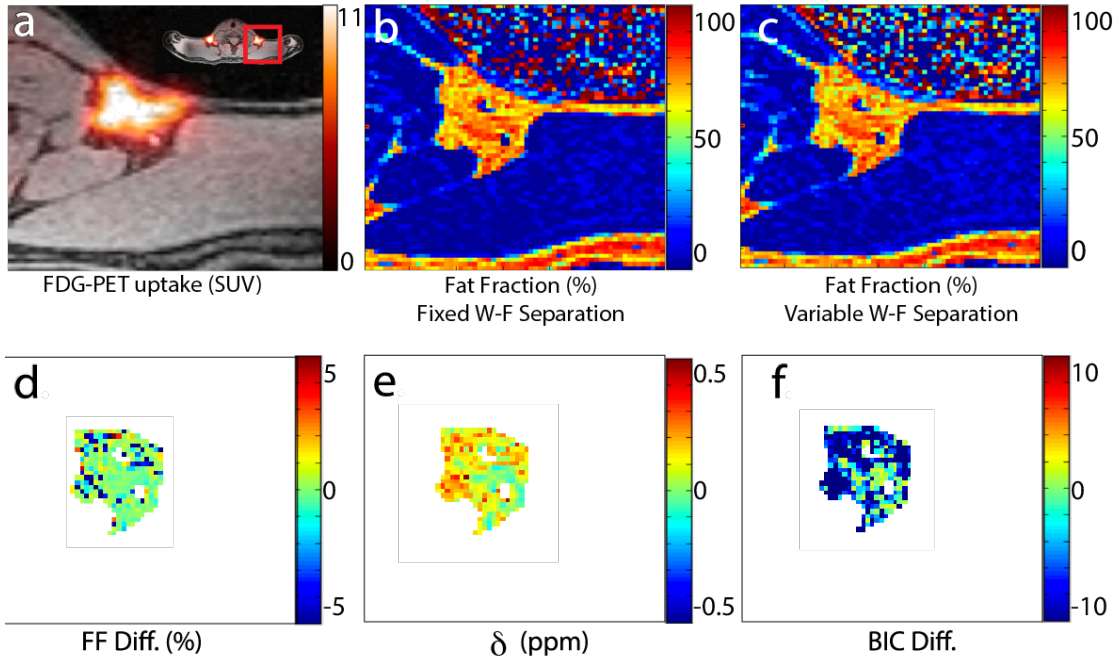

Figure 6.6. a. Axial slice from one of the subjects highlighting the glucose avid supraclavicular region. The red square indicates the region of interest analyzed. Significant FDG-uptake can be seen in the same region analyzed. b. FF map of the highlighted region as obtained by using the first magnitude-based reconstruction algorithm. c. FF map of the same region as obtained by using the second reconstruction algorithm that accounts for the susceptibility-induced water-fat frequency shift. For this subject, the mean difference in FF between the two reconstruction algorithms was -0.8%, with a standard deviation of 2.8%. d. Difference map masked at 40% FF to highlight the supraclavicular fat depot. e. Masked map of the susceptibility-induced frequency shift δ as obtained from the second reconstruction algorithm. f. Masked map of the difference in BIC values between the two reconstruction algorithms ($BIC_{variable}$-BIC_{fixed}).

When looking at the same map for the entire region in the same subject, interestingly, in muscle the two reconstruction algorithms show even larger δ values and FF differences. The second algorithm shows a systematically higher FF of up to 11%, which is greater than the difference shown in supraclavicular fat. However, unlike in the supraclavicular fat region, when the goodness of the individual fit models was examined voxel by voxel by using the Bayesian information criterion (BIC), the majority of the voxels (78%) showed no improvement with the variable spectral model (difference in BIC < 2).

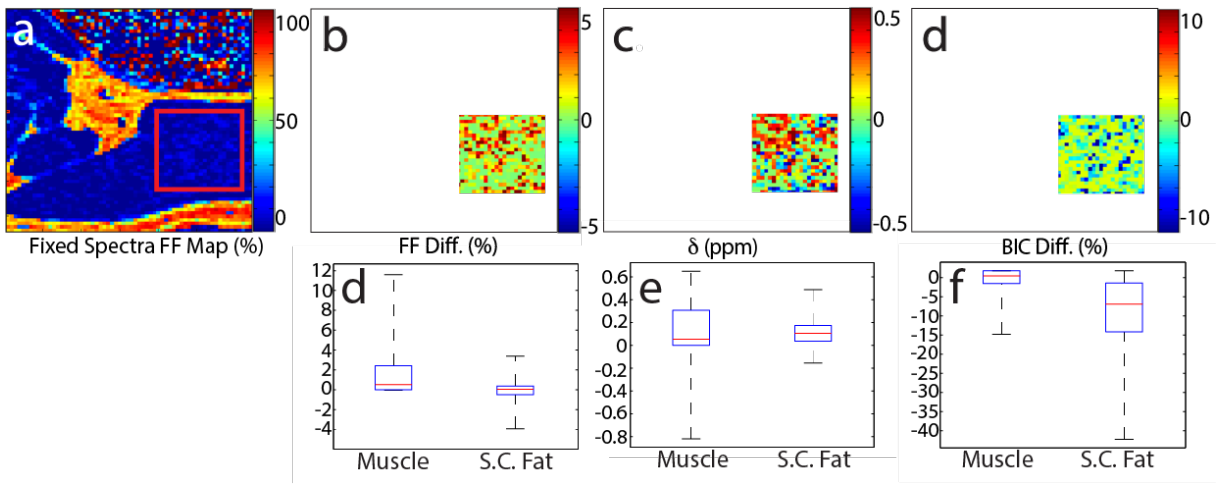

Figure 6.7. a. FF map of the supraclavicular region of Subject 5 (23 y.o. female with a BMI of 21). The red square indicates the region analyzed as muscular tissue. Supraclavicular fat is defined as the masked region in Figure 6. b. Full un-masked FF difference map. c. Full un-masked map of the susceptibility-induced water-fat frequency shift δ as obtained from the second reconstruction algorithm. d. Full un-masked map of the difference in BIC values between the two reconstruction algorithms ($BIC_{variable}$-BIC_{fixed}). e. Box plot of the FF difference seen in muscle (1.4±1.8%) and supraclavicular fat (-0.8±2.8%) f. Box plot of the susceptibility-induced water-fat frequency shift δ in muscle (0.11±0.23 ppm) and supraclavicular fat (0.11±0.10 ppm). g. Box plot of the BIC difference in muscle (0.7±3.5) and supraclavicular fat (-8.8±8.8 ppm).

Looking at the trends across all subjects shown in Figure 6.8, the two reconstruction algorithms produced similar FF values. The average water-fat frequency separation was 3.49±0.15 ppm (δ = 0.09±0.15 ppm), with values ranging from 3 ppm (δ = -0.4 ppm) to 4 ppm (δ = 0.6 ppm).

Blandt-Aldman plots of every voxel in the supraclavicular fat region were created for all 6 lean subjects. The difference in FF values obtained from the two reconstruction algorithms is plotted against the average of the two FF values. Clearly, the two reconstruction algorithms produced similar FF values for most of the voxels, with a mean difference in FF of 1.2% and a standard deviation of 5.26%. However, for some of the voxels, especially those with a FF ranging between 40% and 60%, differences in FF ranged from -25% to 15%.

To further validate the presence of large susceptibility-induced water-fat frequency shifts *in-*

vivo directly, we measured the water-fat frequency shift, δ, as obtained from the 5 subjects that underwent the CSI scans shown in Figure 6.8 d. Across all five subjects the water-fat frequency separation had a mean of 3.44±0.16 ppm and ranged from 3.1 to 3.8 ppm, nicely matching the range of the δ maps obtained by using the variable shift signal model.

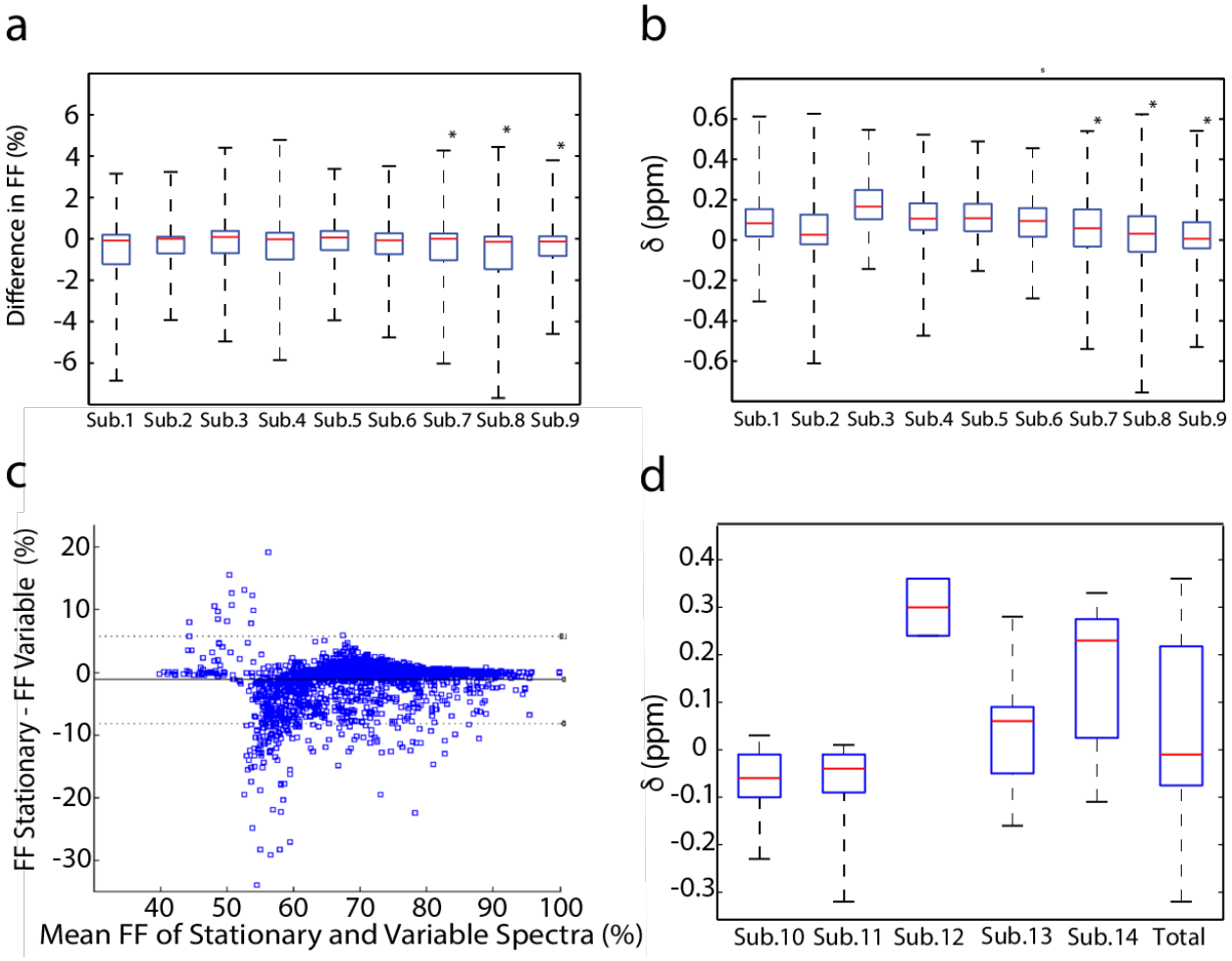

Figure 6.8. a. Boxplot of the difference in FF values measured with the two reconstruction algorithms for the supraclavicular fat depot of all 9 subjects. b. Boxplot of the susceptibility-induced water-fat frequency shift δ for all 9 subjects. c. Bland-Altman plot of the two magnitude-based reconstruction algorithms for all 6 lean subjects from an axial slice encompassing the supraclavicular region and masked with a 40% FF. d. Boxplot of the susceptibility-induced water-fat frequency shift δ as measured by CSI in the supraclavicular fat region for five subjects. Values are displayed relative to the nominal value of 3.4 ppm. When combined, the mean difference in separation was 0.04±0.16 ppm, with a range from -0.3 to 0.4 ppm. * denotes overweight and obese subjects

Section 6.6: Discussion

Unlike the effect of macroscopic field inhomogeneities, which are often accounted for in CSE FF quantification reconstruction algorithms, the effect of microscopic susceptibility gradients present within a single voxel on CSE FF quantification has been left largely unexplored. Here we show that the shift produced by microscopic susceptibility gradients on the water-fat frequency separation in a magnetically heterogeneous region like in the supraclavicular fat region, are on average 0.1 ppm with a standard deviation of 0.2 ppm, but with individual values ranging from a minimum of -0.3 ppm to a maximum of 0.6 ppm. The magnitude of these shifts is consistent with the magnitude of the simulated water-fat frequency shifts caused by microscopic susceptibility gradients as computed in this study. This is not surprising as the supraclavicular tissue, at the microscopic level, is highly heterogeneous, with nerves, brown fat, white fat, and blood vessels that often are not resolved in MR images. Further confirmation of the validity of our simulations comes from CSI analysis of supraclavicular fat, where the measured water-fat frequency shifts ranged from -0.3 ppm to 0.4 ppm. These susceptibility-induced frequency shifts are equivalent to the frequency shifts induced by a change in temperature from +30°C to -40°C, thus much larger than the small temperature-induced shift of a few hundredths of a ppm that can be expected from activation of BAT in humans.

The mean water-fat frequency separation in supraclavicular fat tissue was shown to be around 3.5 ppm, higher than the 3.4 ppm water-fat separation often used for FF quantification[95]. This is not surprising, as the 3.4 ppm value was originally measured in human liver, where the microscopic distribution of water and fat spins is expected to be much different than in the supraclavicular fat. As shown by our simulation and in-vitro experiments, the water-fat separation strongly depends on the specific microscopic distribution of water and fat spins and on its orientation with respect

to B_o.

The simulations also show that these susceptibility-induced frequency shifts can produced FF errors as large as 18%, when not accounted for, and much smaller errors, on the order of 0.4%, when susceptibility-induced water-fat frequency shifts are included in the spectral model. Differences in FF between the two models ranged from less than 1% when the frequency shift was small (~0.1 ppm) up to 18% when the frequency shift was large (~0.4 ppm).

The CSE and CSI results in the phantoms mimicked these results showing large differences in the water fat frequency separation upon rotation in the field in the inhomogeneous, layered bovine phantom, while very little shift was observed in the homogenous droplet-like emulsion. Theoretically, these shifts have a possible range of 1.25 ppm, depending on the microscopic geometries; however, in simulations and phantom experiments a maximum deviation of 0.4 ppm was found to be realistic[118].

It is important to notice that both MR signal models assume a uniform distribution for both water and fat spins. However, as seen in the simulations, when the frequency distribution of one or both spin species is multimodal, both models fail to describe correctly the underlying signal, possibly giving rise to large FF errors. The variable spectral model does not correct for all biases such as these multimodal distributions, or for chemical shift displacement artifacts; however, it should minimize biases in inhomogeneous fatty tissues.

An analysis of the model's goodness suggests that the variable model, which accounts for susceptibility-induced frequency shifts, in general does a much better job in describing the underlying signal in regions in which water and fat almost equally contribute to the signal. However, in more homogenous tissues, when the contribution to the signal originates mainly from

one of the two components (water or fat), this is no longer the case. In this case, the problem seems to be ill-conditioned in the presence of noise; if one of the species is present at much lower concentrations, it is harder to estimate the frequency separation between two spins. In this case, the second model that accounts for the susceptibility-induced frequency shift, by introducing an additional degree of freedom, may actually degrade model performance. In this case, a possible solution could be the use of a constrained reconstruction algorithm at the expense of increased complexity.

The detected FF error measured in this study (1±5%) may not seem to be significant. However, when looking at small changes in tissue FFs, as those expected in BAT during stimulation of thermogenesis, an error of 5% can make the results unreliable[22]. Such errors could indeed explain the contrasting results obtained in humans BAT when measuring changes in tissue FF during cold exposure by FF techniques.

Section 6.7: Conclusion

In inhomogeneous tissues in which water and fat spins both contribute to the MR signal, microscopic magnetic susceptibility gradients induce a shift of the water-fat frequency separation by as much as ±0.4 ppm, which can lead to differences in estimations of tissue FF in individual voxels on the order of 5%. Since the magnitude of the shift strongly depends on the microscopic distribution of water and fat spins within the MR voxel, as well as on its orientation with respect to B_0, its value is expected to vary from voxel to voxel. As we have shown here, the error can be minimized by using a reconstruction algorithm that employs a spectral model that accounts for the susceptibility induced water-fat frequency shift.

We should point out that frequency lineshapes in magnetic resonance are mainly the results of magnetic field distortions experienced by the spins. As these gradients are in general very complicated, their effect cannot be easily removed. Yet, frequency lineshapes are often modeled as Gaussian, Lorentian or, in the best case, Voigt functions, completely ignoring the fact that magnetic field gradients can have a much more pronounced effect on spectral lineshapes.

Another interesting point to make is that the accuracy of CSE FF quantification techniques has always been measured by comparing the FF result obtained with these methods to the FF result obtained by using single voxel spectroscopy measurements, considered to be the MR gold standard. When the second was tried in our lab, it became obvious that, with the exception of few samples, severe distortion of spectral lineshapes made it impossible to quantify FF correctly to within a 10% uncertainty even when the sample was shimmed using higher order shimming gradients. To this end, validation of these methods seems, at a minimum, questionable, especially when the single voxel spectroscopy data and its fitting are not reported, which is typically the case.

REFERENCES

1. Nikolaou P, Coffey AM, Walkup LL, Gust BM, Whiting N, Newton H, Barcus S, Muradyan I, Dabaghyan M, Moroz GD, et al. Near-unity nuclear polarization with an open-source 129Xe hyperpolarizer for NMR and MRI. Proceedings of the National Academy of Sciences of the United States of America. 2013;110(35):14150–5.

2. Antonacci MA, Burant A, Wagner W, Branca RT. Depolarization of nuclear spin polarized 129 Xe gas by dark rubidium during spin-exchange optical pumping. Journal of Magnetic Resonance. 2017;279:60–67.

3. Burant A, Branca RT. Diffusion-mediated 129 Xe Gas Depolarization in Magnetic Field Gradients During Continuous-flow Optical Pumping. Journal of Magnetic Resonance. 2016;273:124–129.

4. Couch MJ, Ball IK, Li T, Fox MS, Biman B, Albert MS. 19F MRI of the Lungs Using Inert Fluorinated Gases : Challenges and New Developments. 2018.

5. Lowell BB, S-Susulic V, Hamann A, Lawitts J a, Himms-Hagen J, Boyer BB, Kozak LP, Flier JS. Development of obesity in transgenic mice after genetic ablation of brown adipose tissue. Nature. 1993;366(6457):740–742.

6. Ma S, Foster D. Uptake of glucose and release of fatty acids and glycerol by rat brown adipose tissue in vivo. CAN. J. PHYSIOL. PHARMACOL. 1986;64:609–614.

7. Cannon B, Nedergaard J. Metabolic consequences of the presence or absence of the thermogenic capacity of brown adipose tissue in mice (and probably in humans). International journal of obesity (2005). 2010;34 Suppl 1(S1):S7-16.

8. Seale P, Lazar M a. Brown fat in humans: Turning up the heat on obesity. Diabetes. 2009;58(7):1482–1484.

9. Cannon B. Brown Adipose Tissue: Function and Physiological Significance. Physiological Reviews. 2004;84(1):277–359.

10. Nedergaard J, Bengtsson T, Cannon B. Unexpected evidence for active brown adipose tissue in adult humans. American journal of physiology. Endocrinology and metabolism. 2007;293(2):E444–E452.

11. Cypess AM, Haft CR, Laughlin MR, Hu HH. Brown Fat in Humans: Consensus Points and Experimental Guidelines. Cell Metabolism. 2014;20(3):408–415.

12. Zhang L, Burant A, Mccallister A, Zhao V, Koshlap KM, Degan S, Antonacci M, Branca RT. Accurate MR thermometry by hyperpolarized 129Xe. Magnetic Resonance in Medicine. 2016;00:1–10.

13. Rasmussen JM, Entringer S, Nguyen A, Van Erp TGM, Guijarro A, Oveisi F, Swanson JM, Piomelli D, Wadhwa PD, Buss C, et al. Brown adipose tissue quantification in human neonates

using water-fat separated MRI. PLoS ONE. 2013;8(10).

14. Gifford A, Towse TF, Walker RC, Avison MJ, Welch EB. Characterizing Active and Inactive Brown Adipose Tissue in Adult Humans Using PET-CT and MR Imaging. American Journal of Physiology - Endocrinology And Metabolism. 2016:ajpendo.00482.2015.

15. Gifford A, Walker RC, Towse TF, Brian Welch E. Correlations between quantitative fat-water magnetic resonance imaging and computed tomography in human subcutaneous white adipose tissue. Journal of medical imaging (Bellingham, Wash.). 2015;2(4):046001.

16. van Rooijen BD, van der Lans A a JJ, Brans B, Wildberger JE, Mottaghy FM, Schrauwen P, Backes WH, van Marken Lichtenbelt WD. Imaging Cold-Activated Brown Adipose Tissue Using Dynamic T2*-Weighted Magnetic Resonance Imaging and 2-Deoxy-2-[18F]fluoro-D-glucose Positron Emission Tomography. Investigative Radiology. 2013;48(10):1–7.

17. Hu HH, Smith DL, Nayak KS, Goran MI, Nagy TR. Identification of brown adipose tissue in mice with fat-water IDEAL-MRI. Journal of Magnetic Resonance Imaging. 2010;31(5):1195–1202.

18. Heaton JM. The distribution of brown adipose tissue in the human. Journal of anatomy. 1972;112(Pt 1):35–9.

19. Hu HH, Perkins TG, Chia JM, Gilsanz V. Characterization of Human Brown Adipose Tissue by Chemical-Shift Water-Fat MRI. AJR Am J Roentgenol. 2013;200(1):177–183.

20. Ehman EC, Johnson GB, Villanueva-meyer JE, Cha S, Leynes AP, Eric P, Larson Z, Hope TA. PET/MRI: Where Might It Replace PET/CT? J Magn Reson Imaging. 2017;46(5):1247–1262.

21. McCallister A, Zhang L, Burant A, Katz L, Branca RT. A pilot study on the correlation between fat fraction values and glucose uptake values in supraclavicular fat by simultaneous PET/MRI. Magnetic Resonance in Medicine. 2017;00(November 2016).

22. Lundström E, Strand R, Johansson L, Bergsten P, Ahlström H, Kullberg J. Magnetic Resonance Imaging Cooling-Reheating Protocol Indicates Decreased Fat Fraction via Lipid Consumption in Suspected Brown Adipose Tissue. Plos One. 2015;10(4):e0126705.

23. Baron P, Deckers R, Bouwman JG, Bakker CJG, De Greef M, Viergever MA, Moonen CTW, Bartels LW. Influence of water and fat heterogeneity on fat-referenced MR thermometry. Magnetic Resonance in Medicine. 2016;75(3):1187–1197.

24. Hansen KH, Schroeder ME, Hamilton G, Sirlin CB, Bydder M. Robustness of Fat Quantification using Chemical Shift Imaging. Magnetic Resonance Imaging. 2012;30(2):151–157.

25. Reeder SB, Pineda AR, Wen Z, Shimakawa A, Yu H, Brittain JH, Gold GE, Beaulieu CH, Pelc NT. Iterative decomposition of water and fat with echo asymmetry and least-squares estimation (IDEAL): Application with fast spin-echo imaging. Magnetic Resonance in Medicine.

2005;54(3):636–644.

26. Yu H, Shimakawa A, Hines CDG, McKenzie CA, Hamilton G, Sirlin CB, Brittain JH, Reeder SB. Combination of complex-based and magnitude-based multiecho water-fat separation for accurate quantification of fat-fraction. Magnetic Resonance in Medicine. 2011;66(1):199–206.

27. Walker, Thad G. (Department of Physics, University of Wisconsin-Madison, Madison W 53706), Happer, William (Department of Physics, Princeton University, Princeton NJ 08544). Spin-exchange optical pumping of noble-gas nuclei. Reviews of Modern Physics. 1997;69(2):629–642.

28. Nikolaou P, Coffey AM, Walkup LL, Gust BM, Whiting N, Newton H, Muradyan I, Dabaghyan M, Ranta K, Moroz GD, et al. 129Xe spin relaxation in frozen xenon. Reviews of Modern Physics. 2014;44(2):267–271.

29. Mugler JP, Altes TA, Ruset IC, Dregely IM, Mata JF, Miller GW, Ketel S, Ketel J, Hersman FW, Ruppert K. Simultaneous magnetic resonance imaging of ventilation distribution and gas uptake in the human lung using hyperpolarized xenon-129. Proceedings of the National Academy of Sciences. 2010;107(50):21707–21712.

30. Freeman MS, Emami K, Driehuys B. Characterizing and modeling the efficiency limits in large-scale production of hyperpolarized Xe 129. Physical Review A - Atomic, Molecular, and Optical Physics. 2014;90(2):1–14.

31. Schrank G, Ma Z, Schoeck A, Saam B. Characterization of a low-pressure high-capacity X 129 e flow-through polarizer. Physical Review A - Atomic, Molecular, and Optical Physics. 2009;80(6):1–10.

32. Ruset IC, Ketel S, Hersman FW. Optical pumping system design for large production of hyperpolarized Xe129. Physical Review Letters. 2006;96(5):8–11.

33. Driehuys B, Cates GD, Miron E, Sauer K, Walter DK, Happer W. High-volume production of laser-polarized ^{129} Xe. Applied Physics Letters. 1996;69(12):1668–1670.

34. Fitzgerald R, Gatzke M, Fox D, Cates G, Happer W. 129Xe spin relaxation in frozen xenon. Physical Review B. 1999;59(13):8795–8811.

35. Kuzma NN, Patton B, Raman K, Happer W. Fast Nuclear Spin Relaxation in Hyperpolarized Solid. Physical Review Letters. 2002;88(14):4.

36. Gamblin RL, Carver TR. Polarization and relaxation processes in He3 gas. Physical Review. 1965;138(4 A).

37. Schearer LD, Walters GK. Nuclear spin-lattice relaxation in the presence of magnetic-field gradients. Physical Review. 1965;139(5A):1398–1402.

38. Levitt MH. Spin Dynamics: Basics of Nuclear Magnetic Resonance 2nd Edition.

39. Kinahan PE, Fletcher JW. PET/CT Standardized Uptake Values (SUVs) in Clinical Practice and Assessing Response to Therapy. Semin Ultrasound CT MR. 2010;31(6):496–505.

40. Cates GD, Benton DR, Gatzke M, Happer W, Hasson KC, Newbury NR. Laser Production of Large Nuclear-Spin Polarization in Frozen Xenon. Physical Review Letters. 1990;65(20):2591–2594.

41. Chann B, Babcock E, Anderson L, Walker T. Skew light propagation in optically thick optical pumping cells. Physical Review A. 2002;66(3):1–3.

42. Kirchvink J. Uniform Magnetic Fields and Double wrapped Coil Systems. Bioelectromagnetics. 1992;(13):401–411.

43. Raich H, Blümler P. Design and construction of a dipolar Halbach array with a homogeneous field from identical bar magnets: NMR mandhalas. Concepts in Magnetic Resonance Part B: Magnetic Resonance Engineering. 2004;23(1):16–25.

44. Altes TA, Eichinger M, Puderbach M. Magnetic Resonance Imaging of the Lung in Cystic Fibrosis. 2007.

45. Kanhere N, Couch MJ, Kowalik K, Zanette B, Rayment JH, Manson D, Subbarao P, Ratjen F, Santyr G. Correlation of Lung Clearance Index with Hyperpolarized 129 Xe Magnetic Resonance Imaging in Pediatric Subjects with Cystic Fibrosis . American Journal of Respiratory and Critical Care Medicine. 2017;196(8):1073–1075.

46. Ebner L, Kammerman J, Driehuys B, Schiebler ML, Cadman R V., Fain SB. The role of hyperpolarized129xenon in MR imaging of pulmonary function. European Journal of Radiology. 2017;86:343–352.

47. Rao M, Stewart NJ, Norquay G, Griffiths PD, Wild JM. High resolution spectroscopy and chemical shift imaging of hyperpolarized ^{129} Xe dissolved in the human brain in vivo at 1.5 tesla. Magnetic Resonance in Medicine. 2016;75(6):2227–2234.

48. Couch MJ, Ball IK, Fox MS, Littlefield SL, Albert MS. F MR Imaging with Inhaled Fluorinated Gas Mixtures in Healthy Volunteers : Feasibility 1. 2013;269(3):903–909.

49. Gutberlet M, Kaireit TF, Voskrebenzev A, Lasch F, Freise J, Welte T, Wacker F, Hohlfeld JM, Vogel-Claussen J. Free-breathing Dynamic (19)F Gas MR Imaging for Mapping of Regional Lung Ventilation in Patients with COPD. Radiology. 2018;286(3):1040–1051.

50. Maunder A, Hughes PJC, Chan H, Norquay G, Collier G, Rodgers O, Rao M, Wild J. Comparing 19 F C3F8 Lung Ventilation Imaging with Hyperpolarized 129 Xe : Similarities and Limitations. In: Proc. Intl. Soc. Mag. Reson. Med. 26 (. 2018. p. 1083–1085.

51. Charles HC, Jones RW, Halaweish AF, Ainslie MD. Parallel Imaging for Short Breath Hold Times in Perfluorinated Gas Imaging of the Lung. Proc. Intl. Soc. Mag. Reson. Med. 23. 2015;23:3984.

52. Halaweish AF, Moon RE, Foster WM, Soher BJ, McAdams HP, MacFall JR, Ainslie MD, MacIntyre NR, Charles HC. Perfluoropropane gas as a magnetic resonance lung imaging contrast agent in humans. Chest. 2013;144(4):1300–1310.

53. Collins FS. Cystic Fibrosis: Molecular Biology & Therapeutic Implications. Science. 1992;256(5058):774–779.

54. Boucher RC. Muco-Obstructive Lung Diseases. New England Journal of Medicine. 2019;380(20):1941–1953.

55. Eichinger M, Heussel CP, Kauczor HU, Tiddens H, Puderbach M. Computed tomography and magnetic resonance imaging in cystic fibrosis lung disease. Journal of Magnetic Resonance Imaging. 2010;32(6):1370–1378.

56. Johnson KM, Fain SB, Schiebler ML, Nagle S. Optimized 3D ultrashort echo time pulmonary MRI. Magnetic Resonance in Medicine. 2013;70(5):1241–1250.

57. Roos JE, McAdams HP, Kaushik SS, Driehuys B. Hyperpolarized Gas MRI: Technique and Applications. Magn Reson Imaging Clin N Am. 2016;23(2):217–229.

58. Anvari A, Halpern EF, Samir AE. Essentials of Statistical Methods for Assessing Reliability and Agreement in Quantitative Imaging. Academic Radiology. 2017:1–6.

59. He M, Kaushik SS, Robertson SH, Freeman MS, Virgincar RS, McAdams HP, Driehuys B. Extending semiautomatic ventilation defect analysis for hyperpolarized 129Xe ventilation MRI. Academic Radiology. 2014;21(12):1530–1541.

60. Li C, Gore JC, Davatzikos C. Multiplicative intrinsic component optimization (MICO) for MRI bias field estimation and tissue segmentation. Magnetic Resonance Imaging. 2014;32(7):913–923.

61. Wild JM, Ajraoui S, Deppe MH, Parnell SR, Marshall H, Parra-Robles J, Ireland RH. Synchronous acquisition of hyperpolarised 3He and 1H MR images of the lungs - maximising mutual anatomical and functional information. NMR in Biomedicine. 2011;24(2):130–134.

62. Wild JM, Marshall H, Norquay G, Parnell SR, Clemence M, Griffiths PD. Simultaneous Imaging of Lung Structure and Function with Triple-Nuclear Hybrid MR Imaging. Radiology. 2013;267(1):251–255.

63. Neal MA, Pippard BJ, Hollingsworth KG, Maunder A, Dutta P, Simpson AJ, Blamire AM, Wild JM, Thelwall PE. Optimized and accelerated ^{19} F-MRI of inhaled perfluoropropane to assess regional pulmonary ventilation. Magnetic Resonance in Medicine. 2019;(March):mrm.27805.

64. Branca RT, McCallister A, Yuan H, Aghajanian A, Faber JE, Weimer N, Buchanan R, Floyd CS, Antonacci M, Zhang L, et al. Accurate quantification of brown adipose tissue mass by xenon-enhanced computed tomography. Proceedings of the National Academy of Sciences. 2018;115(1):174–179.

65. Lee P, Greenfield JR, Ho KKY, Fulham MJ. A critical appraisal of the prevalence and metabolic significance of brown adipose tissue in adult humans. American journal of physiology. Endocrinology and metabolism. 2010;299(4):E601-6.

66. Becker AS, Nagel HW, Wolfrum C, Burger IA. Anatomical grading for metabolic activity of brown adipose tissue. PLoS ONE. 2016;11(2):1–12.

67. Kety SS. The theory and applications of the exchange of inert gas at the lungs and tissues. Pharmacol Rev. 1951;3:1–41.

68. Wickler SJ, Horwitz BA, Stern JS. Blood flow to brown fat in lean and obese adrenalectomized Zucker rats. American Journal of Physiology. 1986;251(5):851–858.

69. Foster DO, Frydman ML. Tissue distribution of cold-induced thermogenesis in conscious warm- or cold-acclimated rats reevaluated from changes in tissue blood flow: the dominant role of brown adipose tissue in the replacement of shivering by nonshivering thermogenesis. Canadian journal of physiology and pharmacology. 1979;57(3):257–270.

70. Thurlby PL, Trayhurn P. Regional blood flow in genetically obese (ob/ob) mice. The importance of brown adipose tissue to the reduced energy expenditure on non-shivering thermogenesis. Pflugers Archiv : European journal of physiology. 1980;385(3):193–201.

71. Cannon B, Nedergaard J. The biochemistry of an inefficient tissue: brown adipose tissue. Essays in biochemistry. 1985;20:110–164.

72. Ricquier D, Gaillard JL, Turc JM. Microcalorimetry of isolated mitochondria from brown adipose tissue. FEBS Letters. 1979;99(1):203–206.

73. Cinti S. Between brown and white: novel aspects of adipocyte differentiation. Annals of medicine. 2011;43(2):104–115.

74. Lowell BB, Spiegelman BM. Towards a molecular understanding of adaptive thermogenesis. Nature. 2000;404(6778):652–660.

75. Mercer SW, Trayhurn P. Effect of high fat diets on energy balance and thermogenesis in brown adipose tissue of lean and genetically obese ob/ob mice. The Journal of nutrition. 1987;117(June):2147–2153.

76. Rothwell NJ, Stock MJ. A role for brown adipose tissue in diet-induced thermogenesis. Obesity research. 1997;5(6):650–656.

77. van der Lans a. a. JJ, Wierts R, Vosselman MJ, Schrauwen P, Brans B, van Marken Lichtenbelt WD. Cold-activated brown adipose tissue in human adults: methodological issues. AJP: Regulatory, Integrative and Comparative Physiology. 2014;307(2):R103–R113.

78. Brooks SL, Neville AM, Rothwell NJ, Stock MJ, Wilson S. Sympathetic activation of brown-adipose-tissue thermogenesis in cachexia. Bioscience Reports. 1981;512(1):509–517.

79. Foster DO, Frydman ML. Nonshivering thermogenesis in the rat. II. Measurements of blood flow with microspheres point to brown adipose tissue as the dominant site of the calorigenesis induced by noradrenaline. Canadian journal of physiology and pharmacology. 1978;56(1):110–122.

80. Gunawardana SC, Piston DW. Reversal of type 1 diabetes in mice by brown adipose tissue transplant. Diabetes. 2012;61(3):674–682.

81. van Marken Lichtenbelt W, Vanhommerig J, Smulders N, Drossearts J, Kemerink G, Bouvy N, Schrauwen P, Teule J. Cold-Activated Brown Adipose Tissue in Healthy Men. New England Journal of Medicine. 2009;360(15):1500–1508.

82. Cypess AM, Haft CR, Laughlin MR, Hu HH. Brown fat in humans: consensus points and experimental guidelines. Cell metabolism. 2014;20(3):408–15.

83. Orava J, Nuutila P, Lidell ME, Oikonen V, Noponen T, Viljanen T, Scheinin M, Taittonen M, Niemi T, Enerbäck S, et al. Different metabolic responses of human brown adipose tissue to activation by cold and insulin. Cell Metabolism. 2011;14(2):272–279.

84. Branca RT, He T, Zhang L, Floyd CS, Freeman M, White C, Burant A. Detection of brown adipose tissue and thermogenic activity in mice by hyperpolarized xenon MRI. Proceedings of the National Academy of Sciences. 2014;111(50):18001–18006.

85. Antonacci MA, Zhang L, Degan S, Erdmann D, Branca RT. Calibration of methylene-referenced lipid-dissolved xenon frequency for absolute MR temperature measurements. Magnetic Resonance in Medicine. 2019;81(2):765–772.

86. Antonacci MA, Zhang L, Burant A, McCallister D, Branca RT. Simple and robust referencing system enables identification of dissolved-phase xenon spectral frequencies. Magnetic Resonance in Medicine. 2018;80(2):431–441.

87. Bauwens M, Wierts R, Van Royen B, Bucerius J, Backes W, Mottaghy F, Brans B. Molecular imaging of brown adipose tissue in health and disease. European Journal of Nuclear Medicine and Molecular Imaging. 2014;41(4):776–791.

88. Chen YI, Cypess a M, Chen YC, Palmer M, Kolodny G, Kahn CR, Kwong KK. Measurement of human brown adipose tissue volume and activity using anatomic MR imaging and functional MR imaging. Journal of Nuclear Medicine. 2013;54(9):1584–1587.

89. Aherne W, Hull D. The Site of Heat Production in the Newborn Infant. Proceedings of the Royal Society of Medicine. 1964;57:1172–3.

90. Branca RT, Zhang L, Warren WS, Auerbach E, Khanna A, Degan S, Ugurbil K, Maronpot R. In Vivo Noninvasive Detection of Brown Adipose Tissue through Intermolecular Zero-Quantum MRI. PLoS ONE. 2013;8(9).

91. Kortelainen ML, Pelletier G, Ricquier D, Bukowiecki LJ. Immunohistochemical detection of human brown adipose tissue uncoupling protein in an autopsy series. The journal of

histochemistry and cytochemistry : official journal of the Histochemistry Society. 1993;41(5):759–764.

92. Ma J. Dixon techniques for water and fat imaging. Journal of Magnetic Resonance Imaging. 2008;28(3):543–558.

93. Dixon WT. Simple proton spectroscopic imaging. Radiology. 1984;153(1):189–194.

94. Zhong X, Nickel MD, Kannengiesser SAR, Dale BM, Kiefer B, Bashir MR. Liver fat quantification using a multi-step adaptive fitting approach with multi-echo GRE imaging. Magnetic Resonance in Medicine. 2014;72(5):1353–1365.

95. Wang X, Hernando D, Reeder SB. Sensitivity of Chemical Shift-Encoded Fat Quantification to Calibration of Fat MR Spectrum. Magnetic Resonance in Medicine. 2016;75(2):845–51.

96. Yu H, Shimakawa A, Mckenzie C a, Brodsky E, Brittain JH, Reeder SB. Multi-Echo Water-Fat Separation and Simultaneous R2* Estimation with Multi-Frequency Fat Spectrum Modeling Huanzhou. Magnetic Resonance in Medicine. 2008;60(5):1122–1134.

97. Hernando D, Kellman P, Haldar JP, Liang ZP. Robust water/fat separation in the presence of large field inhomogeneities using a graph cut algorithm. Magnetic Resonance in Medicine. 2010;63(1):79–90.

98. Reeder SB, Robson PM, Yu H, Shimakawa A, Hines CDG, McKenzie CA, Brittain JH. Quantification of hepatic steatosis with MRI: The effects of accurate fat spectral modeling. Journal of Magnetic Resonance Imaging. 2009;29(6):1332–1339.

99. Nickel MD, Zhong X, Kannengiesser SAR. Water-fat seperation using low-resolution phase maps and eddie currrent compensation. In: ESMRMB 2013, 30th Annual Scientific Meeting, Toulouse, France, 3-5 October. Vol. 26. 2013. p. 454–455.

100. Rossato M, Cecchin D, Vettor R. Brown adipose tissue localization using 18F-FDG PET/MRI in adult. Endocrine. 2016:1–2.

101. Bernard CP, Liney GP, Manton DJ, Turnbull LW, Langton CM. Comparison of fat quantification methods: A phantom study at 3.0T. Journal of Magnetic Resonance Imaging. 2008;27(1):192–197.

102. Ren J, Dimitrov I, Sherry DA, Malloy CR. Composition of Adipose Tissue and Marrow Fat by 1H MR Spectroscopy at 7 Tesla. Journal of lipid research. 2008;49:2055–2062.

103. Lee P, Zhao JT, Swarbrick MM, Gracie G, Bova R, Greenfield JR, Freund J, Ho KKY. High prevalence of brown adipose tissue in adult humans. The Journal of clinical endocrinology and metabolism. 2011;96(8):2450–2455.

104. Zingaretti MC, Crosta F, Vitali A, Guerrieri M, Frontini A, Cannon B, Nedergaard J, Cinti S. The presence of UCP1 demonstrates that metabolically active adipose tissue in the neck of adult humans truly represents brown adipose tissue. The FASEB Journal . 2009;23(9):3113–

3120.

105. Branca RT, He T, Zhang L, Floyd CS, Freeman M, White C, Burant A. Detection of brown adipose tissue and thermogenic activity in mice by hyperpolarized xenon MRI. Proceedings of the National Academy of Sciences. 2014;111(50):18001–18006.

106. Franz D, Karampinos DC, Rummeny EJ, Souvatzoglou M, Beer AJ, Nekolla SG, Schwaiger M, Eiber M. Discrimination Between Brown and White Adipose Tissue Using a 2-Point Dixon Water-Fat Separation Method in Simultaneous PET/MRI. Journal of Nuclear Medicine. 2015;56(11):1742–1747.

107. Frontini A, Cinti S. Distribution and Development of Brown Adipocytes in the Murine and Human Adipose Organ. Cell Metabolism. 2016;11(4):253–256.

108. Lau a Z, Chen a P, Gu Y, Ladouceur-Wodzak M, Nayak KS, Cunningham CH. Noninvasive identification and assessment of functional brown adipose tissue in rodents using hyperpolarized (13)C imaging. International Journal of Obesity. 2014;38(1):126–31.

109. Hernando D, Sharma SD, Kramer H, Reeder SB. On the confounding effect of temperature on chemical shift-encoded fat quantification. Magnetic Resonance in Medicine. 2014;72(2):464–470.

110. McCallister D, Zhang L, Burant A, Katz L, Branca RT. Effect of Microscopic Susceptibility Gradients on Chemical-Shift-Based Fat Fraction Quantification in Supraclavicular Fat. Journal of Magnetic Resonance Imaging. 2018.

111. Ma X, Holalkere N-S, R AK, Mino-Kenudson M, Hahn PF, Sahani D V. Imaging-based Quantification of Hepatic Fat: Methods and Clinical Applications1. RadioGraphics. 2009;29(5):1253–1277.

112. Kühn JP, Hernando D, Mensel B, Krüger PC, Ittermann T, Mayerle J, Hosten N, Reeder SB. Quantitative chemical shift-encoded MRI is an accurate method to quantify hepatic steatosis. Journal of Magnetic Resonance Imaging. 2014;39(6):1494–1501.

113. Hindman JC. Proton Resonance Shift of Water in the Gas and Liquid States. The Journal of Chemical Physics. 1966;44(12):4582.

114. Poorter J De, Wagter C De, Deene Y De, Thomsen C, Stalhlberg F, Achten E. Noninvasive MRI Thermometry with the Proton Resonance Frequency (PRF) Method: In Vivo Results in Human Muscle. Magnetic Resonance in Medicine. 1995;33(1):74–81.

115. Hopkins JA, Wehrli FW. Magnetic susceptibility measurement of insoluble solids by NMR: Magnetic susceptibility of bone. Magnetic Resonance in Medicine. 1997;37(4):494–500.

116. Durrant CJ, Hertzberg MP, Kuchel PW. Magnetic susceptibility: Further insights into macroscopic and microscopic fields and the sphere of Lorentz. Concepts in Magnetic Resonance Part A: Bridging Education and Research. 2003;18(1):72–95.

117. McCallister A, Zhang L, Burant A, Katz L, Branca RT. A pilot study on the correlation between fat fraction values and glucose uptake values in supraclavicular fat by simultaneous PET/MRI. Magnetic Resonance in Medicine. 2017;78(5).

118. Chu SCK, Xu Y, Balschi JA, Springer CS. Bulk magnetic-susceptibility shifts in NMR-studies of compartmentalized samples - use of paramagnetic reagents. Magnetic Resonance in Medicine. 1990;13(2):239–262.